

Utah State University

DigitalCommons@USU

All Graduate Theses and Dissertations

Graduate Studies

5-2011

Aerodynamic Thrust Vectoring For Attitude Control Of A Vertically Thrusting Jet Engine

M. Ryan Schaefermeyer
Utah State University

Follow this and additional works at: <https://digitalcommons.usu.edu/etd>



Part of the [Mechanical Engineering Commons](#)

Recommended Citation

Schaefermeyer, M. Ryan, "Aerodynamic Thrust Vectoring For Attitude Control Of A Vertically Thrusting Jet Engine" (2011). *All Graduate Theses and Dissertations*. 1237.

<https://digitalcommons.usu.edu/etd/1237>

This Thesis is brought to you for free and open access by the Graduate Studies at DigitalCommons@USU. It has been accepted for inclusion in All Graduate Theses and Dissertations by an authorized administrator of DigitalCommons@USU. For more information, please contact digitalcommons@usu.edu.



AERODYNAMIC THRUST VECTORING FOR ATTITUDE CONTROL
OF A VERTICALLY THRUSTING JET ENGINE

by

M. Ryan Schaefermeyer

A thesis submitted in partial fulfillment
of the requirements for the degree

of

MASTER OF SCIENCE

in

Mechanical Engineering

Approved:

Dr. Stephen A. Whitmore
Major Professor

Dr. David Geller
Committee Member

Dr. Barton Smith
Committee Member

Dr. Mark R. McLellan
Vice President for Research and
Dean of the School of Graduate Studies

UTAH STATE UNIVERSITY
Logan, Utah

2011

Copyright © M. Ryan Schaefermeyer 2011

All Rights Reserved

Abstract

Aerodynamic Thrust Vectoring for Attitude Control
of a Vertically Thrusting Jet Engine

by

M. Ryan Schaefermeyer, Master of Science

Utah State University, 2011

Major Professor: Dr. Stephen A. Whitmore
Department: Mechanical and Aerospace Engineering

NASA's long range vision for space exploration includes human and robotic missions to extraterrestrial bodies including the moon, asteroids and the martian surface. All feasible extraterrestrial landing sites in the solar system are smaller and have gravitational fields of lesser strength than Earth's gravity field. Thus, a need exists for evaluating autonomous and human-piloted landing techniques in these reduced-gravity situations. A small-scale, free-flying, reduced-gravity simulation vehicle was designed by a group of senior mechanical engineering students with the help of faculty and graduate student advisors at Utah State University during the 2009-2010 academic year. The design reproduces many of the capabilities of NASA's 1960s era lunar landing research vehicle using small, inexpensive modern digital avionics instead of the large, expensive analog technology available at that time. The final vehicle design consists of an outer maneuvering platform and an inner gravity offset platform. The two platforms are connected through a set of concentric gimbals which allow them to move in tandem through lateral, vertical, and yawing motions, while remaining independent of each other in rolling and pitching motions. A small radio-controlled jet engine was used on the inner platform to offset a fraction of Earth's gravity ($5/6^{th}$ for lunar simulations), allowing the outer platform to act as though it is flying in a reduced-gravity

environment. Imperative to the stability of the vehicle and fidelity of the simulation, the jet engine must remain in a vertical orientation to not contribute to lateral motions. To this end, a thrust vectoring mechanism was designed and built that, together with a suite of sensors and a closed loop control algorithm, enables precise orientation control of the jet engine. Detailed designs for the thrust vectoring mechanisms and control avionics are presented. The thrust vectoring mechanism uses thin airfoils, mounted directly behind the nozzle, to deflect the engine's exhaust plume. Both pitch and yaw control can be generated. The thrust vectoring airfoil sections were sized using the two-dimensional airfoil section compressible-flow CFD code, XFOIL, developed at the Massachusetts Institute of Technology. Because of the high exhaust temperatures of the nozzle plume, viscous calculations derived from XFOIL were considered to be inaccurate. XFOIL was run in inviscid flow mode and viscosity adjustments were calculated using a Utah State University-developed compressible skin friction code. A series of ground tests were conducted to demonstrate the thrust vectoring system's ability to control the orientation of the jet engine. Detailed test results are presented.

(127 pages)

Public Abstract

Aerodynamic Thrust Vectoring for Attitude Control
of a Vertically Thrusting Jet Engine

by
M. Ryan Schaefermeyer

NASA's Exploration Systems Mission Directorate partnered with Utah State University to build a proof-of-concept reduced-gravity simulation vehicle. Funded through the Space Grant Senior Design program, the vehicle was built as a small-scale, free-flying prototype to demonstrate technologies that could one day be used to train human or robotic pilots for landing on extraterrestrial bodies such as the Moon, Mars or nearby asteroids. These nearby extraterrestrial bodies have less gravity than the Earth which changes the way flying vehicles are maneuvered. The vehicle uses modern hardware and digital electronic systems to reproduce many of the capabilities of NASA's retired lunar landing research vehicle that was used during the Apollo program of the 1960s. The vehicle design is split into two main platforms: an outer maneuvering platform and an inner gravity offset platform. The two platforms are connected through a set of concentric rings which allow them to move together through horizontal, vertical, and yawing motions, while remaining independent of each other in rolling and pitching motions. The two platforms are independently powered and controlled. The outer platform uses small airplane propellers in a configuration commonly referred to as a quadrotor. These rotors allow a pilot to fly the vehicle over a simulated flight plan using a handheld radio controller. A small jet engine was used on the inner platform to offset a fraction of Earth's gravity ($5/6^{th}$ for lunar simulations), allowing the outer platform to act as though it is flying in a reduced-gravity environment. A thrust vectoring control system was designed and built to stabilize the inner platform and to allow for precise orientation control of the jet engine. The thrust vectoring mechanism uses thin airfoils, mounted directly behind the jet engine's nozzle, to

deflect the engine's exhaust plume. The airfoils were designed using general code developed at the Massachusetts Institute of Technology as well as code developed specifically for this project at Utah State University. Detailed designs for the thrust vectoring mechanisms and control avionics are presented. A series of ground tests were conducted to demonstrate the thrust vectoring system's ability to control the orientation of the jet engine. Detailed test results are presented.

To my wife and children. Thank you for your continued love and support.

Acknowledgments

I would first like to thank my advisor and mentor, Dr. Stephen Whitmore. There are not many professors who would spend so much extra time outside the classroom working side-by-side with their students. His patience with this project, which has extended many months past its original finish date, has been never-ending. He has taught me many skills both in and out of the classroom that will be an asset to me throughout my career.

Secondly, I would like to thank the 2009-2010 Senior Design “Rocket” Team. This vehicle and its thrust vectoring applications would never have been realized in physical form if not for all of their individual contributions. Special thanks go to Jess Godfrey and Jon McCulley for their continued volunteer support of this project after the completion of their undergraduate work. Moving and operating the vehicle with all of its support equipment would have been a much more difficult task if not for their help. Additional recognition is due to Shannon Eilers for sharing his expertise regarding Simulink modeling.

I would also like to thank NASA’s Exploration Systems Mission Directorate Space Grant Senior Design program for funding this project. If not for this program and the individuals at NASA having the insight to reach out to and support future engineers, this project could never have been realized.

Most importantly, I would like to thank my loving wife, Barbara, for her constant support. She never gave up on me even when it looked like this project would never work. She sacrificed many days and nights alone, seeing me only long enough to bring me food to sustain me for another few hours. Her tireless efforts in raising our children and maintaining our day-to-day lives have made all the difference.

M. Ryan Schaefermeyer

Contents

	Page
Abstract	iii
Public Abstract	v
Acknowledgments	viii
List of Tables	xi
List of Figures	xii
Nomenclature	xv
1 Introduction	1
1.1 Research Motivation	1
1.2 Project Overview	6
1.3 Research Objectives	10
2 Thrust Vectoring Literature Review	14
2.1 Mechanical Nozzle Manipulation	15
2.2 Secondary Fluidic Injection	20
2.3 Exhaust Flow Deflection	23
3 Final Vehicle Design	27
3.1 Vehicle Overview	27
3.2 Outer Platform: Vehicle Maneuvering System	29
3.3 Inner Platform: Gravity Offset	32
4 Static Engine Testing and Characterization	34
4.1 Test Platform	34
4.2 Static Thrust Test Results	44
4.3 Nozzle Exit Plane Measurements	48
4.4 Nozzle Computational Fluid Dynamics Study	52
5 Aerodynamic Thrust Vectoring System	57
5.1 Analysis of Alternative TVC Methods	57
5.2 Top Level View	58
5.3 Airfoil Design	59
5.4 Inner Platform Avionics	73
5.5 Thrust Vectoring Control System	76

6	Test Results	81
6.1	Outer Platform 1-G Free Flight Tests	81
6.2	Static Thrust Vectoring Tests	83
6.3	Moment of Inertia Measurements	87
6.4	Free Gimbal Combined Systems Tests	92
7	Thrust Vectoring System Design Evolution	96
8	Conclusions	100
	REFERENCES	104

List of Tables

Table	Page
2.1 Thrust Vectoring Publications Investigated in the Literature Review with Associated Conclusions	16
4.1 Manufacturer Specifications for Thrust Stand Instrumentation	37
4.2 Typical Jet Engine Test Stand Calibration Matrix: Individual Load Cell mV Readings	42
4.3 Typical Jet Engine Test Stand Calibration Matrix: Normalized Sensitivity .	42
4.4 Statistical Evaluation of Four Identical Load Calibration Cases	43
4.5 Test Stand Mean Measurement Error Uncertainty Estimates	44
4.6 Sensitivity of Thrust Calculations to γ	51
4.7 Flow Properties Used in the CFD Analysis	52
5.1 Sutherland's Parameters for Viscosity Calculation	63
5.2 Aerodynamic Properties for a NACA 0012 Airfoil at $M = 0.5$ and Various Angles of Attack	67
5.3 Airfoil Length Required for a 5.08 mm (0.2 in.) Quarter Chord Thickness .	70
6.1 Best-fit Linear Pendulum Model Parameters for the Inner Platform	90
6.2 Inner Platform Mass, Vertical Center of Gravity and Moment of Inertia Estimates	90
8.1 Roadmap for Future Research	102

List of Figures

Figure	Page
1.1 Locations of the six manned Apollo Moon landing sites.	2
1.2 Required pitch angles for equivalent horizontal accelerations in 1-g and $1/6^{th}$ -g environments.	5
1.3 The Lunar Landing Research Vehicle (LLRV).	6
1.4 Comparison of the ESLRV and LLRV.	8
1.5 Close up view of the ESLRV gimbal design.	9
1.6 Vehicle design process.	10
1.7 Phases of the Apollo landing profile.	11
1.8 Design Reference Mission.	12
2.1 Demonstration of TVC schemes utilizing mechanical nozzle manipulation. .	17
2.2 Depiction of graphite thrust vectoring vanes that were used on German V-2 rockets.	24
2.3 Examples of thrust vectoring that used the exhaust flow deflection technique.	25
3.1 Vehicle functional diagram.	28
3.2 Final design configuration.	28
3.3 Quadrotor propeller layout.	30
3.4 QuadPowered [®] control system functional diagram.	31
3.5 Outer platform wiring diagram.	32
3.6 The JF-170 Rhino: a single-stage, axial flow, centrifugal RC turbine engine.	33
4.1 Jet engine test stand showing various components.	35
4.2 Traversing pitot probe drive mechanism.	38
4.3 Calibration forces and moments being applied to the thrust stand.	41

4.4	JF-170 Rhino thrust vs. RPM curve.	45
4.5	Measured fuel massflow as a function of throttle setting.	46
4.6	Nozzle exit plane mach number distribution for various throttle settings. . .	47
4.7	JF-170 Rhino nozzle and turbine exit fairing.	47
4.8	Total pressure profile for the JF-170 nozzle exit plane at 75% throttle. . . .	49
4.9	Calculated local Mach number for the JF-170 nozzle exit plane at 75% throttle.	49
4.10	Calculated local velocity for the JF-170 nozzle exit plane at 75% throttle. .	50
4.11	Course CFD grid with boundary conditions used in this project.	52
4.12	Dynamic pressure distribution calculated on the fine grid using both the First Order Upwind and Quick methods.	54
4.13	Mach number distribution calculated on the fine grid using both the First Order Upwind and Quick methods.	54
4.14	Dynamic pressure contours in and downstream of the jet engine nozzle as calculated on the fine grid using the QUICK method.	55
4.15	Mach number contours in and just outside the jet engine nozzle as calculated on the fine grid using the QUICK method.	56
5.1	Mechanical configuration of the TVC components.	58
5.2	Profile of pressure drag caused by boundary layer separation.	60
5.3	Custom airfoil design and the associated pressure distribution calculated by XFOIL.	64
5.4	Tapered wedge airfoil design and the associated pressure distribution calcu- lated by XFOIL.	65
5.5	Local pressure coefficient vs. chord length for a NACA 0012 airfoil at $M = 0.5$ and $\alpha = 2.0^\circ$ as calculated in XFOIL.	66
5.6	Total drag force created by a NACA 0012 airfoil pair.	68
5.7	Lift to Drag ratio for a NACA 0012 airfoil pair.	68
5.8	NACA 0012 turning vane pair with annotated dimensions.	70
5.9	Pitching moment about the engine's gimbal point generated by the NACA 0012 vane pair.	71

5.10	Pitching moment about the engine's gimbal point adjusted for low aspect ratio effects.	73
5.11	Gumstix [®] Overo [™] Fire flight computer.	74
5.12	The 3DM-GX3 [®] -25 IMU used to sense angular orientation and rates.	75
5.13	Inner platform avionics power and signal routing.	76
5.14	A block diagram of the end-to-end control law for a single axis on the ESLRV.	77
5.15	A block diagram for a standard PID controller.	78
5.16	Vane deflection for pitch angle trim.	79
6.1	Tethered flights of the outer platform maneuvering system using the VALASARA-PTOR open-loop control method.	82
6.2	Free flight tests of the outer platform maneuvering system using the Quad-Powered board controller.	83
6.3	Load cell mV output for a typical thrust vectoring test case.	84
6.4	Comparison of original and adjusted load cell readings.	85
6.5	Calculated thrust vectoring forces and moments using adjusted load cell data.	86
6.6	Airfoil angle of attack required, as a function of throttle setting (or Mach number), to achieve a desired moment for the vehicle's pitch axis.	87
6.7	JF-170 Rhino thrust vs. RPM curve with the vectoring system installed.	88
6.8	Unforced response of inner platform compared to pendulum model.	89
6.9	Inner platform unforced response spectrum magnitude.	91
6.10	Test setup for TVC ground tests.	92
6.11	Commanded orientation vs. IMU sensed orientation for both pitch and roll axes.	95
7.1	Sound levels produced at third octave frequencies by the JF-170 jet engine.	98
7.2	Design progression of the inner gimbal avionics.	99

Nomenclature

$[]^T$	matrix transpose
α	airfoil angle of attack, <i>deg</i>
$\ddot{\theta}$	pitch axis angular acceleration, <i>rad/sec²</i>
δt	sample interval, <i>sec</i>
$\frac{\partial F_j}{\partial V_{\{I\}i}}$	variation in the force measured along the “j” axis with respect to sensed voltage from load cell “Ii”, <i>N-m/volt</i>
$\frac{\partial M_j}{\partial V_{\{I\}i}}$	variation in the moment measured about the “j” axis with respect to sensed voltage from load cell “Ii”, <i>N-m/volt</i>
$\dot{\theta}$	pitch axis angular velocity, <i>rad/sec</i>
\dot{m}	mass flow rate, <i>kg/sec</i>
\dot{m}_{exit}	mass flow rate across nozzle exit plane, <i>kg/sec</i>
γ	ratio of specific heats
\hat{J}	least squares estimate of thrust stand calibration matrix, <i>N/volt or N-m/volt</i>
μ_∞	freestream dynamic viscosity, <i>N-sec/m²</i>
μ	dynamic viscosity, <i>N-sec/m²</i>
ν	distribution mean, <i>N or N-m</i>
ω_n	natural frequency of either the unforced inner platform oscillation or the control filter, <i>rad/sec</i>
\bar{V}	average velocity, <i>m/sec</i>
\bar{V}_{exit}	average velocity across nozzle exit plane, <i>m/sec</i>
\bar{V}_{inlet}	average velocity into jet engine, <i>m/sec</i>
\bar{x}	sample mean, <i>N or N-m</i>
ϕ	roll angle, <i>deg</i>
ρ_∞	freestream density, <i>kg/m³</i>

ρ	density, kg/m^3
σ_x	sample standard deviation, N or $N-m$
θ_{IMU}	pitch angle measured by the IMU, deg
θ_{ref}	reference pitch angle, deg
θ	pitch angle, deg
$\tilde{\theta}$	commanded pitch angle error, deg
\tilde{C}_{DT}	total drag section coefficient
\tilde{C}_L	section lift coefficient
\tilde{C}_{MG}	gimbal point moment section coefficient
\tilde{F}	calibration matrix of force and moment inputs, N or $N-m$
\tilde{V}	calibration matrix of load cell outputs, $volts$
ζ	damping ratio of either the unforced inner platform oscillation or the control filter
$\{I\}$	load cell index: A, B or C
a	control filter coefficient
A_{exit}	nozzle exit plane area, m^2
B	rate damping coefficient, $N-m/sec$
b	control filter coefficient
c	control filter coefficient
C_{Dfc}	friction drag coefficient for compressible flow
C_{Dfi}	friction drag coefficient for incompressible flow
C_{Di}	induced drag coefficient
C_L	lift coefficient
C_S	Sutherland's constant, K
d	control filter coefficient
D_T	total drag generated by the airfoils, N
e_s	Oswald span efficiency factor
f_n	natural frequency of the unforced inner platform oscillation, Hz
F_x	force directed along the x-axis of the static thrust stand, N

F_y	force directed along the y-axis of the static thrust stand, N
F_z	force directed along the z-axis of the static thrust stand, N
g	acceleration due to gravity, m/s^2
I_{yy}	principle moment of inertia about pitch axis, $kg-m^2$
J	thrust stand Jacobian matrix, $N/volt$ or $N-m/volt$
K	torsional spring coefficient, $N-m$
k	time index
K_D	derivative gain
K_I	integral gain
K_P	proportional gain
L	characteristic length (airfoil chord), m
L	lift generated by airfoils, N
M	Mach number
M_x	moment about the x-axis of the static thrust stand, $N-m$
M_y	moment about the y-axis of the static thrust stand, $N-m$
M_z	moment about the z-axis of the static thrust stand, $N-m$
M_∞	freestream Mach number
$M_{c/4}$	airfoil generated moment about the airfoil quarter chord, $N-m$
M_G	airfoil generated moment about the gimbal point, $N-m$
m_{inner}	mass attached to the inner platform, kg
N	number of thrust stand calibration data sets
n	number of points in the sample data set
p	roll rate, deg/sec
p_o	total pressure, Pa
p_{amb}	ambient pressure, Pa
p_{exit}	average pressure across nozzle exit plane, Pa
p_{static}	static pressure, Pa
q	pitch rate, deg/sec

R	nozzle radius at the exit plane, m
r	position along radial line of the nozzle, m
R_A	airfoil aspect ratio
R_g	gas constant, $J/kg\cdot K$
R_f	adiabaticity correction factor
Re	Reynolds number
$S_{\bar{x}}$	mean error confidence interval
T	thrust, N
t	time, sec
t_γ	student t variable corresponding to an arbitrary double-ended probability level
T_o	stagnation temperature, K
t_{95}	student t variable corresponding to a 0.95 double-ended probability level
T_∞	freestream temperature, K
T_{avg}	average boundary layer temperature, K
T_{ref}	reference temperature used in calculating the friction drag for compressible flow, K
T_{wall}	temperature at the wall, K
V	velocity, m/sec
$V_{\{I\}l_{adj}}$	adjusted lateral load cell voltage reading, <i>volts</i>
V_{Aa}	voltage reading from axial load cell A, <i>volts</i>
V_{Al}	voltage reading from lateral load cell A, <i>volts</i>
V_a	axial component of engine exhaust gas velocity, m/sec
V_{Ba}	voltage reading from axial load cell B, <i>volts</i>
V_{Bl}	voltage reading from lateral load cell B, <i>volts</i>
V_{Ca}	voltage reading from axial load cell C, <i>volts</i>
V_{Cl}	voltage reading from lateral load cell C, <i>volts</i>
V_r	radial component of engine exhaust gas velocity, m/sec
V_t	tangential component of engine exhaust gas velocity, m/sec
W	standard 1-g Earth weight, N
Z_{cg}	vertical offset of inner platform center of gravity from the gimbal pivot point, m

Chapter 1

Introduction

This paper presents research on a method for attitude control of a vertically thrusting jet engine. Motivation for this research as well as historical information on similar efforts is presented in this first chapter in an effort to give the reader sufficient insight into this research topic. The project's basic research objectives, goals and concept of operations (CONOPS) are set forth.

1.1 Research Motivation

Human and robotic missions beyond low earth orbit are key components of NASA's emerging strategy for space exploration [1]. Future missions will inevitably include human-crewed lunar and planetary surface landings. Trips to near-earth asteroids are also in the incipient planning stages. A permanent presence on the surface of an extraterrestrial body like Mars or the Moon will require many landings by both human-crewed and robotic spacecraft. Planetary and lunar surface landings are inherently dangerous, and successful landings are indeed rare.

Since the completion of the Apollo missions in the early 1970s only two successful soft landings have been achieved on the lunar surface, with the last landing being Luna 24 in 1976 [2]. During that same period, there were only six successful martian surface landings with nearly as many failures [3]. Although scientifically interesting surface geology was a secondary consideration in selecting landing sites for the aforementioned missions, the primary considerations were crew safety for the manned missions, vehicle safety, and mission success.

Evidence of NASA's conservative approach to extraterrestrial landings is observed by examining the locations of the Apollo mission landing sites. Figure 1.1 shows these sites, all

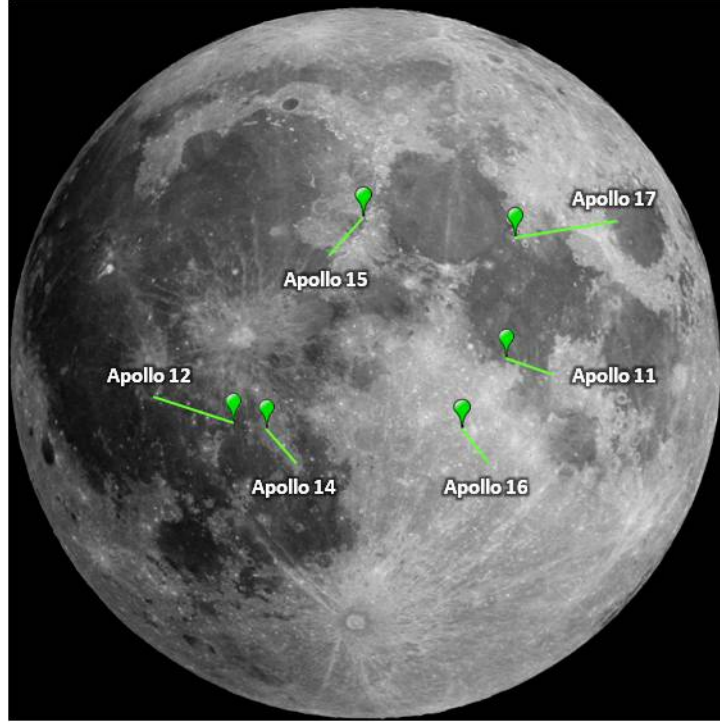


Fig. 1.1: Locations of the six manned Apollo Moon landing sites.

of which were in lunar plains. These landing sites were specifically chosen based upon their lack of craters, boulders, large hills and high cliffs and for their level landing surfaces [4]. The Lunar Excursion Module (LEM) could tolerate a maximum resting tilt of 12° . If the resting tilt was beyond that angle, the LEM ascent stage would not have been able to reach the proper return orbit to rendezvous with the orbiting command module [5]. All Martian surface landing sites have been selected for similar benign surface terrain characteristics.

With a long-term human extraterrestrial surface presence, scientific objectives will become more important, and the landing site terrain will become more diverse. As these surface landing sites become more scientifically interesting, they will correspondingly become more hazardous. Thus, the development of research and testing platforms allowing “pinpoint” autonomous landing systems to be evaluated, refined, and matured is essential.

A Mars hopper, proposed by Howe et al. at the Idaho National Laboratory is one such proposed vehicle that will require new, yet undeveloped, landing technologies. The Mars hopper will use carbon dioxide extracted from the martian atmosphere to hop from site

to site via a ballistic trajectory. Howe envisions that the platform, powered by radioactive isotopes, could jump to a new site every two to three days. It could do so until either the isotope fuel runs out or until some component on the vehicle fails [6]. Potentially, this mission profile will require dozens of landings in very rocky terrain. Such a vehicle will require a very robust landing and guidance system that will need to be thoroughly tested.

This Mars hopper will also require advanced technology which will allow it to identify safe landing sites. NASA's Jet Propulsion Laboratory (JPL) is working on such technology with their Autonomous Landing and Hazard Avoidance Technology (ALHAT) project. A research paper presented by Johnson et al. details the complicated analysis required by an onboard computer for a light detection and ranging (LIDAR) sensor-based ALHAT system. The LIDAR system is capable of directly measuring surface elevation from high altitude. Hazards such as steep slopes and large rocks can be detected from these measurements.

Using a Monte Carlo simulation, the JPL team analyzed several variations in several factors including vehicle hazard tolerance, landing diameter, analysis area hazard density to determine the probability of identifying a safe landing area. Successful identification of a landing area seems to be most sensitive to the vehicles landing tolerance as even a small increase greatly increases the probability of success. The JPL team also identifies the size of the target area as an important factor as larger areas require greater time to sense and process, in turn reducing the pilot's available reaction time. Though the technology is still in development it holds much promise for providing robotic explorers with autonomous landing capabilities [7].

The Mars hopper and ALHAT technologies will provide future missions with greater flexibility, though these systems will require testing in a more realistic mission environment before they can be fielded. Only on a free flying-platform can these surface landing technologies be developed to a sufficient technology readiness level (TRL) to be considered for ultra-expensive, extraterrestrial missions. Chiold Epp, of NASA's Johnson Space Center (JSC), summed up the need for research in extraterrestrial landings. In an article on the ALHAT program entitled "Four of Six Apollos," he is quoted saying:

“To paraphrase an old bromide, those who forget the past are doomed to land like it. Having looked at the Apollo landings I have come to two conclusions. One – those crews did a great job. Two – data from several of the landings support the idea that we must give future moon landers more information to increase the probability of mission success.”¹

1.1.1 Historical Background and Perspective

Powered landings on the lunar surface presented several difficult “situational awareness” challenges to the Apollo astronauts. One such challenge was the significant difference in visual cues from terrestrial landings which was very disorienting to the astronauts. Because of the lack of atmosphere, the surface lighting was very high in contrast, and astronauts had little or no ability to see into areas enveloped in shadow. To train astronauts to deal with this lighting effect, NASA’s Lunar Landing Training Facility (LLTF), which employed severe lighting and night training, was constructed [8]. The LLTF modeled the $1/6^{th}$ -g environment using a complex series of mechanical pulleys and cables. While providing a good visual simulation of the landing environment, the LLTF never successfully produced the required fidelity, and the piloting feel was described as “sluggish and artificial” [9].

More significantly, the LLTF was never able to satisfactorily reproduce the unusual physical orientation required of a lunar landing vehicle during the approach and landing phase of the mission. Because of the $1/6^{th}$ -g lunar environment (compared to a 1-g terrestrial environment), the lunar module required an extreme pitch angle for a given horizontal acceleration. Figure 1.2 demonstrates this reduced-g effect on pitch attitude. Here, the pitch angles required for equivalent horizontal accelerations are shown for an SH-2 helicopter, the LEM and the Apollo-era Lunar Landing Research Vehicle (LLRV). The pitch angles account for accelerating the weight of each vehicle as it operates in its respective environment [10]. Because a vehicle in $1/6^{th}$ -g requires only a fraction of the vertical thrust to hold altitude, the required pitch angle for a given amount of horizontal acceleration is significantly greater. That is, a pitch angle of 5° on earth is equivalent to 28° on the Moon.

¹Chiold Epp. Four of Six Apollos. National Aeronautical and Space Association; December 2008.

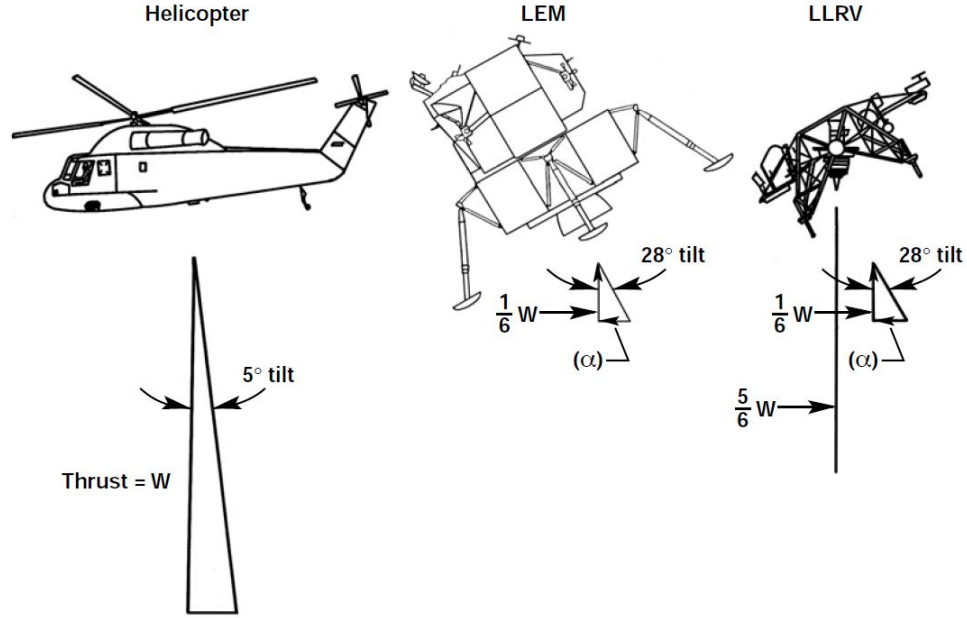


Fig. 1.2: Required pitch angles for equivalent horizontal accelerations in 1-g and $1/6^{th}$ -g environments.

A riskier, yet higher fidelity free-flying vehicle designed to simulate the $1/6^{th}$ -g lunar environment was developed at the NASA Flight Research Center (FRC) (later to become NASA's Dryden Flight Research Center). It was riskier because unlike the LLTF, there was no emergency tether to prevent the vehicle from crashing. This vehicle, the LLRV, used a single General Electric CF700-2V jet engine mounted vertically on a gimbal mechanism. The gimbal system was hydraulically driven to maintain the engine's orientation in the vertical direction. The engine's thrust was adjusted to offset $5/6^{th}$ of the vehicle's weight. This gravity offset provided by the jet engine enabled the vehicle to approximately respond in Earth's gravity field as it would on the Moon. Hydrogen peroxide thrusters were used to maneuver an outer platform where the pilot was seated. Collectively, these apparatus presented an accurate simulation of the lunar landing event to the pilots [10]. Figure 1.3 depicts the original LLRV platform on the tarmac at the FRC. The jet engine, pilot cabin and maneuvering thrusters are clearly visible.

The LLRV was originally built so that NASA scientists could evaluate the feasibility and accuracy of a lunar environment simulator. Once the LLRV proved to be an effec-

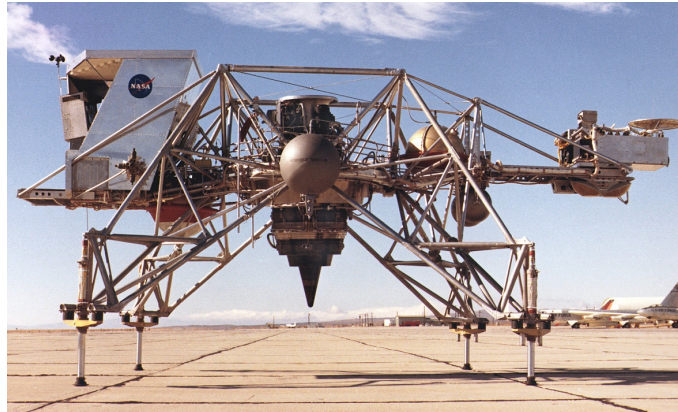


Fig. 1.3: The Lunar Landing Research Vehicle (LLRV).

tive simulator, it was adapted for crew training and five Lunar Landing Training Vehicles (LLTVs) were delivered to NASA's JSC. The LLTV provided a more accurate simulation over the LLRV by employing several modifications which allowed for a better representation of the final descent stage of a lunar landing [10].

The LLTV was a difficult vehicle to fly. The analog control systems available at the time were not sufficiently able to control the vehicle under all flight conditions. Controllability was especially poor when flying in cross winds. Three of the five original LLTV vehicles crashed before the end of the Apollo program. Emergency ejection and parachute systems prevented any significant injury to the pilots. There were also issues with hydrogen peroxide leaking from the thrusters' fuel tanks and burning the pilots' skin. Despite the sizable risks involved in flying the LLTV, seven of the nine astronauts who trained for lunar landings using the LLTV testified that the vehicle was a key component to the success of the Apollo missions [11]. In many ways, flying the LLTV, which presented 11 degrees of motion freedom to the pilot, was more difficult than achieving the lunar landing itself.

1.2 Project Overview

The project described in this document designed and built a free-flying vehicle that reproduces many of the capabilities demonstrated by the 1960s-era LLRV and LLTV, but using modern digital technology. The lessons learned from this project can be applied to a larger vehicle that would potentially be used to evaluate new technologies and train human

pilots.

The approach for this project, whenever possible, was to replace 1960s-era analog designs with proven and reliable, modern digital technologies. The subscale ($\sim 1/10^{th}$ scale relative to the LLRV) vehicle produced for this project simulates a reduced-gravity (i.e., lunar or planetary surface) environment using a vertically-thrusting jet engine to partially offset the vehicle weight. Although this vehicle is remotely piloted, the design is intended to scale up to a vehicle capable of carrying a human pilot. The vehicle is formally designated as the Extraterrestrial Surface Landing Research Vehicle (ESLRV).

The vehicle was the outcome of a two-semester senior design capstone course at Utah State University (USU). The design course was developed and instructed by Dr. Stephen Whitmore in the Mechanical and Aerospace Engineering Department at USU during academic year 2009-2010. Funding came largely from NASA's Exploration Systems Mission Directorate Space Grant Senior Design program with USU's College of Engineering providing additional support.

The complexity of the design – building an actual flying vehicle – required a large interdisciplinary team to be assembled. The size of the team – seven graduate research assistants, nineteen undergraduate students, and a faculty mentor – required the system requirements and individual responsibilities to be clearly defined. Formal systems engineering techniques were applied to facilitate progress towards project objectives.

Since much of the available reference material was written on the subject of lunar landings, and with the consideration that the next manned extraterrestrial landing will most likely occur on the Moon, the vehicle was designed primarily with a lunar landing in mind. As such, all references to extraterrestrial landings hereafter will be geared towards the lunar environment, but the reader should note that the vehicle is designed to be throttleable so that other extraterrestrial conditions can be simulated.

1.2.1 ESLRV Design and Concept of Operation

Figure 1.4 compares the CONOPS for the ESLRV to the original LLRV. The ESLRV is composed of two platforms: an inner platform to hold the gravity offset system, and

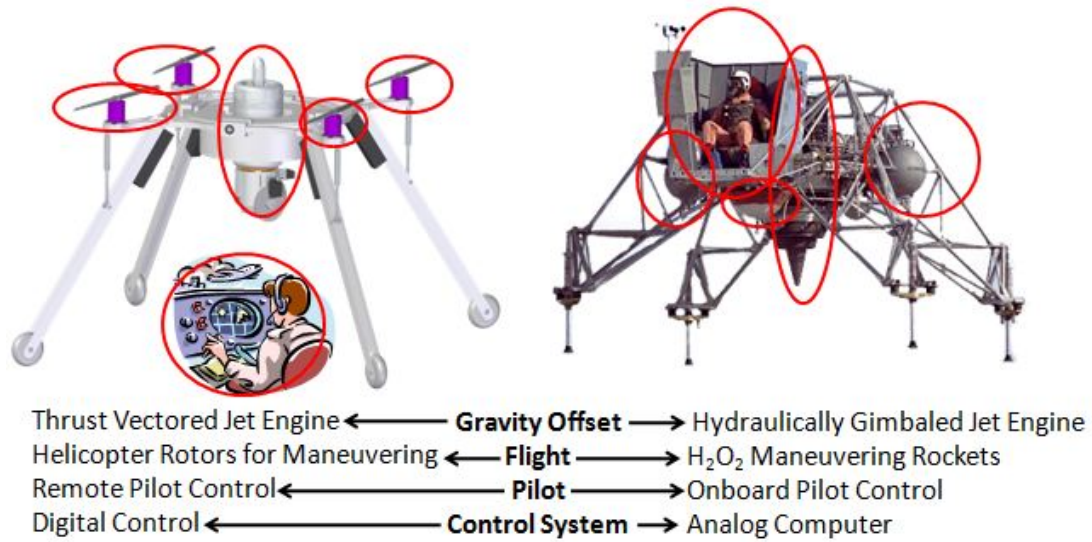


Fig. 1.4: Comparison of the ESLRV and LLRV.

an outer platform to support the maneuvering flight controls. The gravity offset system lifts $5/6^{th}$ of the total vehicle weight during hovering flight, while the maneuvering system controls the horizontal and vertical accelerations of the vehicle and lifts the remaining $1/6^{th}$ of the total weight.

The vehicle design features a two-axis gimbal system which allows the inner platform to move independently in two degrees of freedom from the outer maneuvering platform. Figure 1.5 depicts the platform gimbal design. The outer gimbal-ring holds all of the maneuvering rotors and associated drive-train components, while the inner gimbal-ring holds the gravity offset jet engine and associated equipment. The function of the gimbal platform is to uncouple the roll and pitch rotational dynamics between the two platforms. This design allows the inner platform to maintain a constant downward thrust while the outer platform is free to rotate and maneuver. The stability of each platform is maintained by separate and independent control systems.



Fig. 1.5: Close up view of the ESLRV gimbal design. The landing gear was removed for visual clarity.

The final propulsion systems selected for the inner and outer platforms were the result of trade-study assessments. The gravity offset system features a Jet-Central® JF-170 Rhino [12] centrifugal turbine jet engine. A jet engine was selected for this role primarily due to its high power to weight ratio.

Figure 1.6 shows the recursive process that was followed when during the vehicle's design phase. Each decision had ramifications on every aspect of the vehicle. Periodically throughout the design, each subsystem was reevaluated to ensure that it would still enable the project's goals to be met without negative consequences on the performance of the other subsystems.

1.2.2 Design Reference Mission

A well-defined Design Reference Mission (DRM) sets forth top-level program requirements but limits scope and restricts requirement growth. The DRM for this vehicle duplicates as many elements of a lunar landing mission as is feasible within the schedule and budget constraints of a single-year undergraduate student design project.

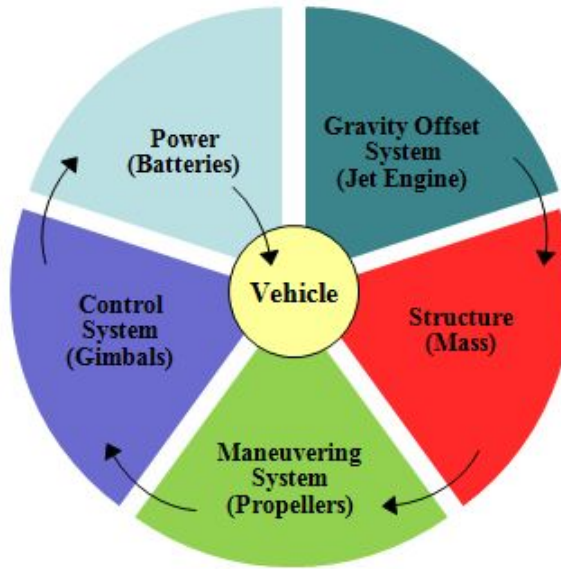


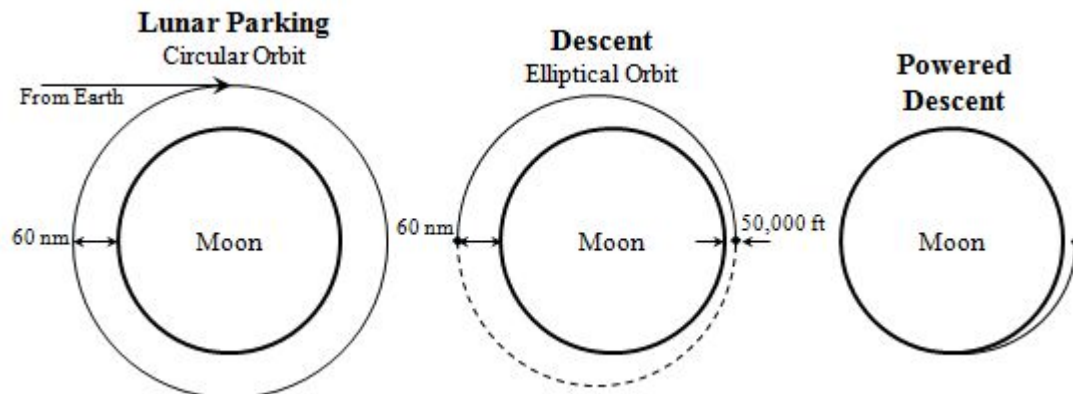
Fig. 1.6: Vehicle design process.

Figure 1.7 shows the three phases of the Apollo landing profile, which the DRM for the ESLRV attempted to reproduce [13]. Pictured are the in-orbit Keplerian maneuvers (1.7a), the powered descent phase (1.7b), and the final approach and landing phase (1.7c). Two key waypoints are shown on the approach trajectory: high gate – where the vehicle transitions from the powered descent to approach, and low gate – where the vehicle transitions from approach to the vertical descent.

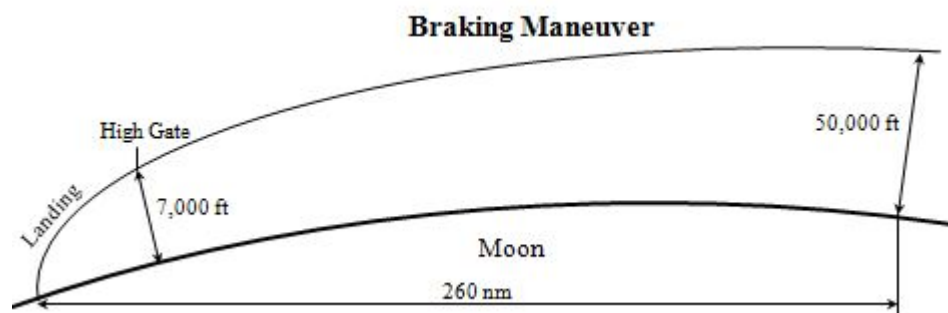
To achieve a simulated lunar landing approach, the ESLRV climbs to gain altitude, maneuvers horizontally to get onto the proper approach trajectory, then begins the powered descent before leveling off for a vertical landing. An initial systems check is performed when the vehicle is at a one meter hover. Figure 1.8 depicts the DRM of the ESLRV. Velocity and altitude markers were scaled from the actual NASA mission profile to keep the vehicle within the available testing range.

1.3 Research Objectives

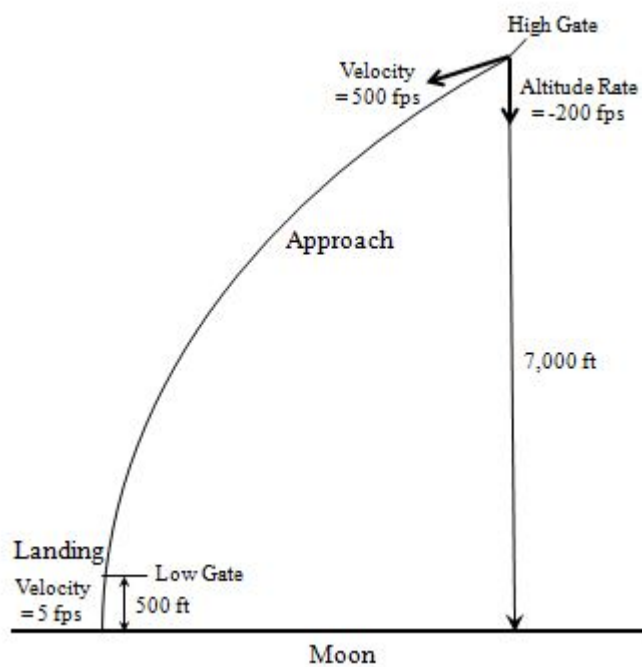
The success of this vehicle hinges on its ability to maintain a vertical orientation of the inner platform and jet engine. Any deviation from vertical will contribute to lateral motions and decrease the force that is holding the vehicle aloft. As can be surmised, coupled vertical



(a) Keplerian maneuvers.



(b) Powered descent.



(c) Approach and landing.

Fig. 1.7: Phases of the Apollo landing profile.

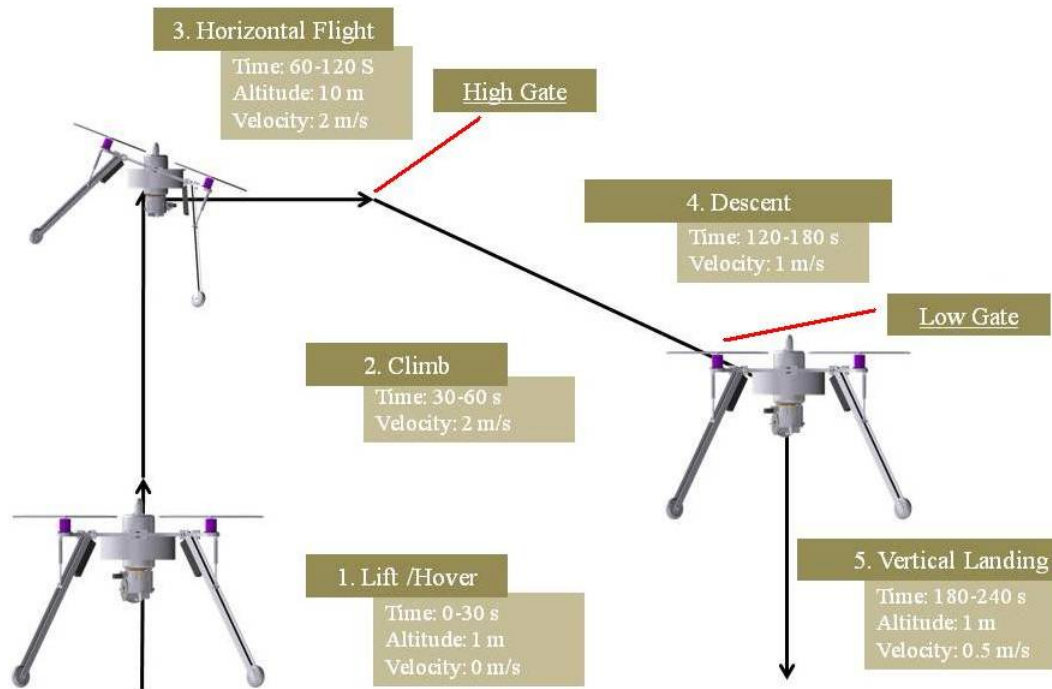


Fig. 1.8: Design Reference Mission.

and horizontal dynamics could adversely affect vehicle stability.

The LLRV maintained a consistent orientation of the central jet engine by using a hydraulic mechanism to physically rotate the inner platform and jet engine relative to the outer platform [10]. Mechanically driving the inner ring against the outer ring to position the jet engine results in two forces: the force exerted on the inner ring by the hydraulic system and a reactionary force exerted on the outer ring. The reactionary force will tend to rotate the outer platform in an undesired manner and must either be overcome by a large moment of inertia (compared to the inner ring's moment of inertia) or by the craft's maneuvering system. Additionally, the very existence of the reactionary force means that the inner ring and the outer ring are not fully uncoupled in pitch and roll. These interaction dynamics detract from the original, independent gravity offset concept.

Since, like the LLRV, the ESLRV uses a jet engine for the gravity offset system, orientation control by means of thrust vectoring presented itself as an attractive solution. Thrust vectoring uses the engine's own exhaust to create side forces capable of altering the engine's

vertical orientation. Selecting thrust vectoring as a means of orientation control allowed the inner and outer platforms to be designed as independent systems. This feature allows the two platforms to be completely uncoupled in pitch and roll rotational dynamics. A robust, closed-loop control system was designed and paired with the thrust vectoring system. This thesis presents the design features and development history for this thrust vectoring system. Ground test results will be presented to demonstrate the effectiveness of the system.

Chapter 2

Thrust Vectoring Literature Review

A literature review was conducted to understand the current state-of-the-art with regard to thrust vectoring systems for airbreathing engines. Many articles were found on thrust vectoring as it applies to fighter aircraft maneuverability augmentation. Only a single reference was found that discusses the application of thrust vectoring to the unique situation of orientation control and is presented in this section. Though limited in control applications, the available literature does shed insight on various thrust vectoring methods and their potential for application to different engine configurations and circumstances. Table 2.1 lists the various vectoring technologies reviewed along with the paper's primary author and their major conclusions regarding the technology.

Thrust vectoring involves redirecting some portion of thrust from the jet engine in any direction other than the normal axial direction. Thrust vectoring is used to control an aircraft's or rocket's motions in roll, pitch and yaw [14]. For fighter aircraft, the benefits of thrust vector control (TVC) include control augmentation and improved survivability. The use of TVC also allows for maneuverability and control at low airspeeds and very high angles of attack, both of which are otherwise inoperable flight regimes [15]. The X-31 and the US Air Force's F-22 are two examples of working aircraft that use TVC for enhanced maneuverability.

Several TVC methods are available for use on a jet engine. Some of these options include: rotation of the entire engine relative to the vehicle; rotation of the engine nozzle in order to direct the exhaust gases in a different direction; insertion of movable vanes or paddles into the exhaust flow; secondary fluidic injection; diversion of exhaust gases prior to the nozzle exit. These methods fall into three primary categories: nozzle manipulation, secondary fluidic injection and exhaust gas deflection. It should be noted that any TVC

method reduces the available axial thrust since it is redirecting a portion of the engine's total thrust away from the axial line.

Traditionally, jet engines use either a convergent or a convergent-divergent nozzle to speed up the exhaust gases and thus increase the thrust of the engine. The latter type uses the properties of an aerodynamic throat, or choking point, to increase the velocity of the exhaust gases to supersonic speeds. Thrust vectoring is traditionally used on fighter aircraft that utilize a convergent-divergent nozzle design. As such, most of the applications of TVC systems, as found in the literature, are geared towards the capabilities and flow properties associated with supersonic nozzles.

2.1 Mechanical Nozzle Manipulation

One commonly used thrust vectoring method involves manipulating the physical configuration of the exhaust nozzle on the jet engine or rocket motor. When the nozzle is physically turned to point in a different direction, the thrust is also pointed in this new direction. This method is commonly used on aircraft and is the most common method used with rocket-propelled launch vehicles.

Convergent-divergent nozzles are sophisticated pieces of hardware that are usually tuned to operate under specific pressure and flow conditions. Altering the nozzle's geometry, specifically the geometry of the aerodynamic throat, in an effort to vector the flow can have unintended consequences that negatively impact engine performance and thrust.

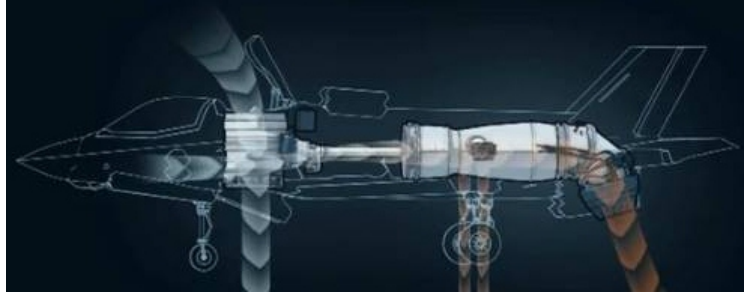
In 1990, Berrier and Taylor proposed that using a gimbal mechanism upstream of the nozzle to turn the flow would have little impact on the overall thrust [15]. By turning the flow in the low-speed, subsonic region ahead of the throat, flow-turning losses are minimized. Their experimental data supports this claim. At geometric vector angles up to 25° , and through a wide range of nozzle pressure ratios, the authors report a maximum thrust loss of only 2%. Additionally, they surmise that this loss is probably due to a calculation error on their part.

Examples of mechanical nozzle manipulation can be seen on two U.S. Air Force fighter jets, namely the F-35 and the F-22. Figure 2.1a illustrates how the F-35 uses a gimbal

Table 2.1: Thrust Vectoring Publications Investigated in the Literature Review with Associated Conclusions

Primary Author	Technology Investigated	Date Published	Major Conclusions
Berrier	Gimbaled nozzle	1990	Turning the flow in the subsonic regime before the nozzle choke point is a highly efficient vectoring technique.
Carson	Variable geometry nozzle	1991	Meant to turn the flow in the sonic regime, this method accidentally manipulated the aerodynamic choke point, turning the flow in the subsonic regime. Also a very efficient technique.
Wing	Adjustable internal nozzle contouring	1997	Adjustable contouring did not produce satisfactory degrees of vectoring. This method also greatly reduced the overall thrust level. Not a viable method.
Deere	Separation Control	2003	Not effective at changing the location of the choke point, but controlling the flow separation in the nozzle did achieve large vectoring angles.
Flamm	Dual Throat Fluidic Vectoring	2007	Most effective when the two minimum areas are equal. This method also achieves large vectoring angles by controlling the flow separation.
Dungan	V-2 Post-exit vanes	2011	One of the earliest known uses of thrust vectoring. These vanes were functional, yet limited in effectiveness because they had not been fully characterized.
Berrier	Post-exit thrust vectoring vanes	1988	Applicable across a wide range of nozzle configurations. Capable of very large vectoring angles, but at the cost of overall thrust.
Bowers	F-18 Thrust Vectoring	1996	Used post-exit vanes despite thrust loss issues. Effectively improved the F-18's maneuvering abilities.
Alcorn	X-31 Thrust Vectoring	1996	Also used post-exit vanes. Tests demonstrated the ability of this method to stabilize a tailless plane.

mechanism for thrust vectoring in order to provide short take-off and vertical landing capabilities. Figure 2.1b shows the F-119 engine, used on the F-22, and the extents to which its nozzle can rotate in the pitch direction.



(a) An illustration of the TVC techniques used on the F-35B. The rotation of the aft nozzle is clearly visible.



(b) F119 engine test: The two blue streams show the extent of its TVC capabilities.

Fig. 2.1: Demonstration of TVC schemes utilizing mechanical nozzle manipulation.

Both the F-22 and F-35 are examples of single-axis thrust vectoring systems. Additionally, researchers have investigated the effects of equipping various engine configurations with multi-axis thrust vectoring systems. Carson and Capone, in 1991, proposed the use of a circumferentially segmented divergent nozzle flap that would be capable of vectoring the thrust in any arbitrary direction [16]. To investigate the effects of this multi-axis system, they tested several subscale nozzles with fixed-geometry divergent sections that were representative of the full-scale, variable geometry. Of particular interest were the effects of flow turning in the divergent section where the flow is supersonic.

By measuring pressures along the divergent section, Carson and Capone discovered

that the actual aerodynamic throat moves as a result of the deflection of the divergent flaps and is relatively independent of the physical throat location. The actual throat location depends on nozzle pressure ratios and is highly inclined relative to the axial center-line. As a result of the inclined throat and its position changes, Carson and Capone discovered that the flow turning is essentially accomplished at subsonic speeds. This subsequently results in little or no turning losses. Their data supports this claim as they report thrust losses of only 1% under vectored nozzle conditions.

The nozzles tested by Carson and Capone were effective at vectoring the thrust when the nozzle pressure ratios were sufficient to reduce the flow separation on the side of the nozzle turned out of the flow. At sufficiently high pressure ratios, the nozzle achieved resultant thrust vectoring angles at least equal to and surprisingly, greater than the geometric angles. At a nozzle pressure ratio of 3.0 and with the nozzle in an afterburning configuration, Carson and Capone measured an effective thrust vector angle of 37° when the geometric angle was only 30° . The researchers also measured identical vectoring angles in both pitch and yaw. This result supported their notion that this system would be effective for multi-axis thrust vectoring.

Translation and inclination of the aerodynamic throat observed in [16] was an incidental result of the nozzle manipulation. Wing et al. proposed a nozzle that could mechanically control the translation and inclination of the throat by means of adjustable internal contouring [17]. In order to accomplish this, the nozzle required four independently adjustable sections that control the height of the throat. Changing the geometries of these sections changes the internal flow paths of the exhaust gases. As a result of using these sections, their nozzle took on a unique flat diamond or parallelogram shape. The nozzle was also equipped with drawers that allowed the upper and lower throat sections to move both upstream and downstream. Their hope was that by changing the angle of the throat relative to the nozzle center-line, flow turning would be accomplished in the subsonic region and thrust losses would be minimized.

Wing and his associates built and tested several subscale nozzles with fixed geometries representative of their adjustable design. The unique parallelogram nozzle exhibited inefficiencies even in an unvectored configuration. The divergent section expands only to a point, and then the upper and lower surfaces remain parallel until they terminate. For higher nozzle pressure ratios, this means that no additional thrust can be gained from the underexpanded flow. Also, even at peak thrust ratio, pressure readings indicate regions of flow separation, circulation, and sections of flow that are underexpanded. These combine to produce a maximum peak thrust ratio which is one to 2% below typical ratios produced by more traditional convergent-divergent nozzles.

Wing et al. tested several pitch and yaw vectoring configurations. Varying the internal flow-path contours by manipulating the four throat sections proved to be ill-suited to thrust vectoring in the pitch direction. In several cases, and especially at lower pressure ratios, they were unable to turn the flow to a measurable degree. Pressure readings indicated that the throat did not form on the internal ridges as was expected, and that it was still relatively perpendicular to the flow. In an attempt to force the flow to turn, they placed strips of material on the ridges to exaggerate the effect of the physical throat. These ridges were successful at forcing the throat to occur in the desired location, but also obstructed the flow and contributed significantly to thrust losses. The degree to which the thrust was vectored was limited because the nozzle exit flaps remained parallel with the original engine center-line and forced the flow to turn in the supersonic regime. This resulted in an oblique shock and associated thrust losses.

Using the drawers to alter the location of the throat achieved better results, but had a direct, negative effect on the power produced by the nozzle. At maximum displacement, this method achieved only 6° of thrust vectoring. Additionally, the magnitude of vectoring decreased with decreasing nozzle pressure ratios. This is undesirable considering that most maneuvering applications requiring thrust vectoring occur at low nozzle pressure ratios.

Yaw vectoring had many of the same thrust losses and flow issues observed in the pitch experiments, but with some notable differences. One big difference was that they

measured a higher maximum vectoring angle of nearly 11° . This maximum angle decreased with increasing nozzle pressure ratios and even reversed under some configurations at high pressure ratios. While 11° is significant, it is still not sufficient for maneuvering very large and heavy fighter planes. When one considers the complex flow interactions and associated thrust losses observed in both the pitch and yaw vectoring demonstrations, it becomes clear that adjustable internal contouring is not a viable thrust vectoring method.

2.2 Secondary Fluidic Injection

Thrust vectoring by means of secondary fluidic injection follows the same principle of nozzle manipulation, though it does not alter the physical configuration of the nozzle. Rather, by injecting a second fluid (typically bleed air from the engine compressor or fan), the exhaust flow can be manipulated and controlled. The injected fluid serves to create variable artificial nozzle boundaries. Nozzles utilizing fluidic vectoring techniques can have better stealth characteristics and weigh less because they can be constructed as fixed geometry nozzles and are not required to have complex adjustable hardware.

The three primary techniques of fluidic thrust vectoring that have been studied include counter flow, shock vector control and throat shifting. While the methods may vary, they can be compared to each other in terms of efficiency. Efficiency for these nozzles is given as the degree of vectoring achieved per percent of secondary flow required as compared to the primary nozzle flow. Thrust losses are also compared in the same manner as previously discussed with other thrust vectoring techniques. The shock vector control method works by creating shock barriers in the supersonic flow. These shock barriers are effective at turning the flow, but at the consequence of total thrust. The shock vector control method is capable of vectoring efficiencies of up to $3.3^\circ/\%$ -injection with thrust ratios ranging from 86% to 94% [18].

The counter-flow method uses suction between the trailing edge of the nozzle and an aft collar. The suction creates reversed flow along the collar. The end result is a pressure drop and an increase in velocity near the reversed flow area which provides a thrust differential. This method has higher vectoring efficiencies with thrust ratios between 92% and 97%. A

downside to this method is the need for secondary equipment to provide the suction.

The fluidic throat shifting method has minimal thrust losses, but also suffers from low performance. It is similar to the mechanical throat shifting method discussed in (2.1) in that it works by manipulating the nozzle throat in an effort to turn the flow while it is still subsonic. It is different from mechanical manipulation because it uses jets of secondary flow to create a new effective geometry at the throat. This method is capable of vectoring efficiencies up to $2^\circ/\%$ -injection while maintaining thrust ratios between 94% and 98% [18].

A new method that would manipulate the sonic plane similar to the throat shifting method, but with higher vectoring efficiencies, was put forward by Deere et al. [18]. They used a computational fluid dynamics program, PAB3D, to examine the vectoring abilities created by secondary flow injection in a 2-D dual-throat nozzle. A dual-throat nozzle has two minimum throat areas with a recessed cavity positioned in between. The secondary flow was injected at the upstream minimum area and was held at 6% of the primary flow rate for all the tests. Design variables for this setup included cavity convergence angle, cavity length, fluidic injection angle and upstream minimum height. Vectoring efficiency and thrust ratios were reported for all of the configurations tested.

As detailed in [18], increasing the cavity convergence angle from 9.55° to 20° increased the thrust vectoring efficiency from $1.49^\circ/\%$ -injection to $1.71^\circ/\%$ -injection with a nearly negligible effect on thrust performance. Decreasing the cavity length only slightly improved vectoring abilities, but did improve the thrust ratios by 1.5%. Decreasing the upstream minimum area so that it was equal to the downstream minimum area did increase thrust vectoring efficiency, but resulted in a thrust penalty of 2.2%.

Changing the injection angle resulted in the greatest increase in vectoring efficiency with the smallest impact on thrust ratios. Increasing the injection angle from downstream at 50° to upstream at 150° resulted in a huge increase in thrust vectoring efficiency from $0.84^\circ/\%$ -injection to $2.15^\circ/\%$ -injection with only a 0.6% decrease in thrust ratio. The researchers note that although they were attempting to manipulate the angle and location of the sonic line in the nozzle, vectoring the primary flow is not entirely dependent on this

manipulation alone. Rather, controlling the flow separation within the recessed cavity was key to obtaining large vectoring angles. By controlling the flow separation, they were able to improve upon the traditional throat shifting method of fluidic thrust vectoring.

Deere et al. built and tested a small-scale dual-throat nozzle with thrust vectoring capability [19]. Using the results from [18], additional sources and new work with PAB3D to guide the design, they built a small-scale axisymmetric dual-throat nozzle which would be capable of testing several design parameters. They again tested the effects of cavity length and cavity convergence angle, but also tested the effects of variable nozzle geometries and circumferential span of secondary injection [19].

Variable nozzle geometries were studied simply because a fixed geometry nozzle is not efficient across all operating conditions. The geometries tested had nozzle expansion ratios optimized for operating conditions corresponding with take-off and landing, mid-climb and cruise. The secondary flow was injected at 150° for all cases. The flow injection area was kept constant while two different circumferential spans of 60° and 90° were tested.

Flamm et al. once again discovered that the best thrust vectoring performance was obtained when the two minimum areas are equal. The equal geometry dual-throat nozzle provided a better compromise between vectoring angle and engine thrust performance than the variable geometry nozzle across all nozzle pressure ratios tested. As with the previous computational study, decreasing the cavity length decreased the thrust vectoring efficiency but increased the thrust ratio. Also, increasing the cavity convergence angle slightly improved thrust vectoring efficiency, but negatively impacted the thrust ratio. Data taken during the tests shows that the 60° span of injection resulted in vectoring angles 1.5 to 2° higher than the 90° span.

Eilers et al. have recently investigated thrust vectoring control on a cold-flow aerospike nozzle by means of secondary fluidic injection [20]. Vectoring forces were produced by injecting a secondary fluid into the primary flow field at an angle normal to the nozzle axis. Their experimental aerospike nozzle was truncated at 57% of its full theoretical length. Compressed carbon dioxide was used as the working fluid.

Eilers et al. investigated the effects of injection port location and vectoring effectiveness. Secondary injection test ports were located at 20%, 80% and 90% axial locations. The 90% injection port location produced the highest force amplification factor of 1.4. In other words, the combination of the main flow and the secondary injection produced 40% more vectoring force than the secondary injection is capable of on its own. Specific impulses at this 90% injection location of up to 55 seconds were observed. Across the series of tests performed, the main flow specific impulse averaged approximately 38 seconds. Measurements taken during these experiments indicate that the side force amplification factor was independent of the operating nozzle pressure ratio.

2.3 Exhaust Flow Deflection

An alternative to nozzle manipulation is direct flow manipulation by use of post-nozzle exit vanes or paddles. Examples of aircraft using paddles are shown in Figures 2.3a and 2.3b. An early version of thrust vectoring by way of exhaust flow deflection was found on WWII era German V-2 rockets. The V-2 rockets used four graphite vanes mounted in the hot exhaust flow to steer the rocket toward its intended target. The deflection of the four vanes, shown in Figure 2.2, were controlled by a series of gyroscopes. Though the V-2 often had difficulty hitting its city-sized targets, the gyroscopic guidance system and use of thrust vectoring for maneuvering made the V-2 a very state-of-the-art vehicle for its time [21].

Berrier and Mason researched the effectiveness of a much more modern, paddle-based system in 1988 [22]. They examined the effects of many variables associated with the design and placement of the paddles including paddle curvature, paddle location relative to the nozzle, the number of paddles used and the degree of deflection. They tested several paddle configurations on a small-scale single engine simulation system which used compressed air as the source of its power. It was immediately noticed that spoon-shaped paddles deflected the flow to a greater degree than paddles that had curvature in the radial direction only. This is due to the terminal angle being approximately 9.3° greater than the geometric angle for the spoon shape. The researchers note, however, that for every case, increased flow deflection always resulted in increased thrust losses.

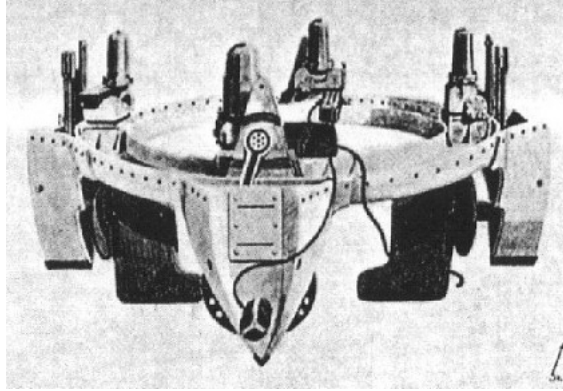


Fig. 2.2: Depiction of graphite thrust vectoring vanes that were used on German V-2 rockets.

The axial position of the paddle hinge had little effect on the resultant thrust vector angle, yet the radial location of the paddle hinge did greatly affect the outcome. As the paddle hinge was moved away from the nozzle exhaust flow, a smaller area of the paddle impinged on the flow, resulting in decreased resultant vector angles. As expected, the direction of the resulting thrust vector angle corresponded precisely with the deflection of one paddle. It was found that the direction of the vectored thrust could be varied to nearly any angle with the use of a second paddle deflected to some corresponding degree.

Berrier and Mason tested two multi-paddle configurations, one having three equiangularly spaced paddles, the other having four. The only advantage to using four paddles was the simplicity with which the thrust could be vectored in only the pitch or only the yaw directions. The three-paddle setup could easily vector in only the pitch direction, but yaw only vectoring was less than straightforward.

The number of paddles had relatively little effect on the resultant thrust vector angle as compared to the number of paddles actually deflected into the flow. As noted previously, the consequence for increasing the resultant vector angle with this form of TVC is a corresponding loss in the available thrust. While the researchers did not show that there is a precise correlation between these values, they did specifically discuss one case for the three-paddle configuration at a nozzle pressure ratio of six. For this case, when one paddle was fully deflected, they measured a resultant vector angle from axial centering of 11.7° with an associated thrust ratio loss of 10%. When they added a second fully deflected paddle, the

resultant vector angle increased to 19° while the thrust ratio loss increased to 21%. These losses are huge and would greatly limit the effectiveness of such a system. As discussed in (2.1) these losses are a result of turning the flow at supersonic speeds.

Despite the limitations of post-nozzle exit paddles, two full-scale flight demonstration projects employed a three-paddle configuration: NASA's F-18 High Alpha Research Vehicle (HARV) and the international X-31 Enhanced Fighter Maneuverability demonstrator. These two vehicles demonstrated that post-nozzle exit paddles could be used on a limited basis to enhance fighter aircraft maneuverability. The paddles have the benefit of no measurable thrust loss when not deflected. Despite the significant loss of thrust when using the paddles, the two vehicles were able to operate for a brief time in the post-stall flight envelope, greatly enhancing their maneuverability.

Measurements taken by the F-18 HARV team validated the thrust loss effects shown experimentally by Berrier and Mason. Additionally, they determined that paddle spacing (relative to each other) was a more important design feature than paddle size. They noticed that paddles located closer to each other allowed less flow to leak between them and thus were more effective at turning the flow [23]. Figure 2.3a shows the F-18 HARV conducting ground-based vectoring tests. The main exhaust plume is clearly deflected upwards while some of the flow can be seen leaking between the paddles.



(a) NASA's F-18 HARV demonstrating thrust vectoring achieved using movable paddles.



(b) The X-31 and its set of movable paddles mounted in the engine's exhaust.

Fig. 2.3: Examples of thrust vectoring that used the exhaust flow deflection technique.

The thrust vectoring system on the X-31, shown in Figure 2.3b, was so effective that the research team went beyond the original scope of the vehicle design and conducted four quasi-tailless flight tests. The idea behind these tests was that the thrust vectoring system could be used to add the stability normally required of the vertical stabilizer. If the vertical stabilizer could be reduced or even removed altogether, enormous benefits from reductions in weight, zero-lift drag and radar observability could be realized. Using the digital flight control system, the researchers were able to use the rudder to remove the normally stabilizing effects of the vertical stabilizer. They then added a system overlay that used the ailerons and the TVC system to restore stability to the aircraft. All four quasi-tailless flight tests were an extreme success and exceeded all expectations [24].

Chapter 3

Final Vehicle Design

Though the primary research for this thesis is thrust vectoring for attitude control, a brief overview of the entire ESLRV design is presented in this chapter. Included in this overview is a description of the vehicle's landing gear, gimbal system, inner and outer platform propulsion systems and the outer platform's power and control systems.

3.1 Vehicle Overview

Figure 3.1 shows a functional block diagram of the overall vehicle design. The calculations, decisions, and considerations used to arrive at this final design are presented in greater detail in [25] and [26]. In Figure 3.1, the primary vehicle components are listed, with arrows showing the flow of information and overall functional interdependence. Figure 3.2 presents a 3-D model showing the final design configuration for the ESLRV with many of the major components labeled. The landing gear are hinged at the base and angled at 45° to avoid the maximum downwash velocity area produced by the rotors. Small spring-loaded shock absorbers are used to reduce landing loads.

Figures 3.1 and 3.2 illustrate the functional and partial physical separation of two primary sections of the vehicle: an outer platform containing the vehicle maneuvering controls and an inner platform that houses the gravity offset system. The inner platform serves to offset $5/6^{th}$ of the vehicle's weight at hover while the outer platform supports the remaining $1/6^{th}$ of the weight and provides maneuvering controls. The two platforms feature a gimbal design, which functions to uncouple the inner platform rotational dynamics from the outer platform while allowing for synchronous translational dynamics. Figure 1.5 depicts the gimbal design.

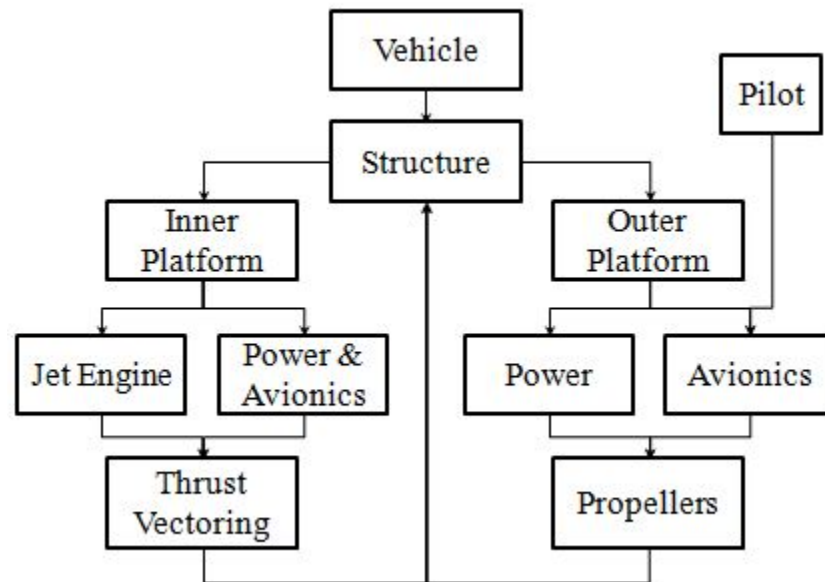


Fig. 3.1: Vehicle functional diagram.

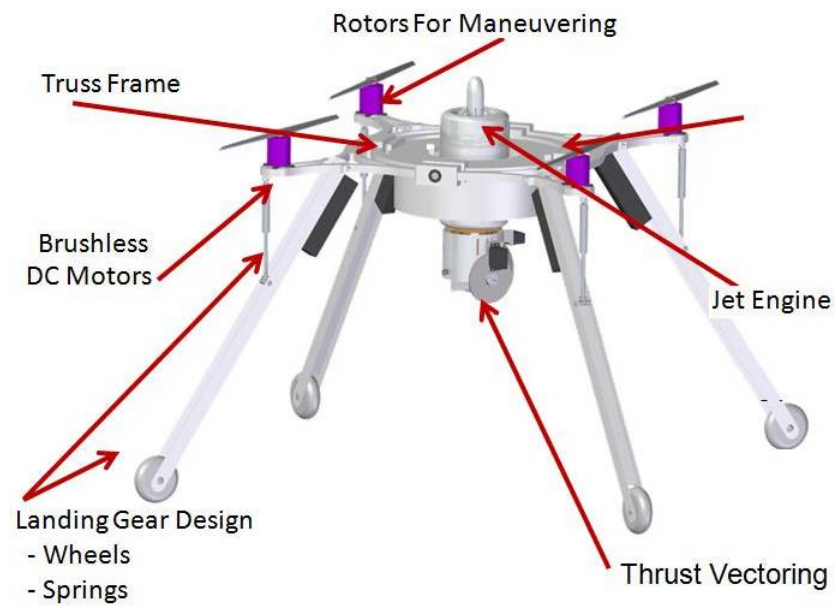


Fig. 3.2: Final design configuration.

In order to completely uncouple the inner platform rotational dynamics from the outer platform while allowing for synchronous translational dynamics, each platform was designed to be a self-contained system, with its own power and communications hardware. This eliminates the need to have cables and other hardware cross over the gimbals which would interfere with the rotational dynamics. The outer platform holds all of the maneuvering rotors and associated drive-train components, while the inner platform houses the jet engine and associated support equipment. The fuel tank for the jet engine is integrated into the structure of the inner ring. The outer gimbal ring is oriented to pivot around the roll axis of the vehicle, and the inner gimbal ring is oriented to pivot about the pitch axis of the vehicle.

The central feature of this vehicle is the JF-170 jet engine. The JF-170 engine is an amateur-class, radio-controlled (RC), single shaft turbojet with an annular combustor. A single-stage axial flow turbine drives a single-stage centrifugal compressor. The shaft is supported by two fuel/oil lubricated, annular contact bearings. A full-authority digital engine control system (FADEC) controls the turbine speed by dictating the fuel flow rate delivered by the fuel pump. The turbine runs on K-1 grade kerosene and starts on propane.

The decision was made very early in the program to eliminate the hydrogen peroxide maneuvering thrusters employed in the LLRV/LLTV design. This corrosive and toxic monopropellant would require extraordinary safety and handling procedures that are incompatible with an “open” university design project. Cold-gas thrusters were quickly eliminated because there was insufficient lift capability to meet the project’s required flight duration. Thus, the lift thrusters were replaced by a propeller-powered quad-rotor system.

3.2 Outer Platform: Vehicle Maneuvering System

The maneuvering system design for the ESLRV attempted to match the general layout of the LLRV thrusters, and provides the means to maneuver the craft up, down, forward, back, left and right with the use of four propellers in a configuration called a quadrotor. Quadrotors can use fixed-pitch blades – blades whose angle of attack is permanently fixed – to achieve precise maneuvering. Control of vehicle motion is achieved by modulating the

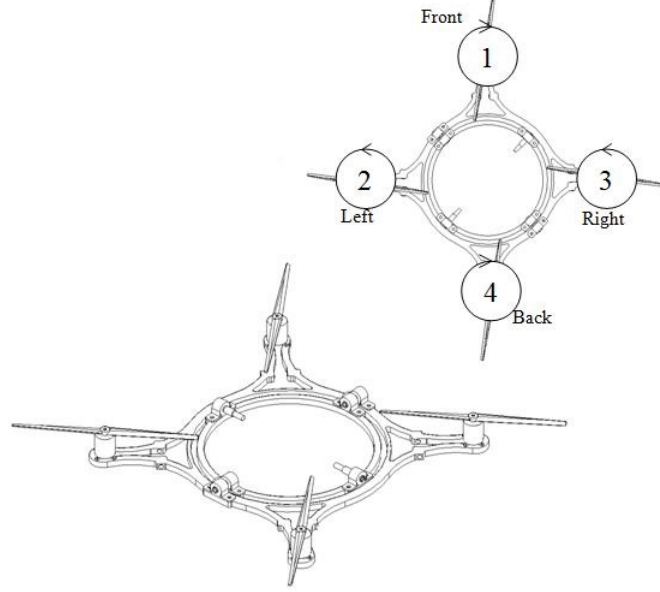


Fig. 3.3: Quadrotor propeller layout.

rotational speed of each rotor to vary the thrust and torque produced by each rotor.

Figure 3.3 depicts the rotor layout on the outer platform support structure. In this design, the front and back propellers (1, 4) rotate in opposite directions than do the left and right (2, 3) propellers. This counter-rotating scheme allows for precise control and trim of the vehicle yawing rate. A left-to-right (2, 3) differential throttle produces a rolling moment about the center of the platform and front-to-back (1, 4) differential throttle produces a pitching moment. Simultaneously increasing (decreasing) throttle on the front and back propellers (1, 4) while decreasing (increasing) the throttle on the left and right propellers (2, 3) produces a yawing motion. Collective throttle (1, 2, 3, and 4) is used to allow the vehicle to climb or descend. On Figure 3.3, the circular arrows superimposed on each rotor show the direction of rotation.

3.2.1 Outer Platform: Control System

Initially, it was thought that the quadrotor system could be flown open-loop using a conventional RC transmitter and receiver designed for model aircraft. Following the procedure developed by the VALASARAPTOR project at the University of Colorado [27],

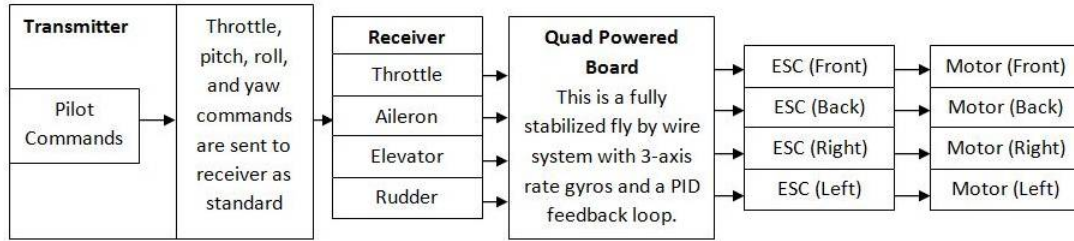


Fig. 3.4: QuadPowered[®] control system functional diagram.

the throttle, rudder, aileron, and flap controls on the transmitter were internally re-mapped to control the four motor throttle levels. This mapping allowed, at least in theory, the quadrotor to be flown as if it were a conventional RC aircraft. This open-loop control mixing scheme resulted in a quadrotor configuration that was unflyable. Command latencies were so significant that the rotational rate onsets could not be negated by pilot input alone. Closed-loop platform control, hosted locally on the vehicle, was required to maintain outer platform stability.

Fortunately, for the ESLRV application, a control and logic board specifically designed for stabilization and control functions for quadrotor systems is commercially available. This device, the QuadPowered[®] board manufactured by Quadpowered Precision Control Systems[®], limits vehicle rotation rates using a proportional, integral, derivative (PID) control system. Feedback measurements include a two-axis rate-gyro for the pitch and roll axes, and a single axis rate-gyro for the yaw axis. Three independent control loops are executed by a microprocessor installed on the board. The microprocessor receives throttle, pitch, roll, and yaw signals from a standard RC transmitter, mixes the commands appropriately, and sends out a pulse-width modulation (PWM) signal to each of the four rotor's electronic speed controller (ESC). Figure 3.4 presents a functional block diagram of the QuadPowered[®] board control logic.

3.2.2 Outer Platform: Power Distribution

All components for the maneuvering system were arranged on the outer platform. Figure 3.5 presents a block diagram of the outer platform power distribution system. The

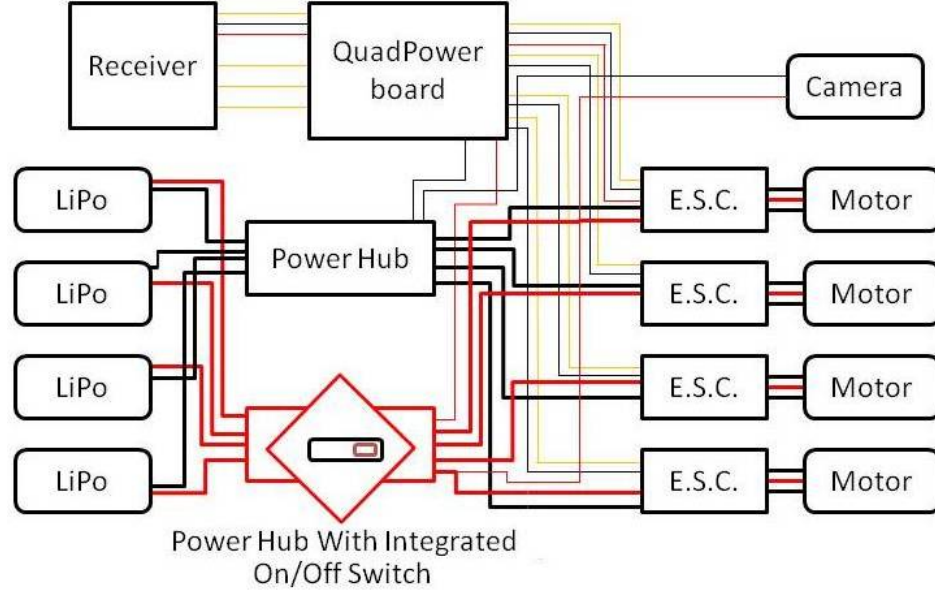


Fig. 3.5: Outer platform wiring diagram.

outer platform is powered by four, 3-cell lithium-polymer (Li-Po) batteries operating at a nominal 11.4 volts. Each battery has a full charge capacity of 3.25 amp-hours. Positive and negative terminals for each battery were connected in parallel to a power hub. This arrangement provides uniform voltage to each ESC and motor. The QuadPowered® board receives power from two sources: the power hub, and one ESC that has an integrated 5-volt battery eliminating circuit (BEC, or more commonly, a DC-to-DC converter) in series with the ESC drive signal. The onboard RC receiver is powered by the QuadPowered® board.

3.3 Inner Platform: Gravity Offset

As described in (1.1.1) and (3.1), the function of the gravity-offset system is to lift $\frac{5}{6}^{th}$ of the vehicle weight without contributing to horizontal linear acceleration. The jet engine used for gravity offset, the JF-170 Rhino, is pictured in Figure 3.6. Automatic start and stop procedures, as well as turbine speed, are controlled by the FADEC. The FADEC controls engine speed by regulating the voltage supplied to the fuel pump. The user controls the throttle setting of the engine by means of a standard RC PWM signal.



Fig. 3.6: The JF-170 Rhino: a single-stage, axial flow, centrifugal RC turbine engine.

Engine control is supported by two primary feedback sensors, a magnetic angular velocity sensor, and an exhaust gas temperature thermocouple. Additional diagnostic measurements include engine run time and power delivered to the fuel pump. All onboard sensor data can be monitored via a standard RS-232 serial output. The FADEC serial data was continuously monitored and logged during static and ground tests using a wireless telemetry link. A detailed description of the inner platform thrust vectoring system will be deferred to (5).

Chapter 4

Static Engine Testing and Characterization

This chapter discusses the static tests performed to characterize the JF-170 engine. This particular engine is normally used in hobby-class RC airplanes and is by no means a precision device. It is balanced so that it runs smoothly, but there was no guarantee that it would perform exactly as advertised, or even consistently. Performance characteristics of the engine needed to be fully understood before a thrust vectoring device be could designed. Specifics such as thrust, fuel consumption rate, exhaust gas temperature and exhaust gas velocity needed to be quantified and tested for repeatability.

The design and calibration of the test stand is presented along with static test results. A numerical analysis of the test results was completed to establish the accuracy of the test stand. Additionally a computational fluid dynamics (CFD) study was performed on the nozzle to further investigate nozzle flow dynamics. The results of this study are presented in the last section of this chapter.

4.1 Test Platform

All engine static tests were performed in the Engineering Technology Department's jet engine test cell on USU's campus. Commercially-available test stands were found to be excessively expensive and had structural support mechanisms unsuitable for mounting the JF-170 Rhino. Consequently, a custom-made, portable test stand was designed and built to support the needs of the ESLRV project.

4.1.1 Overview and Instrumentation

The custom-built test stand features a 6-degree-of-freedom (6-DOF) load balance, a traversing engine exit plume pitot probe, a static pressure port at the nozzle exit, and a

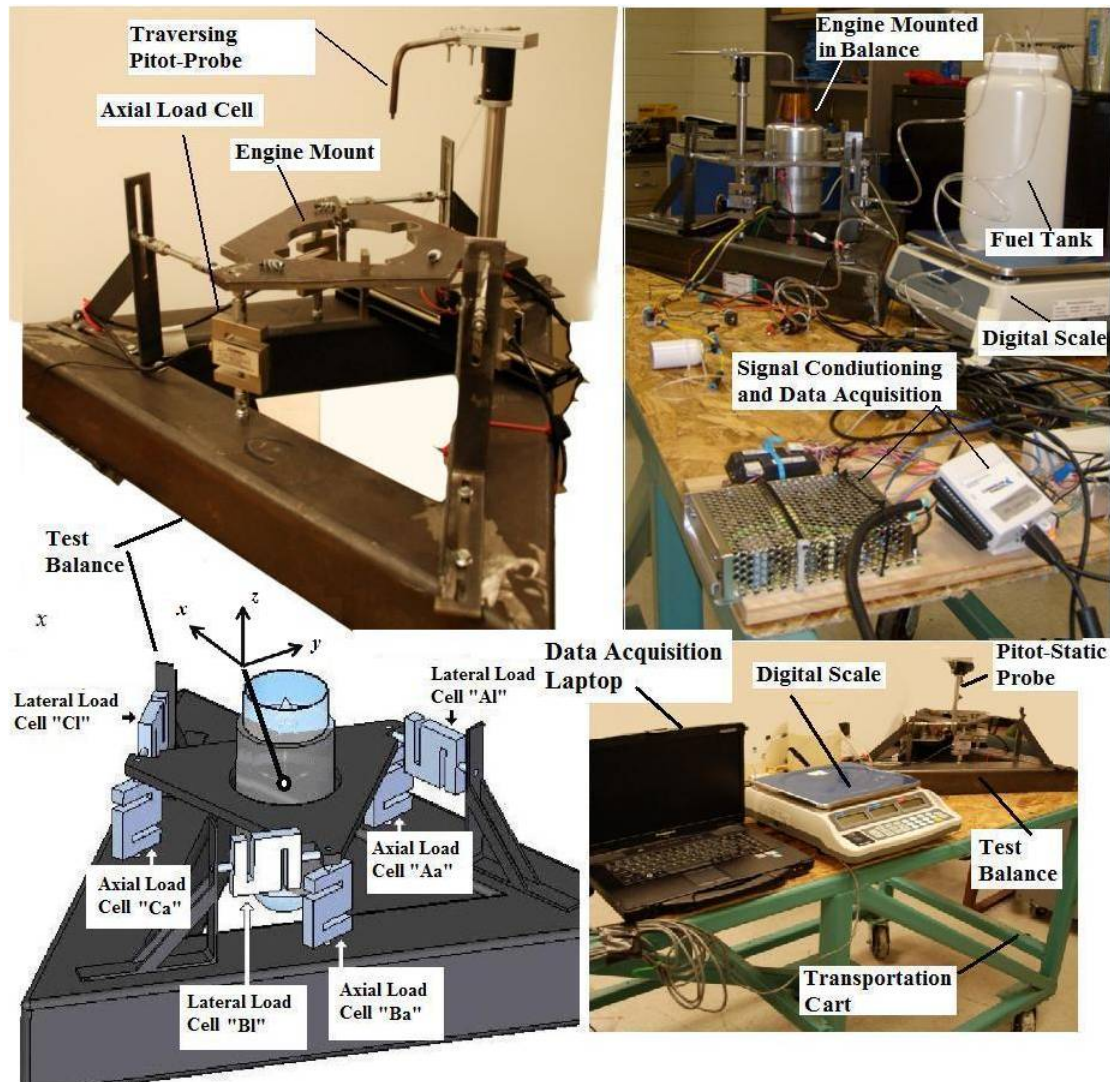


Fig. 4.1: Jet engine test stand showing various components.

digital scale to measure fuel consumption. Figure 4.1 presents an image collage of the test platform with many of these features labeled. The thrust stand was designed so that the engine exhaust plume exits vertically, and the thrust acts downward into the test cart. This orientation prevents the engine's exhaust from stirring up debris that could then be ingested by and cause damage to the engine.

A total of six load cells were used on the test stand to measure the jet engine's axial and lateral forces. Axial loads are measured with three Omegadyne® 100 lbf (444.8 N) load cells, while lateral loads are measured with three Omegadyne® 25 lbf (112.2 N) load

cells. The stagnation pressure at the pitot probe is measured with a 0-30 psia (0-206.8 kPa) Omegadyne[®] pressure transducer. The static pressure at the nozzle exit plane is measured with an identical transducer ranged from 0-15 psia (0-103.4 kPa). The load cells and pressure transducers are connected to three National Instruments[™] (NI) 14-bit stand-alone data acquisition (DAQ) devices. Three DAQ devices are necessary to provide the required six differential and two-single ended channels for the load cells and pressure transducers.

The fuel mass and massflow was measured in real-time using a Weighmax[®] digital scale. The RS-232C serial bus output from this scale was monitored during testing to provide a continuous measure of the fuel consumption rate. Relevant manufacturer's specifications for operating range and accuracy for each of the instruments used on the test stand are listed in Table 4.1. A laptop computer running NI LabVIEW[™] 9.0 was used to operate the jet engine as well as capture, synchronize, process, and log data from the load cells, pressure transducers, serial output data from the scale and data output from the FADEC.

As mentioned earlier, the thrust stand was designed so the engine exhaust plume exits vertically, and the thrust acts downward into the test cart. The load cells are divided into axial [Aa, Ba, and Ca] and lateral [Al, Bl, and Cl] groups based on the orientation of their sensing axes. The coordinate system for the thrust stand, pictured in Figure 4.1, is defined with the z-axis acting vertically upward along the axial centerline of the engine. Thus, the thrust acts in the negative z-direction. The y-axis runs perpendicular to and intersects with the longitudinal axis of the axial load cell, Aa. The x-axis completes the system. A positive rotational moment about the y-axis is equivalent to a positive pitching moment on the vehicle; a positive moment about the z-axis is equivalent to a positive yawing moment on the vehicle; and a positive moment about the x-axis is equivalent to a positive rolling moment on the vehicle. The origin of the coordinate system is centered in the plane of the engine mounts, and lies along the sensing axes of the lateral load cells.

Table 4.1: Manufacturer Specifications for Thrust Stand Instrumentation

Instrument Model	Operating Range	Accuracy
Lateral Loads LCCA-25	$\pm 25 \text{ lbf}$ ($\pm 111.2 \text{ N}$)	$\pm 0.25\%$ of Full-Scale
Axial Load Cells LCCD-100	$\pm 100 \text{ lbf}$ ($\pm 444.8 \text{ N}$)	$\pm 0.25\%$ of Full-Scale
DAQs USB-6009	$\pm 1.0 \text{ V}$	$\pm 0.5 \text{ mV}$ RMS, 14-bit res.
Fuel Mass W-C030	0 - 6.6 <i>lbf</i> (0 - 3 <i>kgf</i>)	$\pm 0.0011 \text{ lbf}$ ($\pm 0.0005 \text{ kgf}$)
Static Pressure PX142-015A5V	0 - 15 <i>psia</i> (0 - 103.4 <i>kPa</i>)	$\pm 0.15\%$ of Full-Scale
Stagnation Pressure PX142-030A5V	0 - 30 <i>psia</i> (0 - 206.8 <i>kPa</i>)	$\pm 0.15\%$ of Full-Scale

4.1.2 Traversing Pitot Probe

The traversing probe was designed to sweep across the engine plume centerline and provide two-dimensional stagnation pressure, velocity, and mass flow distribution data very near the nozzle exit plane. A single-axis position controller, mounted on a rack-and-pinion tracking system, was used as the drive mechanism. Figure 4.2 shows this drive mechanism. A 5 W motor is mounted on top of the traversing block. The motor gear meshes with the block's external gear and carries the motor torque to the rack-and-pinion inside the block.

Linear position along the track is sensed by a ThinPot[®] linear potentiometer. This sensor is constructed from a polyester substrate mounted with pressure-sensitive adhesive. A contact wiper anchored on the traversing block applies pressure to the polyester substrate. As the block moves, the linear potentiometer changes resistance, from which the location of the block can be determined. A commercial H-bridge circuit is used to control the direction and speed of the probe. Detailed design features regarding this traversing probe can be found in Appendix F of [25].

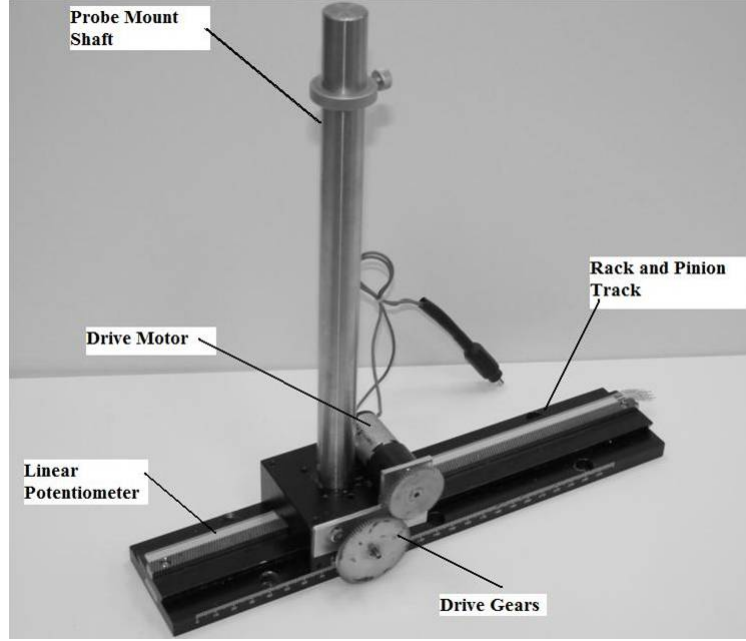


Fig. 4.2: Traversing pitot probe drive mechanism.

4.1.3 Jet Engine Thrust Stand Calibration

Because of the geometric complexity of the test stand, the entire test stand was calibrated for output forces and moments as a function of the six load cell readings. Following the procedure developed by Schaefermeyer, Whitmore and Wright [26], the test stand was modeled as a linear perturbation model of the form

$$\begin{bmatrix} F_x \\ F_y \\ F_z \\ M_x \\ M_y \\ M_z \end{bmatrix} = \begin{bmatrix} \frac{\partial F_x}{\partial V_{Aa}} & \frac{\partial F_x}{\partial V_{Ba}} & \frac{\partial F_x}{\partial V_{Ca}} & \frac{\partial F_x}{\partial V_{Al}} & \frac{\partial F_x}{\partial V_{Bl}} & \frac{\partial F_x}{\partial V_{Cl}} \\ \frac{\partial F_y}{\partial V_{Aa}} & \frac{\partial F_y}{\partial V_{Ba}} & \frac{\partial F_y}{\partial V_{Ca}} & \frac{\partial F_y}{\partial V_{Al}} & \frac{\partial F_y}{\partial V_{Bl}} & \frac{\partial F_y}{\partial V_{Cl}} \\ \frac{\partial F_z}{\partial V_{Aa}} & \frac{\partial F_z}{\partial V_{Ba}} & \frac{\partial F_z}{\partial V_{Ca}} & \frac{\partial F_z}{\partial V_{Al}} & \frac{\partial F_z}{\partial V_{Bl}} & \frac{\partial F_z}{\partial V_{Cl}} \\ \frac{\partial M_x}{\partial V_{Aa}} & \frac{\partial M_x}{\partial V_{Ba}} & \frac{\partial M_x}{\partial V_{Ca}} & \frac{\partial M_x}{\partial V_{Al}} & \frac{\partial M_x}{\partial V_{Bl}} & \frac{\partial M_x}{\partial V_{Cl}} \\ \frac{\partial M_y}{\partial V_{Aa}} & \frac{\partial M_y}{\partial V_{Ba}} & \frac{\partial M_y}{\partial V_{Ca}} & \frac{\partial M_y}{\partial V_{Al}} & \frac{\partial M_y}{\partial V_{Bl}} & \frac{\partial M_y}{\partial V_{Cl}} \\ \frac{\partial M_z}{\partial V_{Aa}} & \frac{\partial M_z}{\partial V_{Ba}} & \frac{\partial M_z}{\partial V_{Ca}} & \frac{\partial M_z}{\partial V_{Al}} & \frac{\partial M_z}{\partial V_{Bl}} & \frac{\partial M_z}{\partial V_{Cl}} \end{bmatrix} \begin{bmatrix} V_{Aa} \\ V_{Ba} \\ V_{Ca} \\ V_{Al} \\ V_{Bl} \\ V_{Cl} \end{bmatrix} \quad (4.1)$$

In Equation 4.1, the vector $[F_x, F_y, F_z, M_x, M_y, M_z]$ contains the forces and moments to be calculated when the thrust stand is loaded. The vector $[V_{Aa}, V_{Ba}, V_{Ca}, V_{Al}, V_{Bl}, V_{Cl}]$ contains the output voltages from the six axial and lateral load cells shown in Figure 4.1. The linear system of Equation 4.1 assumes that the voltage readings for the six load sensors

have been adjusted so that a zero-load on the thrust stand produces no load cell output. The thirty-six elements of the Jacobian matrix define the externally applied forces and moments in terms of the sensed (and zeroed) load cell outputs. The calibration procedure reverses the process with multiple known external forces and moments applied to the thrust stand, while corresponding sensor readings are logged. Assuming a set of N calibration inputs,

$$\tilde{F} = \left\{ \begin{bmatrix} F_x \\ F_y \\ F_z \\ M_x \\ M_y \\ M_z \end{bmatrix}_1 \begin{bmatrix} F_x \\ F_y \\ F_z \\ M_x \\ M_y \\ M_z \end{bmatrix}_2 \dots \begin{bmatrix} F_x \\ F_y \\ F_z \\ M_x \\ M_y \\ M_z \end{bmatrix}_N \right\}, \quad (4.2)$$

and a corresponding set of sensor outputs,

$$\tilde{V} = \left\{ \begin{bmatrix} V_{Aa} \\ V_{Ba} \\ V_{Ca} \\ V_{Al} \\ V_{Bl} \\ V_{Cl} \end{bmatrix}_1 \begin{bmatrix} V_{Aa} \\ V_{Ba} \\ V_{Ca} \\ V_{Al} \\ V_{Bl} \\ V_{Cl} \end{bmatrix}_2 \dots \begin{bmatrix} V_{Aa} \\ V_{Ba} \\ V_{Ca} \\ V_{Al} \\ V_{Bl} \\ V_{Cl} \end{bmatrix}_N \right\}, \quad (4.3)$$

Equation 4.1 can be written as the 6 x N dimensioned matrix equation

$$\tilde{F} = J\tilde{V} \quad (4.4)$$

where J is the 6 x 6 Jacobian. Post multiplying both sides of Equation 4.4 by \tilde{V}^T produces the 6 x 6 dimensioned system

$$\tilde{F}\tilde{V}^T = J \left(\tilde{V}\tilde{V}^T \right) \quad (4.5)$$

Post multiplying both sides of this last equation by $(\tilde{V}\tilde{V}^T)^{-1}$ gives the least squares estimate [28] for the Jacobian matrix:

$$\hat{J} = \tilde{F}\tilde{V}^T (\tilde{V}\tilde{V}^T)^{-1} \quad (4.6)$$

Given an arbitrary set of load cell readings (zeroed for the no load case), the force and moment outputs from the thrust stand can be calculated as:

$$\begin{bmatrix} F_x \\ F_y \\ F_z \\ M_x \\ M_y \\ M_z \end{bmatrix} = \hat{J} \begin{bmatrix} V_{Aa} \\ V_{Ba} \\ V_{Ca} \\ V_{Al} \\ V_{Bl} \\ V_{Cl} \end{bmatrix} \quad (4.7)$$

Prescribed calibration forces and moments are applied to the test stand using known calibration weights. Three axial and three lateral loads are applied at any one time, and the resulting forces and moments are calculated using the known input geometry. The axial calibration weights are placed over 0.5 inch (12.7 mm) diameter steel alignment rods which are approximately 18 inches (0.46 m) in length. These rods are threaded onto the same threaded rod that holds the corresponding axial load cell to the engine mounting plate. The masses of these rods are included as part of the calibration load. The lateral calibration loads are applied by weights suspended on lines routed through pulleys and attached to the engine mounting plate. Figure 4.3 shows the location of the weights and pulleys used to apply the calibration inputs to the test stand.

In a typical calibration procedure, system zeroes are determined by reading the load cell voltages for ten seconds with no loads applied and averaging the time history results. These zeroes are analytically removed from the load cell voltage readings. Next, alignment rods are threaded onto each of the axial calibration load points. Each rod has a mass of approximately 1.7 *lbm* (0.8 *kg*). Next, 6.6 *lbm* (3.0 *kg*) masses are placed on each of the

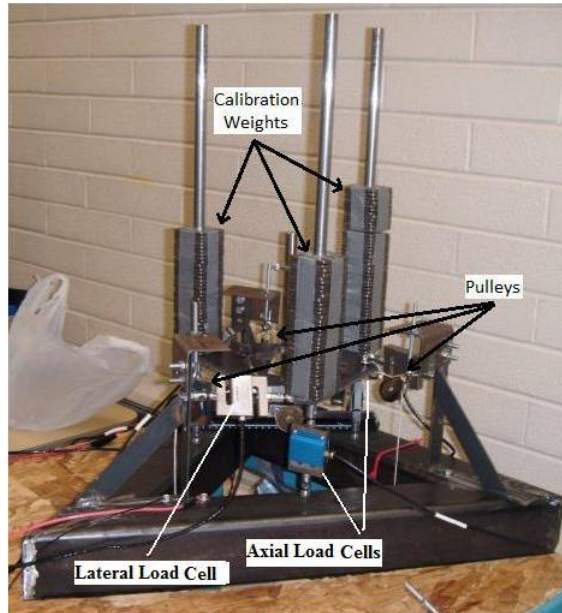


Fig. 4.3: Calibration forces and moments being applied to the thrust stand.

rods. This arrangement creates a total axial force of approximately 24.9 lbf (110.8 N). A 1.0 lbm (0.45 kg) mass is subsequently placed on the axial rod above load cell *Aa*. The six load cell voltages and reference loads are logged. The 1.0 lbm mass is sequentially moved to the axial rods above load cell *Ba*, and then load cell *Ca*. Voltages and loads are logged in each case. Next, a 1.25 lbm (0.57 kg) mass is applied to lateral calibration load point *Al* through pulley A. Data is logged and the process is repeated for lateral calibration points *Bl* and *Cl*. The applied weights are sequentially increased to generate the calibration data set.

Table 4.2 shows a typical calibration matrix generated using this procedure. A negative reading indicates the load cell is under compression; a positive reading indicates a tensile load on the sensor. The rows of this matrix represent the sensitivity of the output loads and moments to the individual load cell millivolt readings. Notice that the matrix is not particularly sparse, indicating that each load cell is affected by any given load and that the outputs from each load cell contribute to the overall load and moment calculations.

Table 4.3 shows the normalized sensitivity of each load or moment to the individual load cell outputs. The values in this table were calculated for each row by taking the square

Table 4.2: Typical Jet Engine Test Stand Calibration Matrix: Individual Load Cell mV Readings

	Load Cell <i>Aa</i>	Load Cell <i>Ba</i>	Load Cell <i>Ca</i>	Load Cell <i>Al</i>	Load Cell <i>Bl</i>	Load Cell <i>Cl</i>
F_x	-663.47	440.67	327.82	-3815.97	2124.60	1865.77
F_y	38.53	-890.14	935.53	-404.17	-3137.27	3390.67
F_z	-14806.02	-15058.92	-15526.69	-411.71	-890.79	-837.60
M_x	2063.50	-1005.05	-1046.50	14.72	25.21	20.86
M_y	-27.17	1899.09	-1778.54	-22.61	-3.92	-23.66
M_z	-74.41	-134.87	-150.76	-470.58	-531.57	-539.38

Table 4.3: Typical Jet Engine Test Stand Calibration Matrix: Normalized Sensitivity

	(1) Load Cell <i>Aa</i>	(2) Load Cell <i>Ba</i>	(3) Load Cell <i>Ca</i>	(4) Load Cell <i>Al</i>	(5) Load Cell <i>Bl</i>	(6) Load Cell <i>Cl</i>
(1) F_x	0.137	0.091	0.068	0.794	0.440	0.387
(2) F_y	0.008	0.185	0.194	0.084	0.652	0.704
(3) F_z	0.564	0.574	0.592	0.016	0.034	0.032
(4) M_x	0.818	0.398	0.415	0.006	0.010	0.008
(5) M_y	0.010	0.730	0.683	0.009	0.002	0.009
(6) M_z	0.081	0.147	0.164	0.513	0.580	0.588

root of the sum of the squares for the six elements in the row, and dividing this value back into each element of the row. The magnitudes show the relative contribution of the load cell output to the force or moment calculation. For example, the major contributors to the yawing moment calculation, M_z (row 6), are the lateral load cell outputs (columns 4-6). Conversely, the pitching moment calculation, M_y , is most sensitive to the output from the axial load cells Ba and Ca , and is almost completely insensitive to the outputs from the lateral load cells. As expected, the thrust, $-F_z$, is most sensitive to the outputs from the axial load cells, and almost completely insensitive to the lateral load cell outputs.

3.1.3.1 Calibration Uncertainty Estimates

A total of thirty-two independent calibration data sets were generated. Collectively, these data were used to calculate the Jacobian (calibration) matrix for the system. Four of these load cases imparted identical forces and moments to the test stand and were used to estimate the statistical uncertainty of the calibration.

Table 4.4: Statistical Evaluation of Four Identical Load Calibration Cases

	$F_x (N)$	$F_y (N)$	$F_z (N)$	$M_x(N-m)$	$M_y(N-m)$	$M_z(N-m)$
Applied Load	-10.556	9.234	-146.273	1.580	1.398	-0.773
Measured Loads:						
Case 1	-10.411	8.798	-144.808	1.550	1.364	-0.714
Case 2	-10.021	8.874	-145.257	1.591	1.409	-0.717
Case 3	-10.230	9.102	-147.043	1.703	1.411	-0.729
Case 4	-10.076	9.084	-144.644	1.796	1.304	-0.729
Mean	-10.184	8.964	-145.438	1.660	1.372	-0.722
Standard Deviation	0.175	0.152	1.101	0.112	0.050	0.008
Error	0.372	-0.270	0.835	0.081	-0.026	0.011
% Error	3.65%	3.01%	0.57%	4.86%	1.91%	1.50%

Table 4.4 shows the statistical results from the four identical load cases. These data points were used to approximate the 95% confidence interval on the mean error estimate using the confidence interval formula,

$$S_{\bar{x}} = \frac{t_{\gamma}\sigma_x}{\sqrt{n}} \quad (4.8)$$

$$CONF_{\gamma} \{ \bar{x} - S_{\bar{x}} \leq \nu \leq \bar{x} + S_{\bar{x}} \} \quad (4.9)$$

where $S_{\bar{x}}$ is the mean error confidence interval, σ_x is the sample standard deviation, and t_{γ} is the t-distribution variable corresponding to a double-ended probability with $n-1$ degrees of freedom [29]. For this data set, $n = 4$, $\gamma = 0.95$ corresponding with the 95% confidence interval and $t_{95} = 3.19$. Using these values, the confidence intervals calculated for the data set in Table 4.4 are shown in the second column of Table 4.5. The mean error is a systematic error and is subtracted from the results of calculations from Equation 4.7. The confidence interval is the random uncertainty in the test-stand measurements.

The calibration weights were measured using the Weighmax[®] scale described in (4.1.1). The manufacturer's estimated scale error is ± 0.005 kg. The uncertainty in the moment arm points on the lateral load cells is estimated at $\pm 1/16^{th}$ inch (± 1.6 mm). Factoring in the

Table 4.5: Test Stand Mean Measurement Error Uncertainty Estimates

Measurement	Mean Error \pm Confidence Interval	Total Measurement Uncertainty Estimate
$F_x (N)$	0.372 ± 0.278	$\pm 0.279 N (\pm 2.64\%)$
$F_y (N)$	-0.270 ± 0.242	$\pm 0.242 N (\pm 2.62\%)$
$F_z (N)$	0.835 ± 1.752	$\pm 1.752 N (\pm 1.2\%)$
$M_x (N\cdot m)$	0.081 ± 0.177	$\pm 0.177 N\cdot m (\pm 11.23 \%)$
$M_y (N\cdot m)$	-0.263 ± 0.080	$\pm 0.082 N\cdot m (\pm 5.83 \%)$
$M_z (N\cdot m)$	0.108 ± 0.012	$\pm 0.020 N\cdot m (\pm 2.59\%)$

uncertainty in the scale measurements and moment arm measurements as systematic errors, and root sum-squaring these errors with the random uncertainties from column two of Table 4.5, the total estimated test stand measurement uncertainties are calculated. These total measurement uncertainty estimates are listed in the third column of Table 4.5.

4.2 Static Thrust Test Results

A total of six different static thrust tests were performed to characterize the performance of the JF-170 Rhino. So many tests were required due to the complexity of both the jet engine operation and the test stand. The initial tests provided significant insight into the performance quirks of the jet engine as well as the bugs in the instrumentation equipment. Once a basic understanding was gained of the jet engine performance properties, the thrust vectoring vanes were designed.

4.2.1 Jet Engine Performance

The LabVIEWTM signal processing code allowed for the acquisition and storage of data from many sensors. It allowed for a chronological comparison of jet engine performance data vs. the input engine control settings. One of the more important sets of data needed for comparison was the actual thrust vs. engine revolutions per minute (RPM) curve. The manufacturer data for the JF-170 Rhino was available, but being a hobby class engine, this data needed to be verified. Also of interest was the effect of the thrust vectoring system on the total engine thrust.

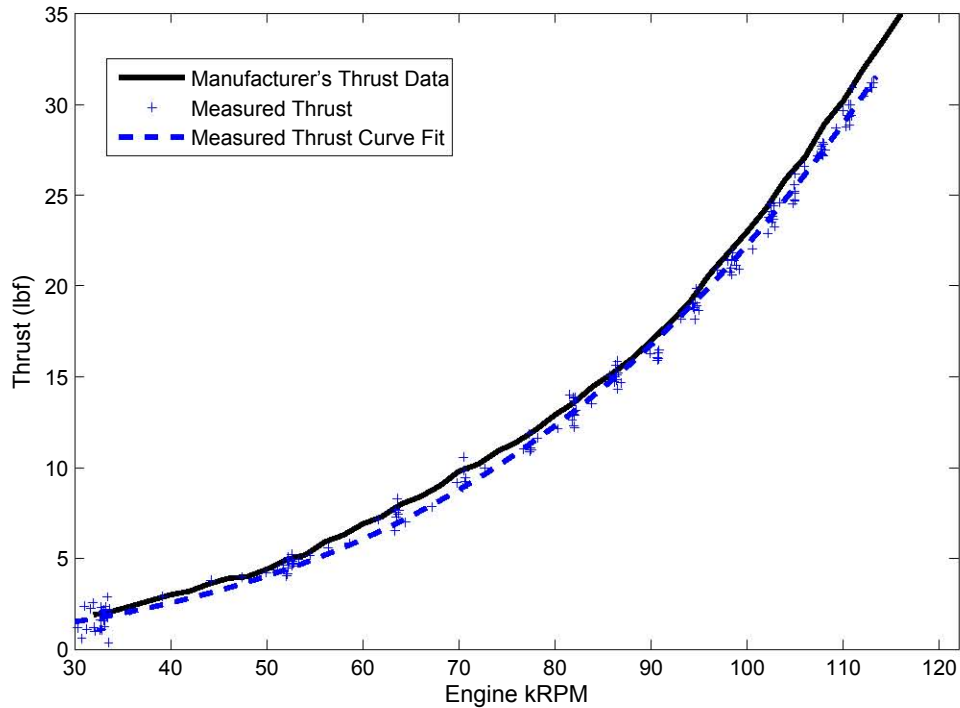


Fig. 4.4: JF-170 Rhino thrust vs. RPM curve.

The measured thrust data was plotted against engine RPM measured by the FADEC. Figure 4.4 compares the original manufacturer's thrust vs. RPM profile [12] against the measured thrust vs. RPM profile with no vectoring system installed. The RPM (x-axis) is plotted in units of 1000s of RPM. A cubic polynomial curve fit was applied to the data points seen in Figure 4.4 to obtain the dashed line. The measured thrust is slightly lower than, but closely parallels the manufacturer's published data. The differences are likely due to the relatively high altitude operation of the JF-170 Rhino in the test cell at USU. The elevation at USU is approximately 4,700 feet. The manufacturer's data were obtained for near sea level conditions. Without the thrust vectoring system installed, the engine produces approximately 32 lbf of thrust at full throttle (115,000 RPM).

Figure 4.5 shows the measured fuel mass flow consumption as a function of the engine throttle setting. Fuel consumption was calculated by numerically differentiating the fuel mass time-history profiles, plotting as a function of throttle, and curve-fitting the results.

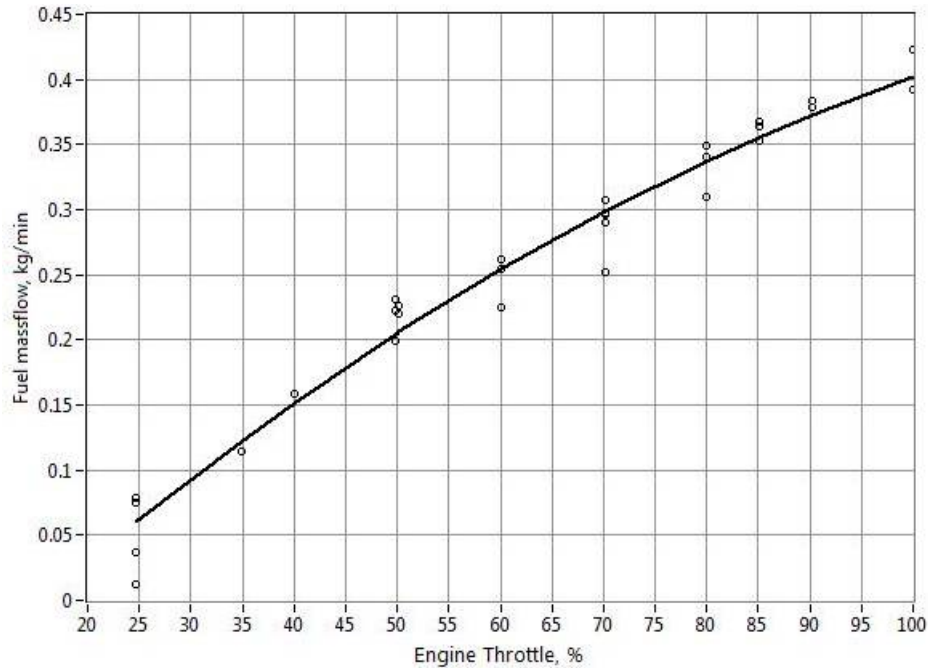


Fig. 4.5: Measured fuel massflow as a function of throttle setting.

The ESLRV design assumes a nominal engine thrust level of 85%. Operating at an 85% throttle setting (115,000 RPM), the jet engine produces approximately 26 lbf thrust (approximately one pound less than advertised) and allows for a safety margin should the outer platform’s lift system fail. At this throttle setting, the fuel mass-flow rate is approximately 0.36 kg/min.

4.2.2 Exit Plane Velocity Profile

The JF-170 Rhino has an unusual nozzle exit plane velocity and Mach number profile. This profile, shown in Figure 4.6, has a large momentum defect near the axial centerline. The source of this momentum defect is unclear, but it is possible that the “hole” is a result of flow separation off the turbine’s conical exit fairing. The exit fairing is short and blunt at the end, and even at 100% throttle setting, the nozzle exit velocity is subsonic. In subsonic flow, these types of aft-facing geometries frequently lead to flow separation. The features of the flow profile shown in Figure 4.6 clearly correlate with the boundaries of the nozzle and the turbine exit fairing pictured in Figure 4.7.

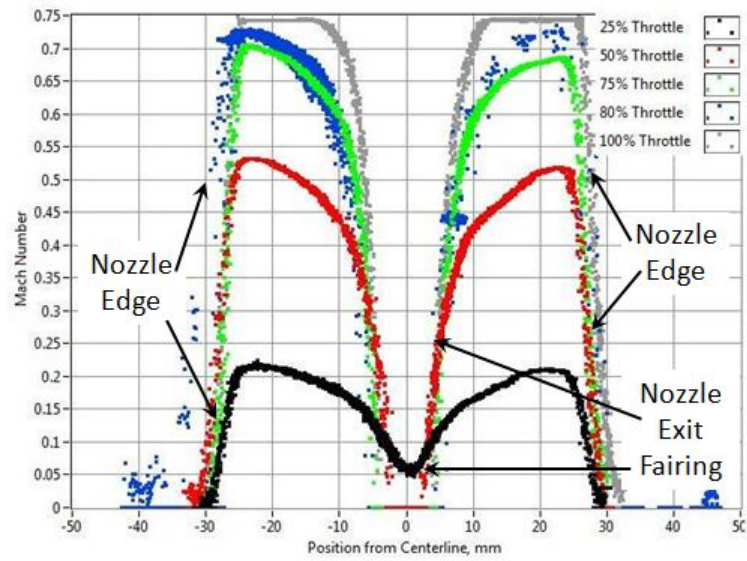


Fig. 4.6: Nozzle exit plane mach number distribution for various throttle settings.

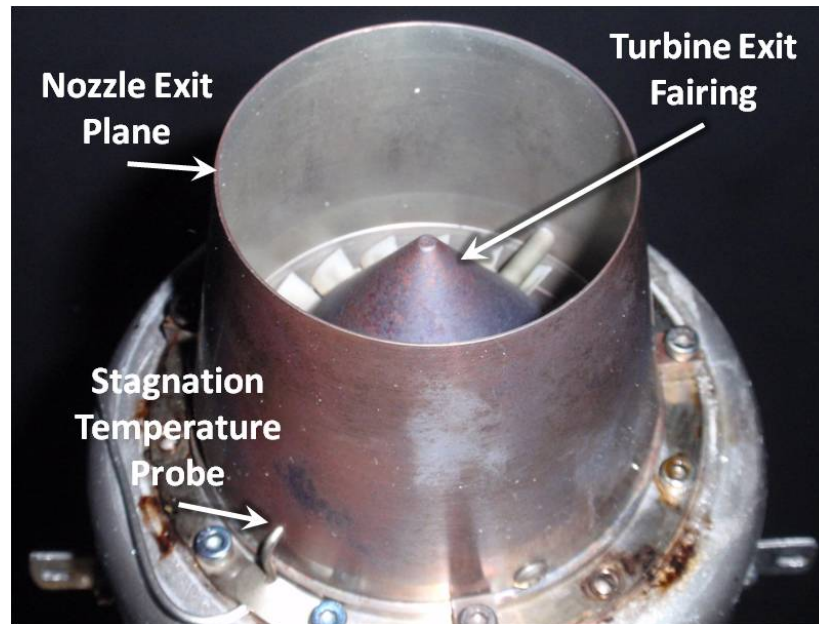


Fig. 4.7: JF-170 Rhino nozzle and turbine exit fairing.

4.3 Nozzle Exit Plane Measurements

Using equations developed specifically for high-speed flow [30], a relationship between the measured pressures and thrust levels can be established. The ratio of total pressure to static pressure is related to the Mach number and γ , the ratio of specific heats, through

$$M(r) = \sqrt{\frac{2}{\gamma - 1} \left(\left(\frac{p_o(r)}{p_{static}} \right)^{\frac{\gamma-1}{\gamma}} - 1 \right)} \quad (4.10)$$

where $M(r)$ and $p_o(r)$ denote the Mach number and total pressure at the position from the centerline, r . The exact value of γ depends upon the chemical makeup of the exhaust gases, which in this case is unknown. Knowing that jet engines run very lean (with an air-to-fuel ratio on the order of 50:1) the ratio of specific heats for air, $\gamma = 1.4$, was chosen as a close approximation. Since the JF-170 Rhino is a single-stage engine with a subsonic nozzle, the nozzle exit plane pressure, p_{static} , equals the the local ambient pressure.

Figure 4.8 shows the measured total pressure profile at a 75% throttle setting. Figure 4.6 plots the exit plane Mach number distribution, calculated using the 75% throttle pitot-static pressure measurements. The span of the high-velocity flow is approximately 22 mm wide on either side of the momentum hole. The hole is approximately 12 mm wide. These exhaust plume features significantly affected the thrust vectoring vane design.

The mean exit plane cross section Mach number is calculated as

$$\bar{M} = \frac{\int_{-R}^R M(r) 2\pi r dr}{2A_{exit}} = \frac{\int_{-R}^R M(r) r dr}{R^2} \quad (4.11)$$

At the 75% throttle setting, the mean exit plane mach number is approximately 0.598.

The local exit plane velocity is calculated as

$$V(r) = \sqrt{\gamma R_g T_o} \frac{M(r)}{\sqrt{1 + \frac{\gamma-1}{2} M(r)^2}} \quad (4.12)$$

where T_o is the stagnation temperature at the exit plane and R_g is the gas constant. T_o is measured by the nozzle exit plane temperature probe, and R_g is assumed to have its

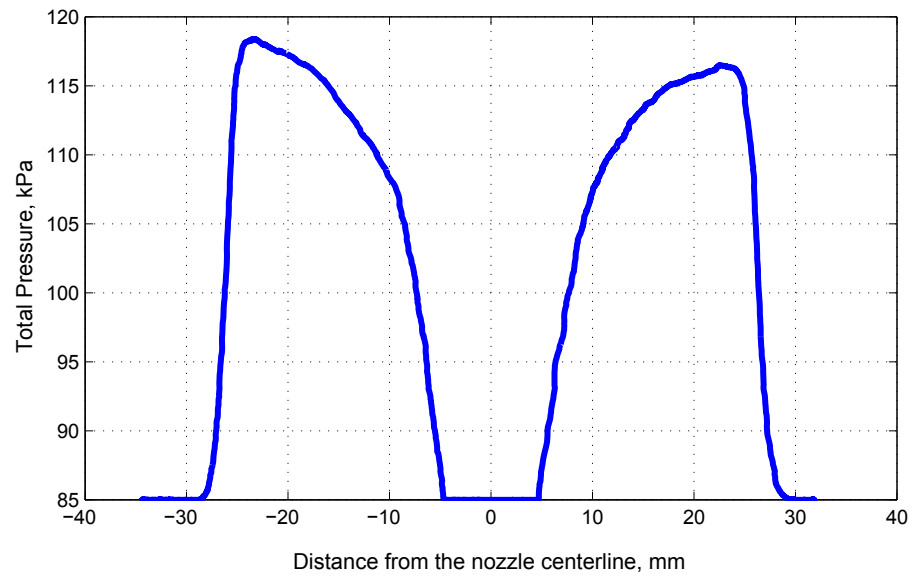


Fig. 4.8: Total pressure profile for the JF-170 nozzle exit plane at 75% throttle.

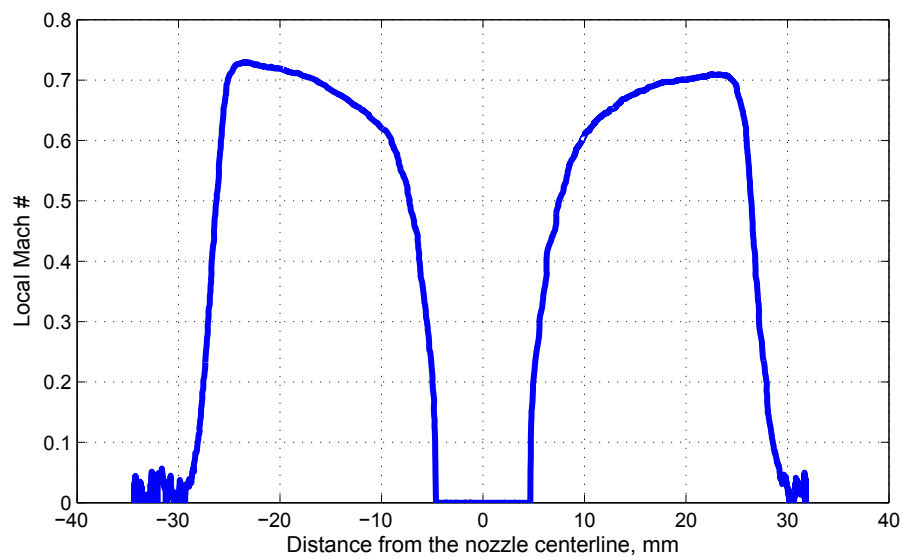


Fig. 4.9: Calculated local Mach number for the JF-170 nozzle exit plane at 75% throttle.

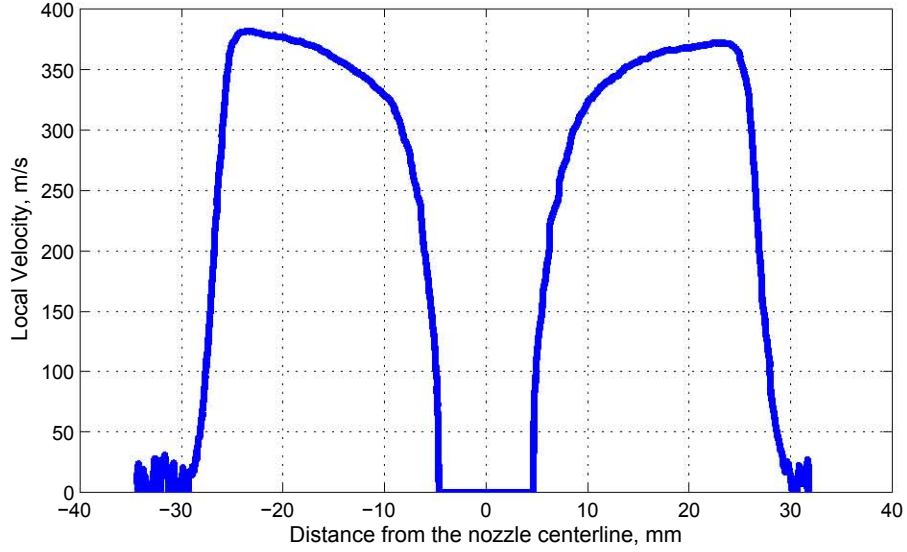


Fig. 4.10: Calculated local velocity for the JF-170 nozzle exit plane at 75% throttle.

standard value for air. Figure 4.10 shows the calculated local velocity at the 75% throttle setting. Following a procedure similar to the one used in Equation 4.11, the average velocity was calculated at $\bar{V} = 324.663 \text{ m/s}$ at the same 75% throttle setting.

The total mass flow through the nozzle is calculated from the integral of the local mass flow across the exit plane given by

$$\dot{m} = \frac{1}{2} \left(\int_{-R}^R \frac{\sqrt{\gamma} M(r)}{\left(1 + \frac{\gamma-1}{2} M(r)^2\right)^{\frac{\gamma+1}{2(\gamma-1)}}} \frac{p_o(r)}{\sqrt{R_g T_o}} 2\pi r dr \right) \quad (4.13)$$

Using Equation 4.13 the total massflow through the nozzle at 75% throttle was calculated to be $\dot{m} = 0.312 \text{ kg/sec}$.

The total thrust produced by the the system can be calculated using

$$T = \dot{m}_{exit} \bar{V}_{exit} - \dot{m} \bar{V}_{inlet} + (p_{exit} - p_{amb}) A_{exit} \quad (4.14)$$

the one dimensional thrust equation. Using Equation 4.14, the thrust produced by the engine at 75% throttle is calculated as 22.7 lbf . This result is within 1% of the thrust

Table 4.6: Sensitivity of Thrust Calculations to γ

γ	\bar{M}	\bar{V} (m/s)	\dot{m} (kg/s)	T (lbf)	Thrust measured by load cells (lbf)	% Error
1.400	0.598	324.663	0.312	22.745	22.600	0.64%
1.300	0.619	325.891	0.308	22.568	22.600	0.14%
1.236	0.633	326.792	0.305	22.441	22.600	0.70%

measured by the loads cells ($22.600lbf$) at the same throttle setting.

4.3.1 Sensitivity of the Measurements to the Ratio of Specific Heats, γ

The calculations of the previous section assumed gas properties for air at standard temperature, where $\gamma = 1.4$ and $R_g = 287.056 J/kg-K$. This section investigates the effects of real gas chemistry accounting for the effects of the fuel combustion within the engine. For this analysis, the equilibrium gas-chemistry code Chemical Equilibrium with Applications (CEA) [31] was used to model the combustion products.

The CEA code was developed at NASA's Glenn Research Center, and has been successfully applied for the analysis of rocket combustion, detonation, and flow across non-adiabatic shock waves. The code posits chemical reactions across the shockwave and then minimizes the Gibbs free energy in order to reach thermodynamic and transport properties at chemical equilibrium. The CEA code has extensive internal libraries for gas thermodynamic and transport properties including standard and non-standard temperature and pressure conditions.

The propellants used in the CEA analysis were turbine oil, kerosene and air. Since the exact makeup of the turbine oil is unknown, as is the precise fuel to air mixture ratio for the engine, several cases were analyzed with CEA. The values calculated for γ by CEA lie within the range of 1.236 to 1.238. Using these numbers, the calculations detailed in the previous section were repeated and the results are given in Table 4.6. The data verify that the thrust calculations are rather insensitive to changes in γ . The choice for $\gamma = 1.4$ was an accurate approximation.

Table 4.7: Flow Properties Used in the CFD Analysis

Mass Flow	Temperature	γ
0.308 kg/sec	580°C	1.3

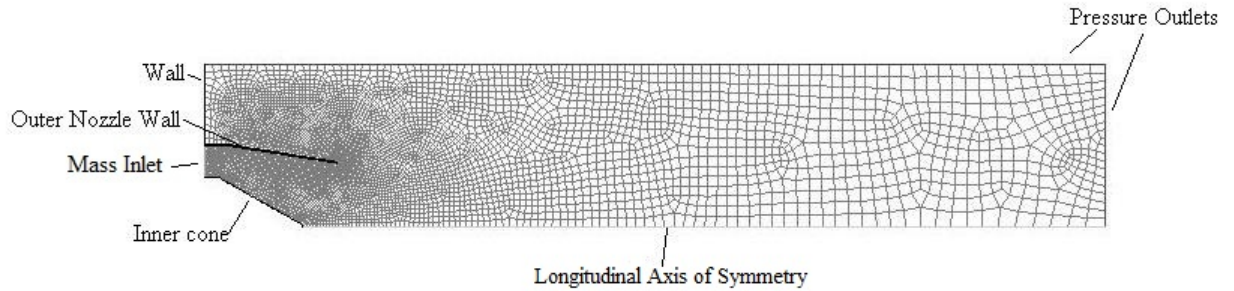


Fig. 4.11: Course CFD grid with boundary conditions used in this project.

4.4 Nozzle Computational Fluid Dynamics Study

Since thrust vectoring airfoils are being placed in the very non-uniform exhaust flow described in (4.2.2) and (4.3), the dynamics and properties of the exit plane flow must be better understood. To this end, an axisymmetric CFD model was created in the modeling software ANSYS® FLUENT®, to see if a flow pattern similar to that shown in Figures 4.8 and 4.9 could be reproduced numerically.

4.4.1 Numerical Method

Figure 4.11 shows one of the CFD grids created for this project. The nozzle has a converging outer wall and a short inner cone. These features are pictured in Figure 4.7. The mesh shown in Figure 4.11 is a relatively course grid using 7064 nodes. A finer grid was constructed using 28899 nodes. The finer grid uses node spacing that is approximately half of the node spacing in the course grid. Inputs for this CFD project include the exhaust mass flow rate, exhaust gas temperature and the ratio of specific heats. The CFD simulation was constructed to approximate the engine performance at 75% throttle with flow properties given in 4.7.

A solution was calculated on both the course and fine grids using both the first-order Upwind method as well as the second-order quadratic upstream interpolation for convective

kinetics (QUICK) method. The Upwind method uses data from the nearest upstream node to compute values for downstream nodes. The QUICK method uses quadratic interpolation with data from two upstream nodes and one downstream node to calculate new values for each node. The QUICK method generally provides a more accurate solution, but at the cost of stability and computation time [32].

Additional features used in FLUENT[®] include the ideal-gas solver and a k - ϵ turbulence model with standard wall functions. Various ratios of axial, radial and tangential velocities were tested by trial and error. The velocity profile which produced results that most closely matched the engine data had an axial component of $V_a = 0.987$, a radial component of $V_r = 0.15$ and a tangential component of $V_t = 0.05$.

4.4.2 CFD Results

Convergence was achieved on both the course and fine grid using both first and second order methods with the residual values being approximately 10^{-6} for all cases. The analytical solutions closely match each other, but only roughly approximate the measured data. Figures 4.12 and 4.13 show the pressure and Mach number distributions calculated on the fine grid using both the first-order Upwind method and the second-order QUICK method. These results are plotted along with the measured values.

The CFD solutions show a nearly linear drop off in stagnation pressure and mach number from the outer edge of the plume to the nozzle core. The measure profiles are more rounded. This difference is likely due to the rotational flow produced by the engine turbine. This rotating flow field smears the exit flow and was not accurately modeled in the CFD solutions.

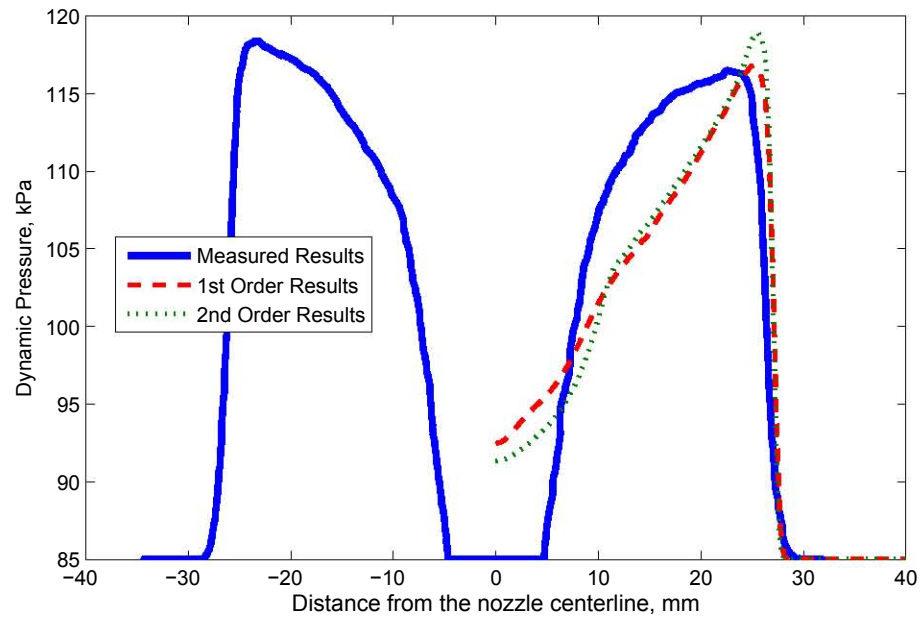


Fig. 4.12: Dynamic pressure distribution calculated on the fine grid using both the First Order Upwind and Quick methods.

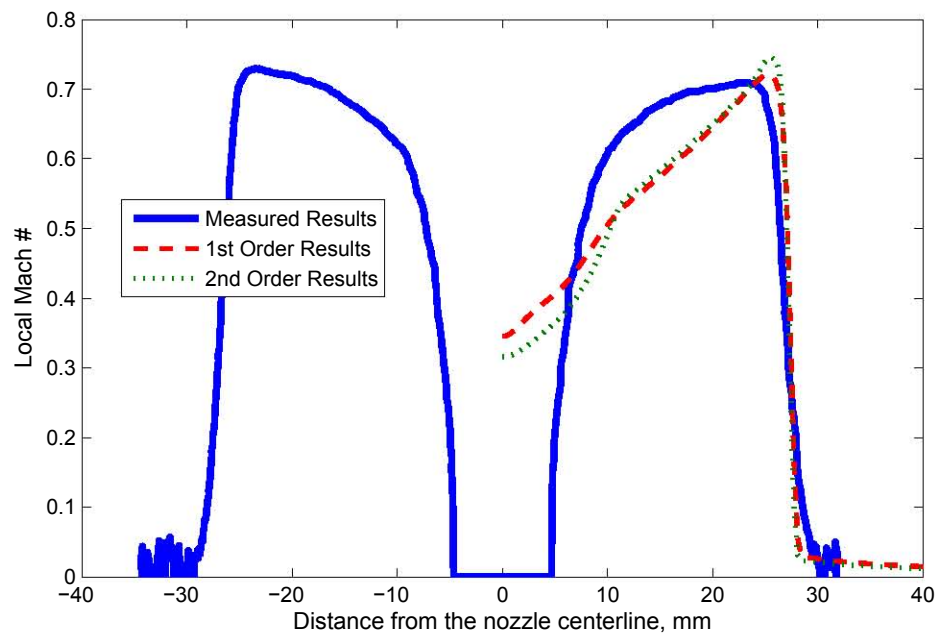


Fig. 4.13: Mach number distribution calculated on the fine grid using both the First Order Upwind and Quick methods.

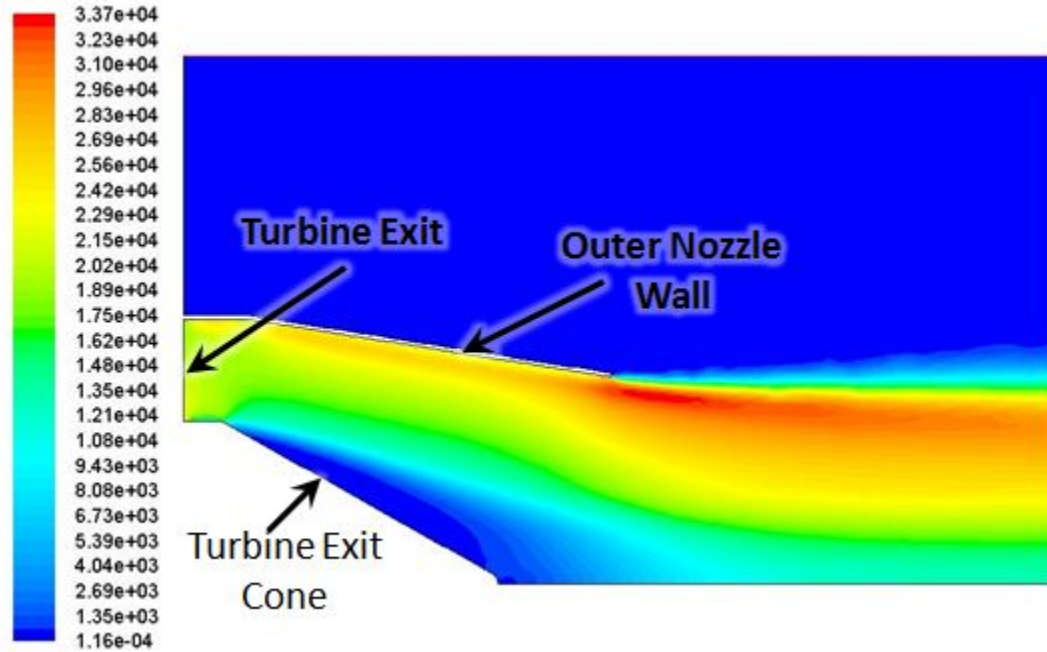


Fig. 4.14: Dynamic pressure contours in and downstream of the jet engine nozzle as calculated on the fine grid using the QUICK method.

The finer mesh better approximated the low pressure region, but the difference between the two solutions is negligible when compared to the differences between the calculated and measured profiles. Figures 4.14 and 4.15 show contours of dynamic pressure and Mach number in and just outside the nozzle. The low pressure region around the center cone is clearly visible.

Both static test measurements and CFD calculations confirm that the short length of the nozzle's center cone creates undesirable flow conditions. The cone converges too quickly and the flow is unable to "turn the corner." The flow is separating and creates a low pressure region behind the cone that affects the jet engine's performance. More thrust could be extracted from a properly designed nozzle. While the results from FLUENT[®] do not exactly match the empirical data, they do confirm the existence of the low pressure region and give a visual indication of the conditions creating the unusual exit plane profiles depicted in Figures 4.12 and 4.13.

Cases analyzed using only axial flow with zero tangential and radial velocity failed

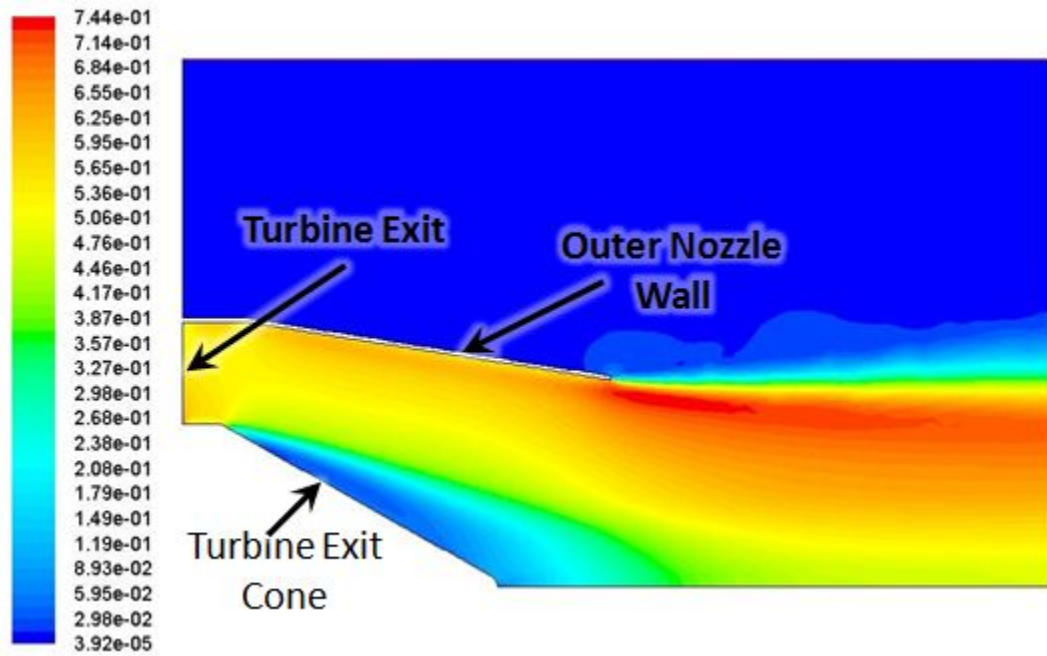


Fig. 4.15: Mach number contours in and just outside the jet engine nozzle as calculated on the fine grid using the QUICK method.

to completely model the rotating flow field and exhibited considerable differences with the measured exhaust plane data. This exit plane swirl has implications on the thrust vectoring system and could cause an asymmetry in the lift and moment forces produced by a set of airfoils. This asymmetry could cause instabilities that the orientation controller for the TVC system may not be able to overcome.

Chapter 5

Aerodynamic Thrust Vectoring System

5.1 Analysis of Alternative TVC Methods

The small scale of and low thrust available from commercial RC jet engines greatly limited the techniques available for the TVC system. The final system must be lightweight, have fast response times and have repeatable results. Gimbale and segmented nozzles both have large weight penalties and require many actuators for precise control. Such a system would be difficult to build on the small scale of the ESLRV.

A secondary fluidic injection TVC system requires modifying the engine nozzle to create a cavity for flow manipulation as well as injection ports. The lack of a readily available source of engine bleed air necessitates the use of a storage tank which would have a large weight penalty and would occupy valuable real estate. The amount of plumbing necessary for this system also presents design difficulties and weight penalties.

Post-nozzle exit exhaust flow manipulation leaves the original engine design intact, and has the smallest weight penalty. Thrust losses associated with supersonic flow turning will not be an issue since the JF-170 engine is equipped with a subsonic nozzle. Data verifying the subsonic nozzle exit plane condition was presented in (4.2.2).

Following an extensive trade study, a vectoring method using airfoils mounted directly in the exhaust flow was selected for the TVC system. This vectoring method reduces the magnitude of the available thrust, but care was taken to insure that sufficient thrust would be available to meet mission objectives. Because the jet engine's exhaust temperatures, approximately 600 °C at full throttle, are substantially lower than the melting temperature of readily available materials, this design requires no active cooling or special high-temperature materials.

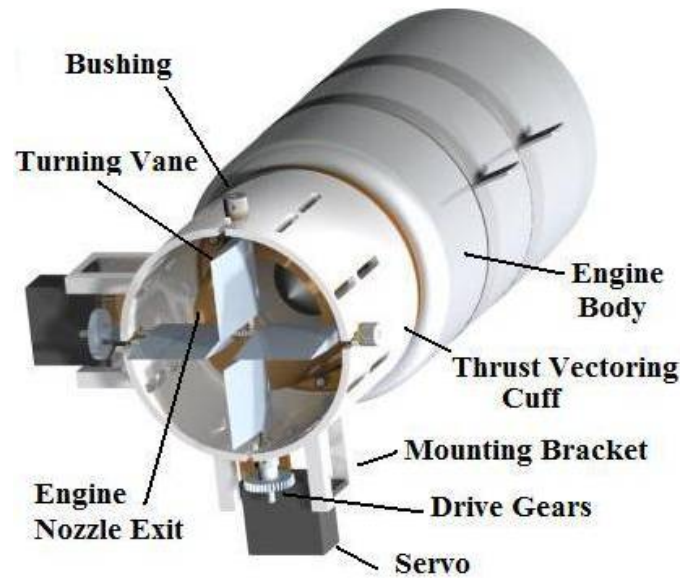


Fig. 5.1: Mechanical configuration of the TVC components.

5.2 Top Level View

Figure 5.1 shows a detailed view of the thrust vectoring system. Two sets of airfoils are used for pitch and roll plume deflections. Each set of airfoils is welded in place on an $1/8$ " stainless steel rod mounted over the nozzle of the jet engine and aligned with either the roll or pitch axis. The gap between airfoils allows both sets to be displaced to a maximum extent without causing interference. The airfoils are machined from stainless steel to withstand the high temperature of the jet engine exhaust.

Hobby-class RC servos were chosen to drive the thrust vectoring system because of their proven track record, low cost, and availability in a wide range of sizes. For the ESLRV design, two HITEC HS-5245MG digital programmable servos [33], featuring a PWM drive signal, were selected for use. The duty cycle of the PWM signal determines the extent of servo deflection. The HITEC servos use a finite number of steps of resolution for any given range of travel. The extent of travel was decreased from the nominal $\pm 60^\circ$ to $\pm 10^\circ$ to increase the available mechanism drive fidelity. Tests showed with the reprogrammed servo range, the servos could resolve angles down to at least $1/4^\circ$. This level of resolution is more than sufficient for the needs of this project. The deflection limits also prevent interference between the pitch and roll vanes.

5.3 Airfoil Design

Several airfoil configurations were selected for analysis, including several NACA four-digit series airfoils and airfoils with cylindrical and elliptical leading edges with tapered trailing edges. Design parameters include physical dimensions, section lift, section drag, and section pitching moment. Due to the high-speed of the engine's exhaust, the analysis also accounts for compressibility effects.

5.3.1 Airfoil Analysis

The thrust vectoring airfoil sections were sized using the two dimensional airfoil section compressible-flow CFD code, XFOIL, developed at the Massachusetts Institute of Technology [34]. Viscous calculations derived from XFOIL were demonstrated to be inaccurate. This inaccuracy was likely due to the viscosity model incorporated into the program. This model did not account for the high exhaust temperatures in the nozzle exit plane flow. Instead XFOIL was run in inviscid flow mode and viscosity adjustments were calculated using a USU-developed compressible skin friction code. Because XFOIL is a two dimensional analysis code, outputting sectional aerodynamic coefficients, the effects of finite wingspan were approximated using linear airfoil theory. Drag on a thin airfoil at the speeds produced by the jet engine is caused by three separate mechanisms: 1) Pressure profile drag, 2) Induced drag, and 3) Viscous surface drag. Viscous surface drag is often referred to as "skin friction."

Pressure profile drag is created by a difference in pressure between the leading and trailing edge of the airfoil [35]. High pressure builds in front of the airfoil while lower pressures exist towards the trailing edge, often as a result of flow separation. This differential pressure pushes back on the airfoil, creating a drag force. Figure 5.2 illustrates flow separation and the effect that streamlining has on reducing the magnitude of profile pressure drag. XFOIL predicts the pressure at any point around an airfoil and can accurately calculate the pressure profile drag.

Induced drag is produced by finite span airfoils and is a result of vortex-induced downwash at the airfoil wing tips. This induced downwash creates an induced flow component parallel to the freestream flow acting in the negative axial direction [36]. The induced drag

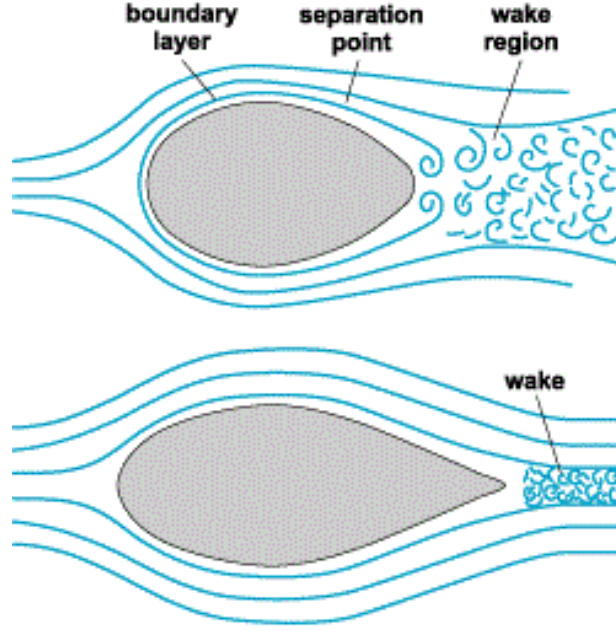


Fig. 5.2: Profile of pressure drag caused by boundary layer separation.

is easily calculated using Equation 5.1 which comes from linear thin airfoil theory [36]. In Equation 5.1, C_L is the lift coefficient predicted by XFOIL, R_A is the aspect ratio, e_s is the Oswald span efficiency factor and C_{Di} is the computed induced drag coefficient.

$$C_{Di} = \frac{C_L^2}{\pi R_A e_s} \quad (5.1)$$

A span efficiency factor of $e_s = 0.9$ was used. As the aspect ratio of the wing decreases from larger numbers (aspect ratios for common airplane wings typically range from 6 to 16) and approaches one, the span efficiency factor approaches one. The aspect ratios for the airfoils analyzed for this project were in the range of 0.5 to 1.1.

Skin friction drag is a result of viscous interactions between the high-speed gases and the airfoil's surface. Essentially, the friction between the fluid and the airfoil surface imparts a force, or transfer of momentum, from the fluid to the airfoil. The component of this wall shear force in the direction of fluid flow is the friction drag [35]. The vortex panel method used by XFOIL does not account for viscous effects and is not capable of calculating the skin friction drag.

The skin friction drag was calculated using traditional flat plate skin friction models adjusted for compressibility and hot gas flow using the methods of Sommer and Short [37]. The specific model used depends on the type of boundary layer present on the airfoil.

The Reynolds number of the flow under consideration, given by Equation 5.2, is used as a guideline for determining which type of boundary layer is present. Common practice states that a laminar boundary layer is present when the Reynolds number is below 500,000 and that a turbulent boundary layer clearly exists for Reynolds numbers greater than 10,000,000. A transition boundary layer is assigned to the values in between [35].

The Reynolds number is calculated using Equation 5.2, where ρ is the density of the fluid, V is the velocity of the fluid, L is the characteristic length or distance traveled by the fluid, μ is the dynamic viscosity of the fluid [38]. Reynolds numbers for the airfoils analyzed were below 200,000, indicating the presence of a laminar boundary layer.

$$Re = \frac{\rho V L}{\mu} \quad (5.2)$$

The derivation of compressibly corrected friction drag begins with Equation 5.3, the equation for the friction drag coefficient in incompressible flow situations [35]. This coefficient is represented by the notation C_{Dfi} .

$$C_{Dfi} = 1.328 \frac{1}{\sqrt{Re}} \quad (5.3)$$

Again, because the jet engine's exhaust flow is greater than the incompressible approximation limit of $M < 0.3$, Equation 5.3 must be adjusted to account for compressibility effects.

The method developed by Sommer and Short compensates for compressibility effects by evaluating the Reynolds number based upon their empirically derived reference temperature calculation. This calculation is shown in Equation 5.4, where M_∞ is the freestream Mach number, T_∞ is the freestream temperature and T_{wall} is the surface temperature of the airfoils. This reference temperature is used in the calculation of the density and dynamic

viscosity which in turn affect the final value of the Reynolds number.

$$T_{ref} = \left(1 + 0.035M_\infty^2\right) T_\infty + 0.045 (T_{wall} - T_\infty) \quad (5.4)$$

A second temperature adjusting equation, based on the same principle as Sommer and Short's reference temperature calculation, is shown in Equation 5.5. Instead of using a wall temperature, which would need to be measured, this equation evaluates a reference temperature based upon average conditions within the boundary layer. In Equation 5.5, γ is the ratio of specific heats, and R_f is a correction factor that accounts for the adiabaticity (or non-adiabaticity) of the system. Equation 5.5 was used for the skin friction drag calculations performed in this analysis as it eliminated the need for a direct airfoil surface temperature measurement. Additionally, the thermodynamic and transport properties of the jet engine exhaust gases were assumed to be identical to those of high temperature air.

$$T_{avg} \approx T_\infty \left[1 + \left(R_f - \frac{8}{15} \right) \left(\frac{\gamma - 1}{2} M_\infty^2 \right) \right] \quad (5.5)$$

Values for R_f can vary over a wide range. $R_f = 1$ is used for adiabatic flow, and $R_f = 0$ provides solutions for isothermal flow. In the case of the airfoils being analyzed, their total heat capacity is small compared to the energy of the flow. Therefore, it is assumed that the flow under consideration is very close to adiabatic and a value of $R_f = 1$ was used in the skin friction drag calculations.

Using the average temperature calculated from Equation 5.5, the temperature-adjusted density can be calculated using Equation 5.6. This equation assumes that pressure is constant.

$$\rho(T_{avg}) = \rho_\infty \left(\frac{T_\infty}{T_{avg}} \right) \quad (5.6)$$

The temperature-adjusted dynamic viscosity is given in Equation 5.7. In this equation, μ_∞ is the freestream viscosity and C_S is Sutherland's constant. Equation 5.7 is also known as Sutherland's formula [39]. Table 5.1 contains Sutherland's constant for various gases

Table 5.1: Sutherland's Parameters for Viscosity Calculation

Gas	C_S (K)	T_∞ (K)	μ_∞ ($N\cdot s/m^2$)
Air	66.667	291.15	1.827×10^{-5}
Nitrogen	61.667	300.55	1.781×10^{-5}
Oxygen	70.556	292.25	2.018×10^{-5}
Carbon Dioxide	133.333	293.15	1.480×10^{-5}

along with their reference temperatures and viscosities.

$$\mu(T_{avg}) = \mu_\infty \left(\frac{T_{avg}}{T_\infty} \right)^{\frac{3}{2}} \left(\frac{0.555T_\infty + C_S}{0.555T_{avg} + C_S} \right) \quad (5.7)$$

Equation 5.8 is obtained by substituting Equations 5.5 through 5.7 into Equation 5.3. This new equation provides a convenient method for estimating the values of skin friction drag for compressible flows of a laminar nature.

$$C_{Dfc} = \frac{C_{Dfi}}{\left[\left(\frac{T_\infty}{T_{avg}} \right)^{\frac{5}{2}} \left(\frac{T_{avg} + C_s}{T_\infty + C_s} \right) \right]^{\frac{1}{2}}} \quad (5.8)$$

Equations 5.1 through 5.8 were coded together in LabVIEW to run calculations on the airfoils mentioned in (5.3). Data files generated by XFOIL for multiple Mach numbers and multiple angles of attack were read by this LabVIEW code. The code then computed the induced drag, compressibly corrected friction drag and the total moment created about the engine's gimbal point. This data was saved for later reference as well as plotted for visual inspection.

5.3.2 Airfoil Analysis Results

Representative data sets from XFOIL are plotted in Figures 5.3 and 5.4 showing two airfoil sections being analyzed and the local pressure coefficient with respect to the airfoil surfaces. The airfoil in Figure 5.3 starts with a circular leading edge which directly extends into a flat section before tapering to a sharp trailing edge. The transition from flat to taper for the airfoil pictured occurs at the 60% chord position. Various airfoils of this

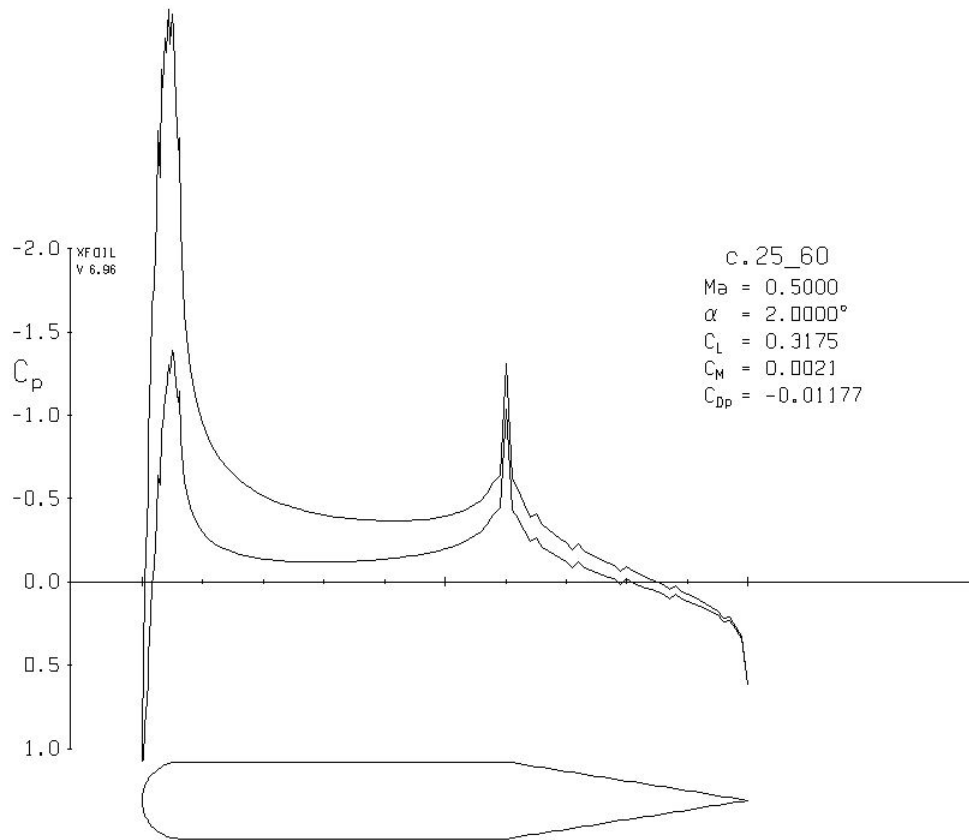


Fig. 5.3: Custom airfoil design and the associated pressure distribution calculated by XFOIL.

geometry were analyzed with each having a different thickness ratio and different taper transition point. The airfoil in Figure 5.3 has a 12.7% thickness ratio. Notice in the pressure distribution that there are two alarming spikes in pressure. One occurs at the blunt leading edge and the other occurs at the transition to taper point. These spikes indicate areas where the boundary layer is likely to separate at even moderate angles of attack. Each of the airfoils analyzed with variations of this geometry exhibited similar pressure spikes.

The airfoil in Figure 5.4 again begins with a circular leading edge, but instead of having a flat region, it proceeds directly into a taper of 6.7° , terminating at a sharp trailing edge. The maximum thickness for this airfoil is 21%. This airfoil has a smoother pressure graph than the airfoil in Figure 5.3, but it still has a sharp spike in pressure at the leading edge. This again, is indicative of flow separation.

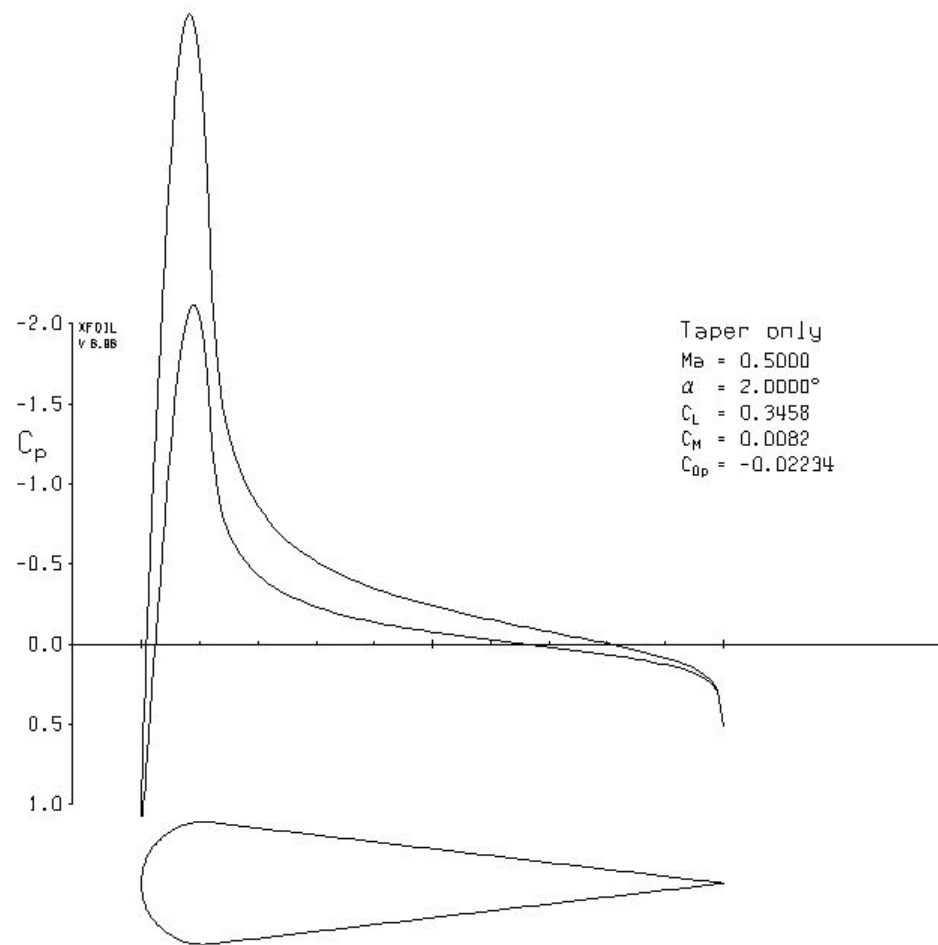


Fig. 5.4: Tapered wedge airfoil design and the associated pressure distribution calculated by XFOIL.

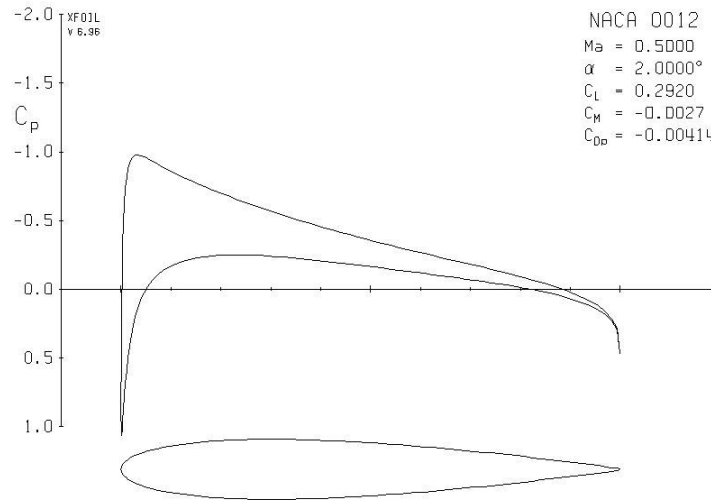


Fig. 5.5: Local pressure coefficient vs. chord length for a NACA 0012 airfoil at $M = 0.5$ and $\alpha = 2.0^\circ$ as calculated in XFOIL.

The two airfoils pictured in Figures 5.3 and 5.4 were designed and analyzed when it was thought that the flow out of the jet engine was at or slightly above Mach 1.0. Airfoils with blunt leading edges and sharp transition points are typically used in supersonic flow. Shock waves develop at these transition points which help to bend the flow around the corner. This is not true of subsonic flow, and these features are likely to induce premature boundary layer separation. This would have the adverse effect of both decreasing lift and increasing drag.

Figure 5.5 shows the pressure plot produced by XFOIL for a NACA 0012 airfoil at an angle of attack (AoA) of 2° with $M = 0.5$. Table 5.2 shows the data for the same NACA 0012 airfoil produced by XFOIL and the USU-developed compressible skin friction code at $M = 0.5$ and for various AoAs. Data values are a sum of the results obtained for two individual airfoils having a chord length of 43 mm and a span of 22 mm.

In Table 5.2, L is the lift force in Newtons, D_T is the total drag from all three sources in Newtons, M_G is the moment about the gimbal point, $M_{c/4}$ is the moment about the quarter chord of the airfoil and the remaining three symbols represent the section coefficients for their respective subscript variables. Section coefficients represent dimensionless aerodynamic forces per unit span. They are non-dimensionalized by the dynamic pressure

Table 5.2: Aerodynamic Properties for a NACA 0012 Airfoil at $M = 0.5$ and Various Angles of Attack

α	$L (N)$	$D_T (N)$	$M_G (Nm)$	$M_{c/4} (Nm)$	\tilde{C}_L	\tilde{C}_{D_T}	\tilde{C}_{M_G}
-2.00	-4.2937	1.0232	0.9925	0.0481	-0.2708	0.0645	1.4557
-1.00	-2.1437	0.3664	0.4955	0.0240	-0.1352	0.0231	0.7268
0.00	-0.0016	0.1483	0.0004	0.0000	-0.0001	0.0094	0.0005
1.00	2.1421	0.3661	-0.4951	-0.0240	0.1351	0.0231	-0.7262
2.00	4.2921	1.0226	-0.9921	-0.0480	0.2707	0.0645	-1.4551

and the planform area (the airfoil's chord length multiplied by its wingspan). The moment naturally produced by the airfoils is traditionally given at the quarter chord, $M_{c/4}$ where the moment changes negligibly with angle of attack [36]. The moment about the gimbal point, M_G , includes the effects of the lift created by the airfoils.

The effects of friction drag can be seen in the total drag at $\alpha = 0^\circ$. At zero angle of attack, drag is produced by skin friction drag and pressure profile drag. Similar data sets were calculated at a variety of Mach numbers. These calculations were repeated for several different airfoils.

Figures 5.6 and 5.7 show the total drag calculated as well as the lift to drag (L/D) ratio for the NACA 0012 airfoil. In Figure 5.7, it becomes clear that the total drag force grows parabolically at angles of attack beyond $\pm 1^\circ$. Thus, the thrust vectoring system will need to maintain orientation using commanded angles less than $\pm 1^\circ$ to reduce total thrust losses due to vane drag.

5.3.3 Vane Mechanism Design

Effects of total lift, flow separation at high angles-of-attack, induced drag, and wing thicknesses at the quarter chord (for structural integrity) were considered in the design analysis. The simple blunted leading edge configurations offered the greatest ease of manufacturing, but tended to separate on the leeward side at moderate angles of attack. This flow separation resulted in a significant increase in the overall profile drag of the section.

A major design consideration was mechanical interface. As described in Section 5.2,

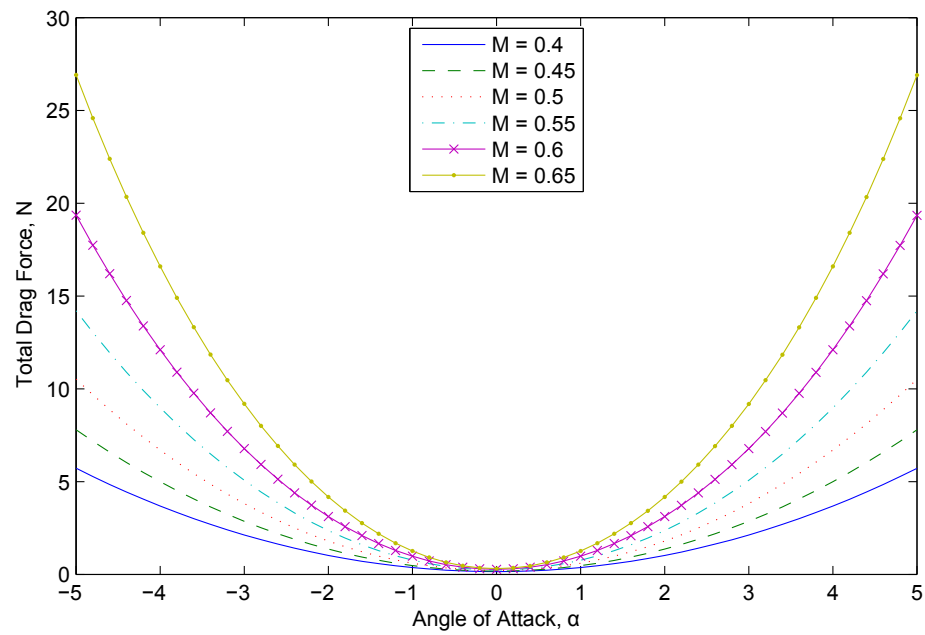


Fig. 5.6: Total drag force created by a NACA 0012 airfoil pair.

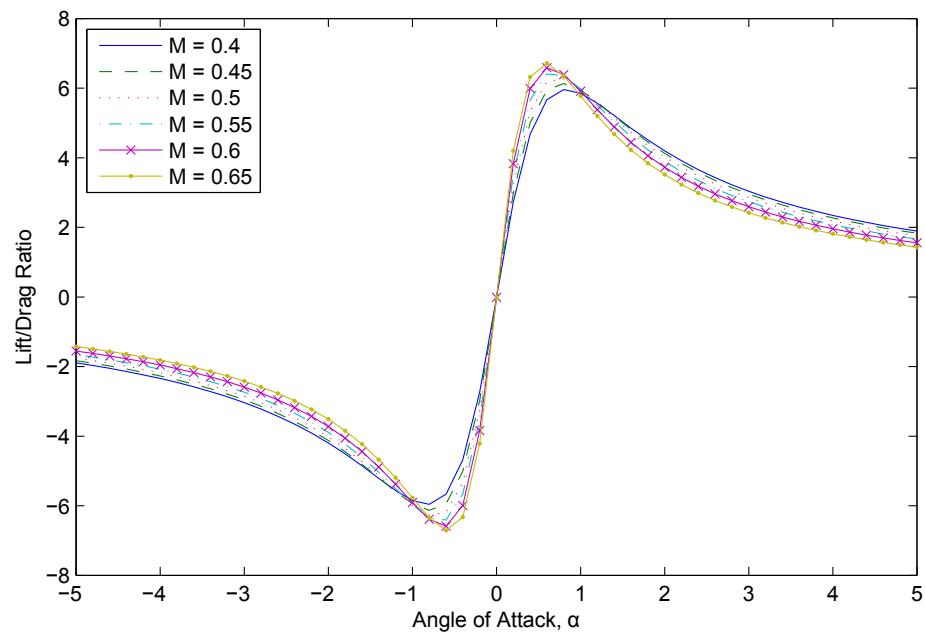


Fig. 5.7: Lift to Drag ratio for a NACA 0012 airfoil pair.

digital servos were chosen early on in the design phase. They were selected because of their proven track record, ease of use and high degree of resolution. After servo selection, the next step in the mechanical design was coming up with a method for interfacing the servos with the airfoils. A commercially available set of rods and gears were found that are specifically manufactured for use with servos.

A geared design was chosen for two reasons. First, the sprocket on the output shaft of the servos is small and it would be difficult to mount an interface rod directly to it. The shaft does, however, have splines machined into it for ease of interface with various commercially available servo arms. Servo City manufactures a variety of metal and plastic gears which are machined with a matching spline on their internal shafts. The second reason a geared design was chosen is because it provides more thermal distance between the hot exhaust gases and the sensitive and partially plastic servos. The gears limit the amount of direct contact between the servos and any heat that would be conducted through the interface shaft.

The drawback to using the gears manufactured by Servo City is the size of the mounting shaft for the interface gear. The smallest shaft available has a 3.175 mm ($1/8$ in.) diameter. This size limitation has a direct effect on the thickness of the airfoils. The airfoils were to be welded directly to the interface shaft in order to provide a solid connection between the servos and the airfoils. In order to facilitate proper alignment and ease of manufacturing, a 3.175 mm ($1/8$ in.) hole would need to be drilled in the airfoil near the quarter chord.

The quarter chord location was chosen because as a general rule, the moment on an airfoil is smallest at this point. The airfoils would also need to be thicker than 3.175 mm ($1/8$ in.) to provide for structural integrity around this hole. Table 5.3 lists the various airfoils considered and their respective lengths required for a 5.08 mm (0.2 in. thickness at the quarter chord. The required length correlates inversely with the airfoil's thickness. It is not desirable to use an airfoil with a thickness above $\sim 12\%$ because the assumptions behind thin airfoil theory are no longer valid [36].

After all of the above factors were considered, it was determined that the NACA 0012

Table 5.3: Airfoil Length Required for a 5.08 mm (0.2 in.) Quarter Chord Thickness

Airfoil	Thickness Ratio	Chord Location of Max Thickness	Required Length (mm)
NACA 0004	4%	30%	127
NACA 0008	8%	30%	63.5
NACA 0012	12%	30%	42.333
Circular leading edge with 6.7° taper.	21%	10%	28.63
Circular leading edge with sharp taper beginning at 60% chord.	12.7%	6% - 60%	40

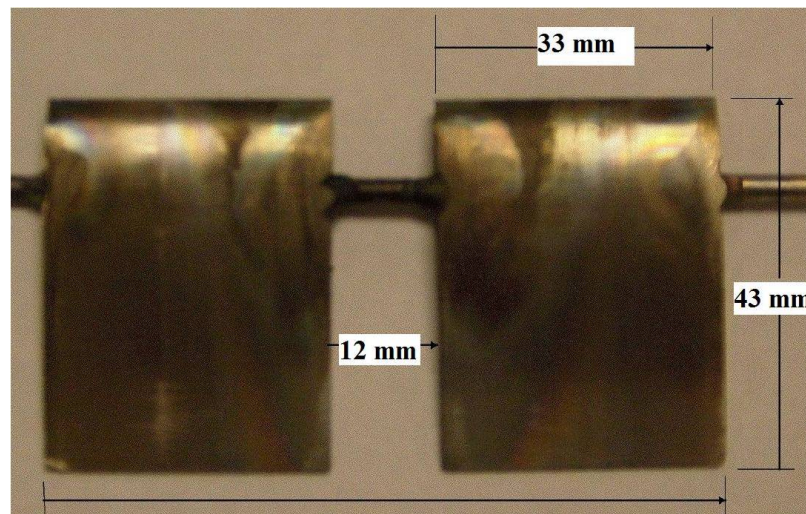


Fig. 5.8: NACA 0012 turning vane pair with annotated dimensions.

airfoil section offered the best overall performance: it was selected for the ESLRV design. It combines the ideal pressure distribution in a configuration that minimizes the chord length of the airfoil. Figure 5.8 shows the NACA 0012 turning vane pair design. One pair of vanes is used for the pitch axis, and another for the roll axis. The center gap between the turning vanes prevents the pitch and roll vanes from interfering as they pivot about their axes. The center gap, vane span, and chord are marked on the image. Each vane segment was machined from a single block of stainless steel, and the mounting rod was press-fit and welded at the quarter chord of the vane.

The vane dimensions were based on the flow characteristics of the engine plume. To

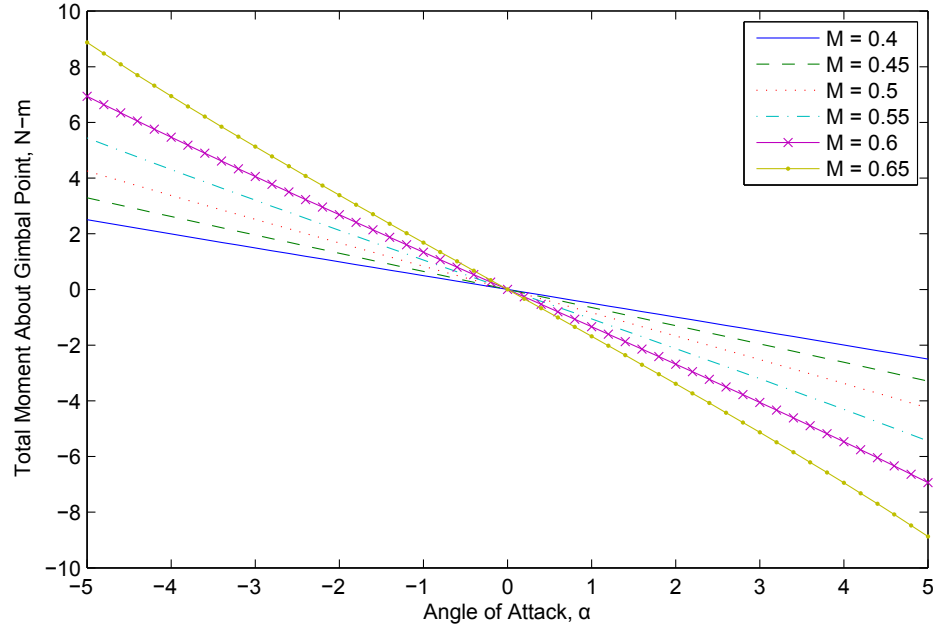


Fig. 5.9: Pitching moment about the engine's gimbal point generated by the NACA 0012 vane pair.

best take advantage of the flow distribution presented in (4.2.2) and to aid in fabrication, the pitch and roll axis turning vanes were divided into two sections each, with each section spanning approximately 33 mm with a 12 mm gap between sections. Due to the momentum hole in the center of the nozzle flow, the gap between airfoil sections eliminates pitch-vane and roll-vane interference, while having a minimal effect on the overall performance. The vanes are slightly oversized to extend beyond the edge of the exit jet-plume. This extension beyond the plume flow field helps to weaken the wingtip vortex and minimizes induced drag effects.

Figure 5.9 shows the calculated gimbal point pitching moment for the pair of NACA 0012 airfoils having a chord length of 43 mm and a combined span of 66 mm. Quarter-chord pitching moments have been translated to account for the vane offset from the hinge point of the inner gimbal ring. The moment is plotted as a function of angle of attack for Mach numbers varying from 0.40 to 0.65. A positive angle of attack on the vane results in a negative pitching moment about the gimbal point.

The data presented in Table 5.2 and Figures 5.7 and 5.9 does not account for the low aspect ratio of the airfoils. Though the airfoils have a physical span of 33 mm, the flow is constrained across approximately 22 mm. This gives the airfoils an effective aspect ratio of 0.5116. Equation 5.9 presents a method for calculating the effects of aspect ratio on the lift coefficient [40]. The required inputs include the section lift slope, $\tilde{C}_{L,\alpha}$, and the lift slope factor, κ_L . κ_L is given by Equation 5.10 where a_1 is the first coefficient of a Fourier series that represents the circulation distribution predicted by Prandtl's lifting-line theory. An indepth explanation of this Fourier series and the calculation of its coefficients is given in [40].

$$C_{L,\alpha} = \frac{\tilde{C}_{L,\alpha}}{\left[1 + \tilde{C}_{L,\alpha}/(\pi R_A)\right] (1 + \kappa_L)} \quad (5.9)$$

$$\kappa_L = \frac{1 - (1 + \pi R_A/\tilde{C}_{L,\alpha}) a_1}{(1 + \pi R_A/\tilde{C}_{L,\alpha}) a_1} \quad (5.10)$$

The section lift slope was derived from the section lift coefficients predicted by XFOIL for various Mach numbers. These values ranged from 7.83 at Mach 0.40 to 10.53 at Mach 0.65. For comparison, thin symmetric airfoils under more traditional flow conditions have a lift slope of 2π or 6.28. Using these values for section lift slope in Equations 5.9 and 5.10, the lift slopes for the finite airfoil at various Mach numbers were calculated. These new values ranged 1.31 from at Mach 0.40 to 1.37 at Mach 0.65. Using Equation 5.11 [40], the lift coefficient was calculated from which the total lift and effective gimbal point moment were calculated. The total moment about the gimbal point, adjusted for the effects of the low aspect ratio is plotted in Figure 5.10.

$$C_L = C_{L,\alpha} \alpha \quad (5.11)$$

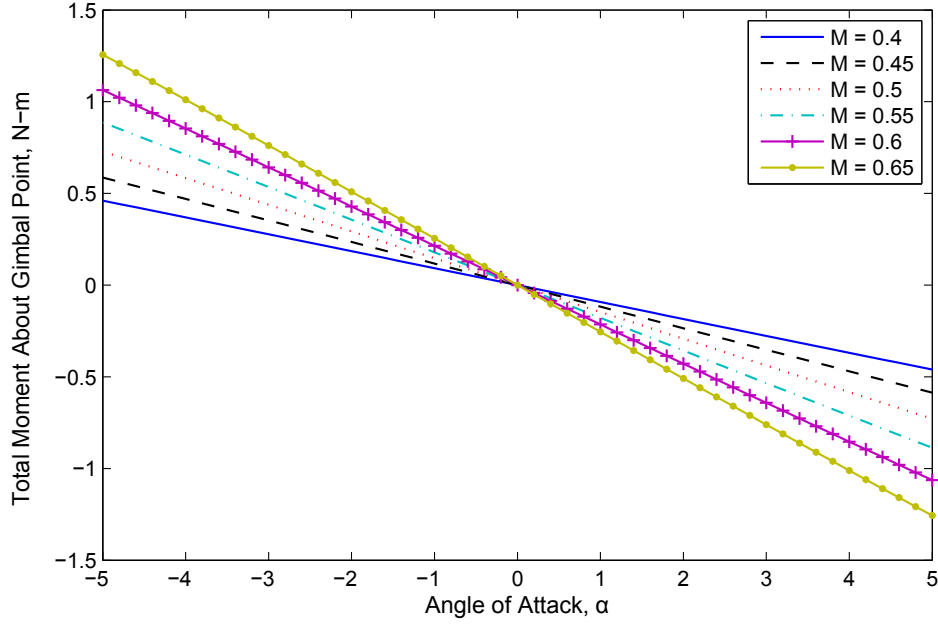


Fig. 5.10: Pitching moment about the engine's gimbal point adjusted for low aspect ratio effects.

5.4 Inner Platform Avionics

Onboard thrust vectoring control law calculations and data flow management were controlled using a GumStix[®] Overo[™] Fire micro-computer [41]. The GumStix[®] is a 17 mm x 58 mm x 4.2 mm, 720 MHz single-board computer which features the open-source Overo[™] development platform. The Fire platform also features an industry-standard IEEE 802.11g wireless connection as well as a Bluetooth connection. Figure 5.11 shows the Gumstix[®] flight computer.

The computer's design allows it to easily interface with one of several expansion boards. This project makes use of the Pinto-TH expansion board which features two two-wire serial ports, a USB mini-AB port and six PWM lines. The ESLRV design leveraged both the built-in wireless capability for down-link to the ground, and the PWM ports to control both the engine throttle and thrust vectoring vane servo commands.

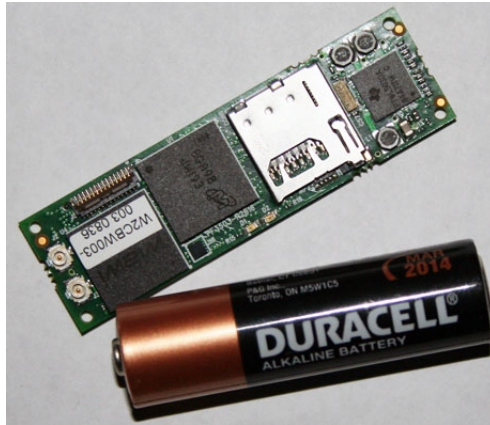


Fig. 5.11: Gumstix[®] Overo[™] Fire flight computer.

A wireless telemetry link was used to communicate between a ground-based laptop computer and the onboard Gumstix[®] flight computer. This laptop runs an interface program, written specifically for this project in the NI Labview 2009[®] programming language, which allows direct control of all engine functions including built-in test diagnostics, startup, and throttle settings. The program also allows the controller gains and reference angles to be modified in real-time and uplinked to the flight computer. Finally, this program receives and logs pertinent flight data including the engine FADEC parameters, inertial measurement unit (IMU) outputs, and controller moment and vane deflection commands. The Gumstix[®] interface replaces the RC transmitter and receiver control units typically used to control the JF-170 Rhino engine.

The IMU used on the vehicle, model number 3DM-GX3[®]-25, manufactured by Microstrain[®] [42], is shown in Figure 5.12. This IMU is a high-performance miniature attitude heading reference system that includes embedded tri-axial accelerometers, rate-gyros, magnetometers, and a temperature sensor. The form factor and weight are very small, making this an ideal device for use on such a small vehicle.

User-selectable output parameters for the IMU include Euler angles, rotation matrix components, velocity vector components, acceleration vector components, three-axis angular rates, and three-axis magnetic field components. Local magnetic field disturbances created by the rapidly spinning jet engine turbine on the inner platform, and ESCs and

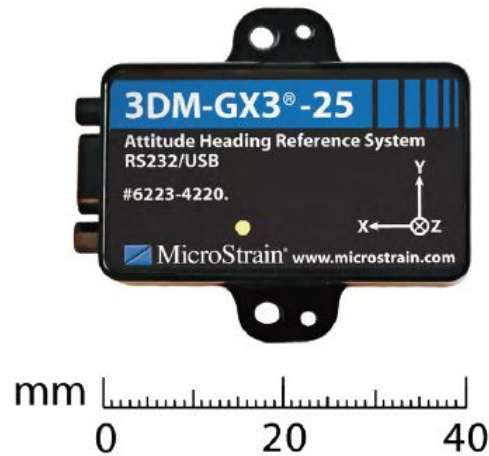


Fig. 5.12: The 3DM-GX3[®]-25 IMU used to sense angular orientation and rates.

maneuvering motors on the outer platform were a real concern. It was feared that these magnetic field disturbances would bias the magnetometer readings of the IMU, and in turn bias or corrupt the calculated attitude angles. A series of calibration tests were performed where the IMU Euler angles were logged for a wide range of engine throttle settings and maneuvering rotor speeds. Fortunately, there were no observable effects due to the rotating components.

Figure 5.13 shows the power distribution and signal routing of the thrust-vectoring avionics components on the inner gimbal platform. A two-cell 7.4-volt, 1.00 amp-hour Li-Po battery supplies power to a 5-volt output BEC. Power from the BEC is then distributed to the Gumstix[®] and associated logic level shifting circuits, two servos, the engine FADEC and the IMU with its associated logic level converter. The FADEC is powered by the BEC, but it also controls the distribution of power from a separate two-cell, 7.2-volt, 4.3 amp-hour Lithium-Ion (Li-Ion) battery to the jet engine fuel pump and other support equipment. A powered USB hub was originally used to facilitate communication between the FADEC, IMU and Gumstix[®]. The FADEC also required a serial to USB interface cable. The USB hub proved to be unreliable and was replaced with direct serial communications.

Logic level shifting circuits are required on the communication lines because each of the devices operates on a separate logic level. The IMU operates at standard RS-232 logic

levels of ± 15 volts. The FADEC and the servos expect a PWM signal that operates on transistor-transistor logic (TTL) levels of 0 to 5 volts. The FADEC also outputs data at this same logic level. The Gumstix[®] operates at a much lower 0 to 1.8-volt logic level.

5.5 Thrust Vectoring Control System

The pitch and roll orientations of the inner platform are controlled independently using either a PID control law [43] or a proportional, filtered control law. The reasons behind using either will be demonstrated in 6. On the ESLRV, the roll angle (ϕ), pitch angle (θ), roll rate (p), and pitch rate (q), as sensed by the on-board IMU, are used as feedback

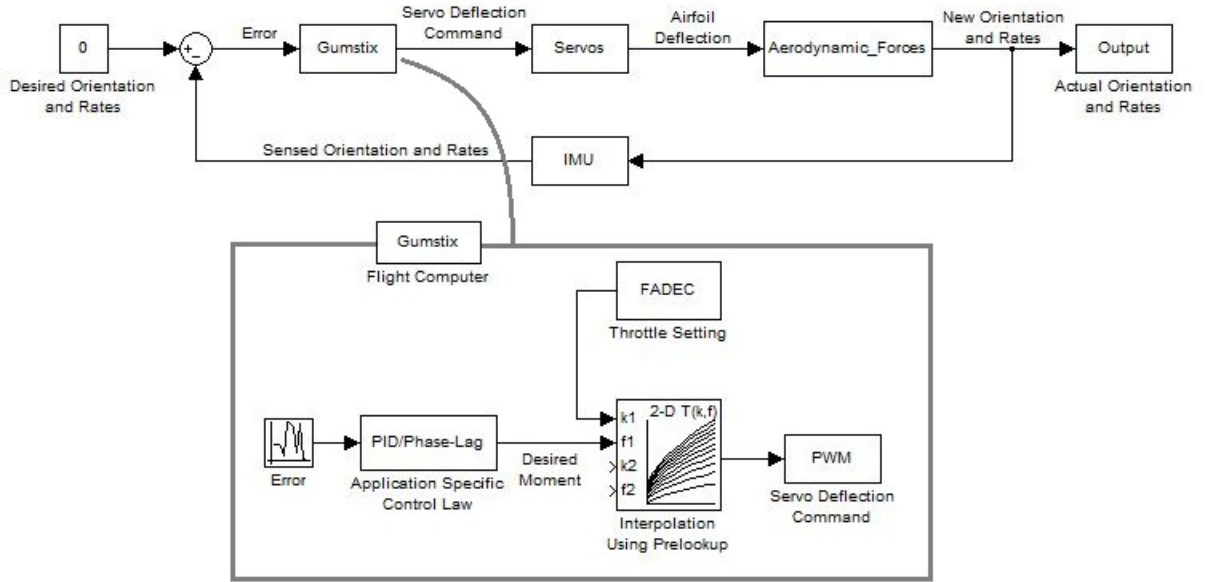


Fig. 5.14: A block diagram of the end-to-end control law for a single axis on the ESLRV.

parameters for the control laws.

The IMU sensor data is blended in an internal micro-processor running a sensor fusion algorithm to provide inertial navigation quality output parameters. Figure 5.14 presents the end-to-end control law for a single control-axis. An on-board micro-computer processes the current orientation state of the jet engine, as sensed by the IMU. Based upon the current orientation, the micro-computer uses a PID control law to compute a moment command that will restore the engine to a vertical state. Once the moment command is calculated by the control law, a table-lookup of the vane deflection moment data, presented in Figure 6.6a, is used to generate the pulse-width command for the servo mechanism. The onboard avionics necessary to perform the control calculations are described in (5.4). The pitch and roll control laws were identical, and were implemented independently.

5.5.1 PID Control Method

The PID control law generates a moment command to keep the inner gimbal pitch and roll angles very near pre-determined reference control angles – zero in the ideal case. A PID controller uses the sum of three representations of the error of the state: a proportional term,

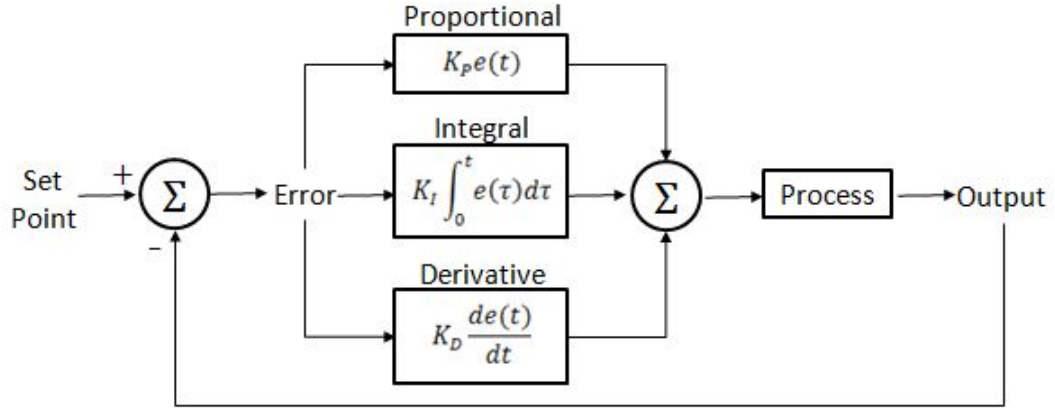


Fig. 5.15: A block diagram for a standard PID controller.

an integral term and a derivative term. The proportional term represents the instantaneous value of the error, the integral term provides a historical sum of the error up to the current time and the derivative term provides a linear extrapolation of the future value of the error. A block diagram showing the basic operation of a closed-loop PID controller is shown in Figure 5.15. The gains shown in Figure 5.15 (K_P , K_I and K_D) require precise tuning in order for the system to be stable. With the proper gains selected, PID controllers are normally very stable, to the point where they are used on approximately 95% of industrial control problems [44].

In the case of the ESLRV, the state to be controlled is the vertical angle of the jet engine. The error used in the PID controller, given by Equation 5.12, is the difference between the desired reference angle, typically zero, and the IMU sensed angle.

$$\tilde{\theta} = \theta_{ref} - \theta_{IMU} \quad (5.12)$$

Figure 5.16 depicts a typical pitch-angle restorative thrust vectoring vane deflection. Here the x-axis points along the direction of travel of the vehicle, the z-axis points downward, and the y-axis completes the set. The pitch angle corresponds to a “right-handed” rotation about the y-axis. The roll angle corresponds to a right-handed rotation about the x-axis.

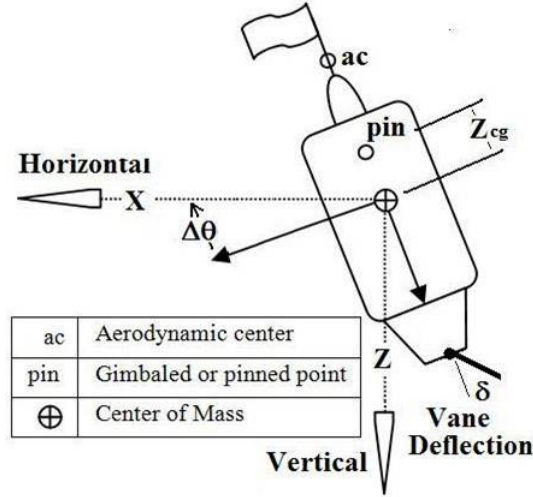


Fig. 5.16: Vane deflection for pitch angle trim.

The pitch and roll axes each have their own separate PID control law. The PID control law for the pitch axis is given by

$$K_P \tilde{\theta} + K_D \frac{d}{dt} \tilde{\theta} + K_I \int^t \tilde{\theta} \Delta t = \frac{M_y}{I_{yy}} \quad (5.13)$$

while a similar PID control law is used for the roll axis.

The parameter M_y in Equation 5.13 is the commanded pitching moment to be generated by the pitch axis turning vane and I_{yy} is the moment of inertia about the gimbal pitch axis. The gains K_P , K_D and K_I are initially selected using a variety of synthesis techniques, and then manually tuned to give acceptable controller performance.

Various methods can be used to discretize Equation 5.13 for implementation on a digital computer, with the most common method being the bi-linear transform [45]. When the bi-linear transform is used to discretize the controller the resulting difference equation is

$$M_y = M_{y_{k-1}} + K_P I_{yy} [\theta_k - \theta_{k-1}] + K_D \frac{I_{yy}}{\Delta t} [\theta_k - 2\theta_{k-1} + \theta_{k-2}] + K_I I_{yy} \Delta t \quad (5.14)$$

In Equation 5.14, the time indices k , $k-1$, and $k-2$ correspond to the current, previous,

and previous minus one sampled data points. Δt is the discrete time interval between data points. The numerically differentiated pitch angle data can lead to a noisy control signal; however, Equation 5.14 can be rewritten to directly use the pitch rate output by the IMU. This reformulated control law becomes

$$M_y = M_{y-1} + K_P I_{yy} [\theta_k - \theta_{k-1}] + K_D \frac{I_{yy}}{\Delta t} [q_k - q_{k-1}] + K_I I_{yy} \Delta t \quad (5.15)$$

This reformulated control law also has the added benefit of faster operation in that it requires fewer calculations and is required to only work from two frames of sampled data instead of three frames.

Chapter 6

Test Results

In preparation for a combined systems flight test, the inner and outer platforms were separately built up and tested. The outer platform's maneuvering controls were tested in tethered and free flights. The thrust vectoring system was built and installed on the jet engine which was once again placed in the 6 DOF test stand. A series of static tests were performed to test the effectiveness of the TVC system. The results of these tests are discussed in this chapter. As a required input of the PID control system, the rotational inertias of the inner platform were measured and are reported herein. Following the static tests and the measurement of the rotational inertias, a series of free gimbal ground tests were performed. These tests were conducted to ensure that the thrust vectoring system was able to stabilize the inner platform prior to flight testing. The results of these ground tests are also presented in this chapter.

6.1 Outer Platform 1-G Free Flight Tests

A lengthy series of flight tests were conducted on the outer platform maneuvering system. The VALASARAPTOR control method presented in (3.2.1) was used on the vehicle for the first several flight tests. Having no control surfaces (rudder, aileron or elevator), a quadrotor system relies entirely upon differential thrust for stability and maneuvering control. The VALASARAPTOR control method remaps the RC transmitter's signals for throttle, yaw, pitch and roll to four individual throttle signals. Ideally, this would have allowed the outer platform to be flown in an open-loop system that would have the feel of flying a standard RC airplane or helicopter.

Initial flight tests employed the semi-tethered system shown in Figure 6.1. The tethers consisted of fiberglass rods that were attached to the vehicle on one end and had lengths

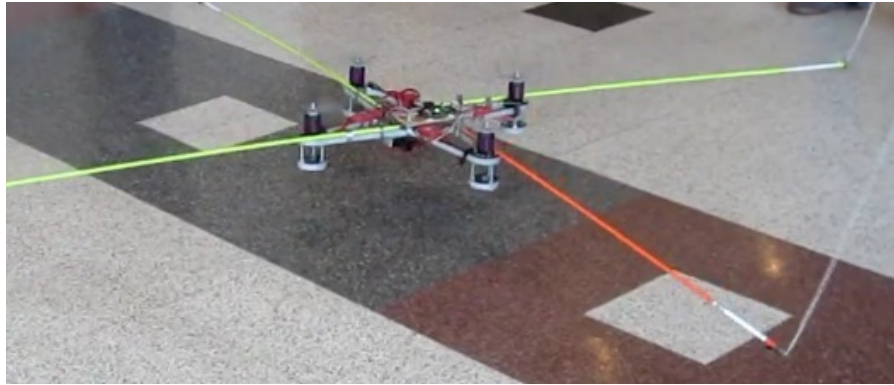


Fig. 6.1: Tethered flights of the outer platform maneuvering system using the VALASARAPTOR open-loop control method.

of rope attached to the other. The ropes were held by four members of the test team who could follow the motion of the vehicle and react to prevent the vehicle from crashing should something go wrong. The structure shown in Figure 6.1 was a temporary one built to facilitate early testing while the final ESLRV structure design was finalized.

The tethers were frequently required on tests that employed the VALASARAPTOR system. The open-loop system was unstable and too difficult to fly. The pilot's reaction was often too slow and too strong. Fearing that the tethers themselves were contributing to the vehicle's instability, they were removed and a few free flight tests were conducted. These tests all ended in failure.

Controllability of the outer platform improved with the use of the QuadPowered® control board discussed in (3.2.1). Initial tests with this new controller also utilized the tethers shown in Figure 6.1. The QuadPowered® control board stabilized the vehicle enough for simple hovering flights, however, vehicle maneuverability still suffered. The tethers were removed and the system's stability and maneuvering performance greatly improved. The flexible fiberglass rods acted as a spring-mass-damper system that degraded the vehicle's stability.

Following the initial success with the QuadPowered® control board, the rotors and associated support equipment were moved to the now completed final structure pictured in Figure 6.2. The legs for the landing gear were shortened for the remainder of the flight



Fig. 6.2: Free flight tests of the outer platform maneuvering system using the QuadPowered board controller.

tests in order to reduce the outer platform's weight. The four rotors were designed to carry only $1/6^{th}$ of the total vehicle weight. The outer platform, with full length landing gear, exceeded that weight. Figure 6.2 shows the outer platform in its final configuration during one of many successful flight tests.

6.2 Static Thrust Vectoring Tests

Figure 6.3 shows the load cell outputs for a typical test, adjusted for their initial zero offsets. In this test, the throttle setting was incrementally increased from idle to 100%. At each throttle setting, the pitch vane was swept through a deflection range from -5° through 5° . Figure 6.3a plots the load cell outputs. Figure 6.3b plots the vane deflections. The engine throttle settings are also indicated on the load graph. The effects of the vane deflections are clearly visible on all six load cell readings.

In Figure 6.3a, the level of the lateral load cell outputs can be seen to drift away from center as the throttle was increased. This drift is a test stand artifact, and is likely caused by deflections in the load cells and the test stand structure itself. To correct for this effect, each lateral load cell voltage was reduced by an amount directly proportional to the corresponding axial load cell voltage according to Equation 6.1.

$$V_{\{I\}l_{adj}} = V_{\{I\}l} + k_{\{I\}} V_{\{I\}a} \quad (6.1)$$

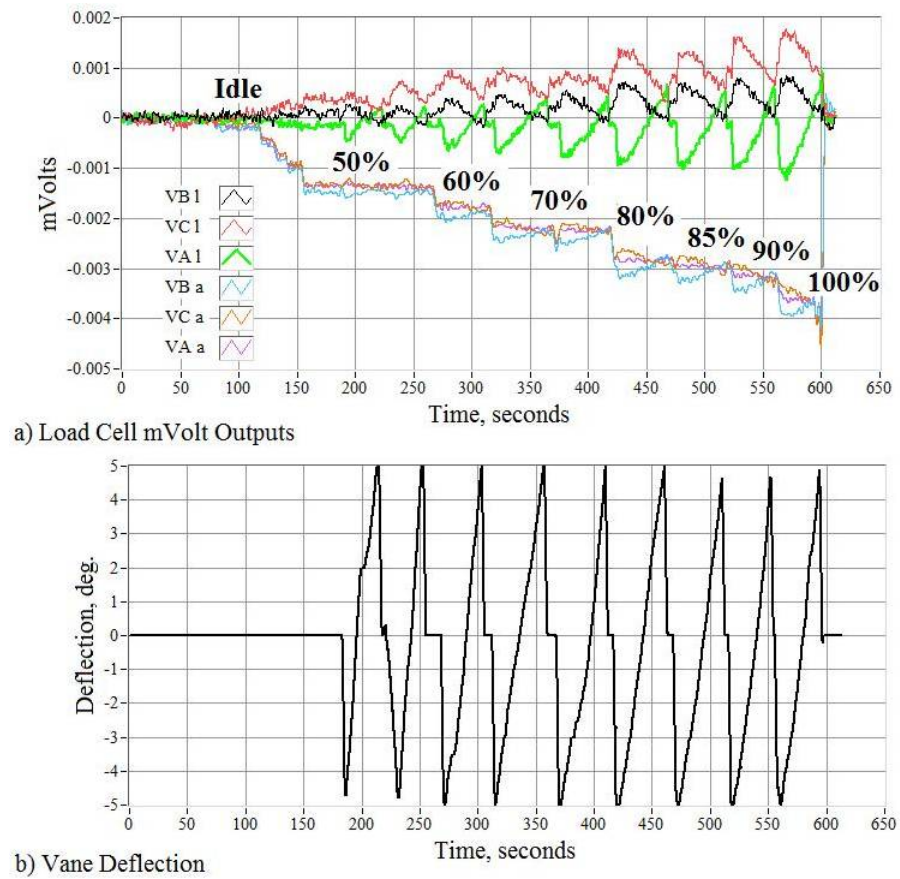


Fig. 6.3: Load cell mV output for a typical thrust vectoring test case.

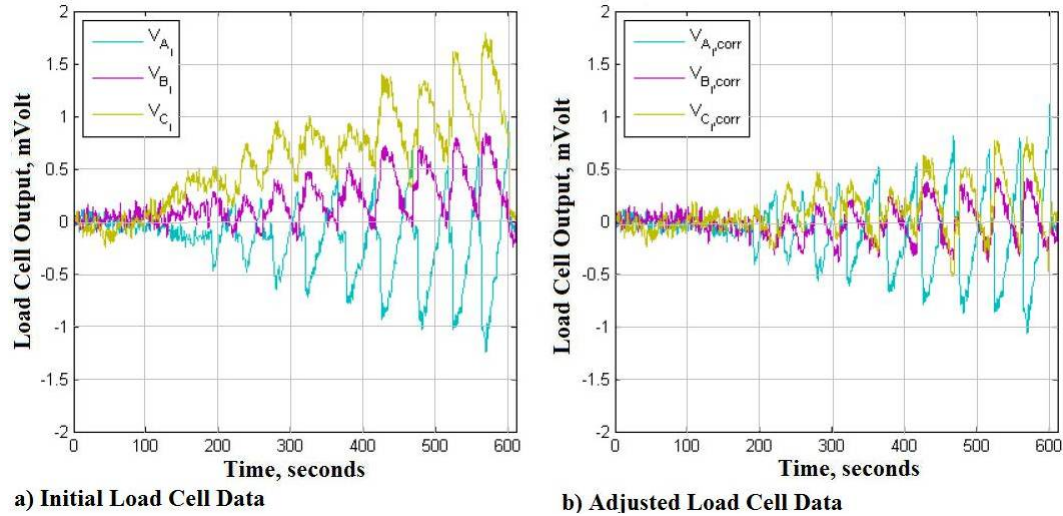


Fig. 6.4: Comparison of original and adjusted load cell readings.

In Equation 6.1, the index I corresponds to the load cell indices A, B , and C . The subscript l implies a lateral load cell reading, and the subscript a implies an axial load cell reading. These coefficients were selected to minimize the drift of the mean lateral load signal away from the zero trim-line. Figure 6.4 compares the original (a) and adjusted (b) lateral load cell readings. The drift is dramatically reduced.

Figure 6.5 plots the forces and moment for all three axes using the adjusted load cell data. The F_z force data corresponds to a positive thrust level. Cross-talk between the axes has been virtually eliminated. However, there is a slight pitching moment asymmetry, which is likely due to the combined effects of exit plane wake asymmetry and vorticity in the flow. The exit plane asymmetry can be clearly observed in Figure 4.6. The lower velocity on the right-hand side of the wake has the effect of reducing the vane effectiveness in that direction.

A curve-fit was applied to the moment data of Figure 6.5 to generate the pitch axis, look-up table data presented in Figure 6.6a. A similar look-up table data set was generated for the vehicle roll axis. The magnitude of the measured vectoring force is considerably less than was predicted during the TVC design phase. The data from Figure 5.10 was replotted in Figure 6.6b with reversed axes for ease of comparison to Figure 6.6a. Comparing these figures shows that the measured moment about the gimbal point is approximately 40%

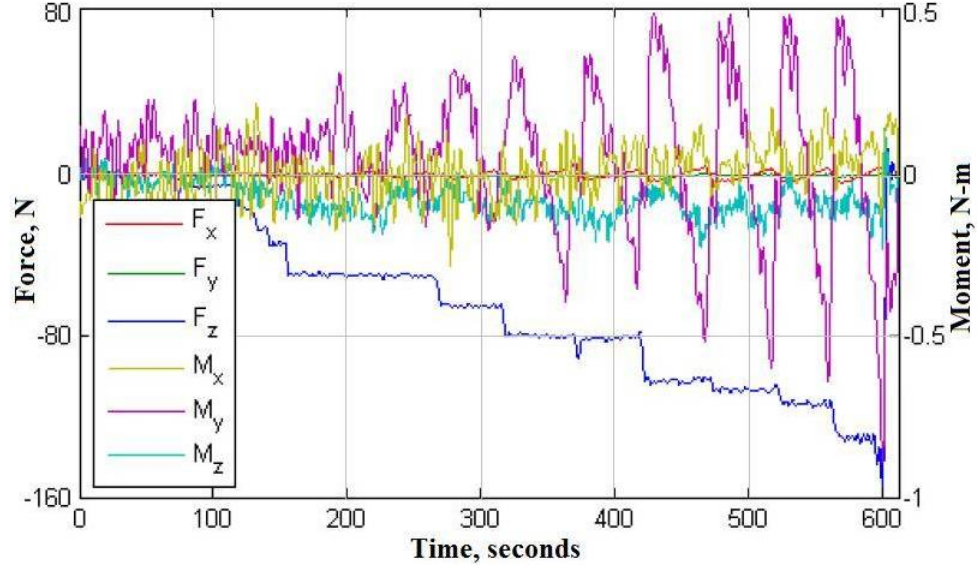


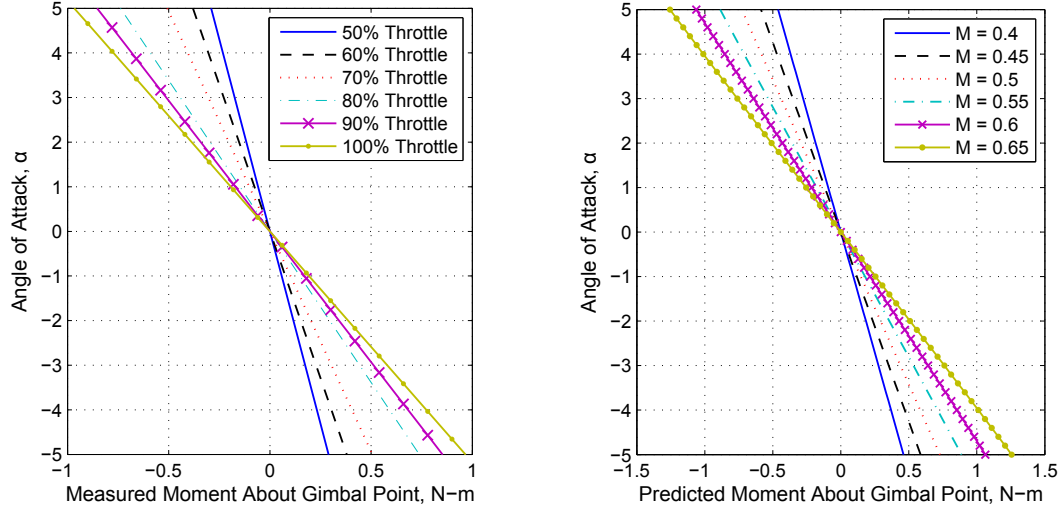
Fig. 6.5: Calculated thrust vectoring forces and moments using adjusted load cell data.

lower than the predicted moment as defined by Equation 6.2.

$$\text{Percent Difference} = \frac{\text{predicted moment} - \text{measured moment}}{\text{predicted moment}} 100\% \quad (6.2)$$

As an example, assume that the engine is running at 75% throttle. The desired moment computed by the PID algorithm is 0.62 N-m. By examining Figure 6.6a and interpolating between the 70% and 80% throttle lines, it is determined that an angle of attack of -5° is required to achieve the desired pitching moment of 0.62 N-m. Recalling the analysis of (4.3), an engine throttle setting of 75% has an average Mach number of approximately 0.6. Examining Figure 6.6b reveals that, at Mach 0.6, an angle of attack of -5° produces a pitching moment of 1.06 N-m. Using these numbers in Equation 6.2, the measured moment is calculated to be 41.5% less than the predicted moment.

Clearly the linear potential-flow model used to design the turning vanes does not account for several essential flow field factors that contribute to the reduced lift of the airfoils. The cause of the reduced gimbal point moment at lower throttle settings is not definitively known, though it is likely due to a combination of the rotational swirl of the exit plume,



(a) Actual relationship between the airfoil angle of attack and the gimbal point moment. (b) Predicted relationship between the airfoil angle of attack and the gimbal point moment.

Fig. 6.6: Airfoil angle of attack required, as a function of throttle setting (or Mach number), to achieve a desired moment for the vehicle's pitch axis.

discussed in (4.4), and interfering flow fields produced by the two orthogonal sets of airfoils.

As expected, the thrust vectoring vanes slightly reduce the total thrust available from the engine. Figure 6.7 shows the thrust vs. RPM curve measured with the vectoring system installed as compared to the engine manufacturer's published data and the thrust measured without the vectoring system. The vanes were held at a zero degree deflection angle during these measurements. The addition of the vectoring system reduces the available thrust by 17-18% at the 85% operational throttle setting.

6.3 Moment of Inertia Measurements

Before a combined systems test (CST) could be performed, it was essential to understand the rotational inertia, natural frequency, and damping ratio for both the pitch and roll axes of the inner platform. A series of inertia swings were performed to estimate these parameters. The process follows the method outlined by Wolowicz and Yancey [46]. The platform dynamics for each axis were modeled as a simple linear pendulum. This

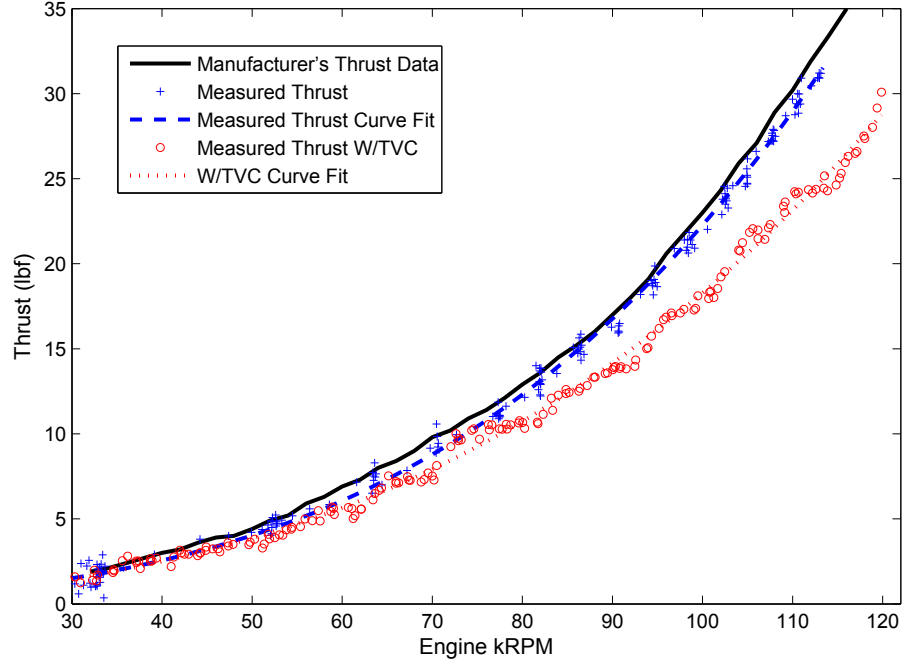


Fig. 6.7: JF-170 Rhino thrust vs. RPM curve with the vectoring system installed.

second-order model is valid for small angle approximations, and, for the pitch axis, is given by

$$\ddot{\theta} + \frac{B}{I_{yy}}\dot{\theta} + \frac{K}{I_{yy}}\theta = \frac{M_y}{I_{yy}} \quad (6.3)$$

An identical expression can be written for the roll axis. In Equation 6.3, the parameter B is the rate damping term and K is the torsional spring coefficient. For the inertial swing tests, the platform was perturbed to a non-zero position and allowed to swing freely ($M_y = 0$) and the acceleration time histories along each axis were recorded by accelerometers. Tests were performed with the fuel tank empty, partially full, and entirely full. Interestingly, the response time histories showed almost no dependence on the fill level of the fuel tank. If the linear pendulum model is valid, this result is as expected. Figure 6.8 shows typical responses for both the pitch and roll axes.

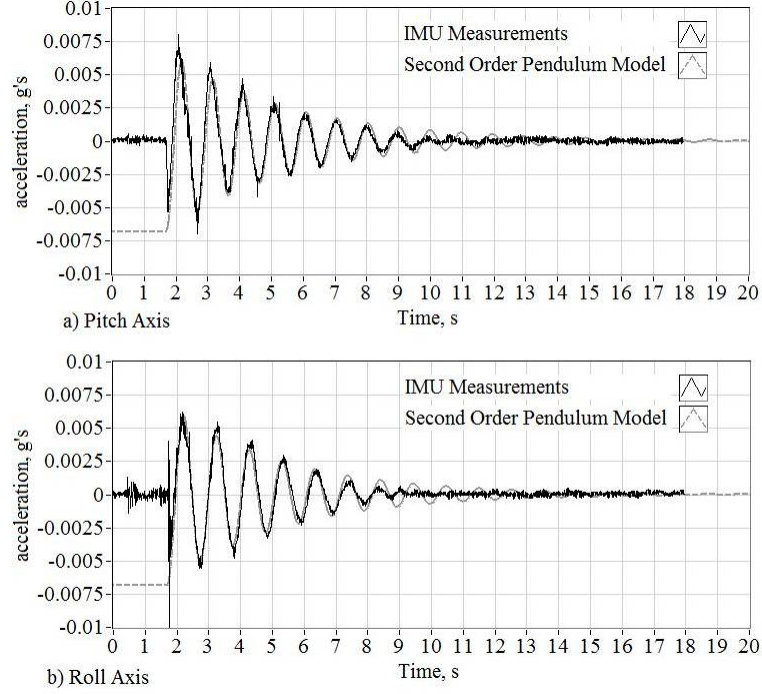


Fig. 6.8: Unforced response of inner platform compared to pendulum model.

When written in terms of the natural frequency and damping ratio [47], the unforced response of the inner platform is

$$\ddot{\theta} + 2\zeta\omega_n\dot{\theta} + \omega_n^2\theta = 0 \quad (6.4)$$

where the natural frequency and damping ratio respectively are

$$\omega_n = \sqrt{\frac{K}{I_{yy}}}, \text{ and } \zeta = \frac{B}{2\sqrt{KI_{yy}}} \quad (6.5)$$

The pendulum-model responses plotted in Figure 6.8 use the best-fit estimates for the natural frequency and damping ratio. Table 6.1 lists these parameters. The data presented in Figure 6.9 verifies the best-fit calculations for natural frequency. The power spectrum magnitude of the response-time histories is plotted against cyclic frequency. For both axes, there are distinct response peaks near 1 Hz. The secondary peak near 2 Hz on the pitch axis plot is very likely due to fuel slosh in the tank. Clearly, the system is very lightly damped, and any non-steady input has the potential to grow. Also, the natural response

Table 6.1: Best-fit Linear Pendulum Model Parameters for the Inner Platform

Axis	ζ	ω_n (rad/s)	f_n (Hz)
Pitch Axis	0.04	6.44	1.025
Roll Axis	0.045	6.09	0.97

Table 6.2: Inner Platform Mass, Vertical Center of Gravity and Moment of Inertia Estimates

Pitch Axis	Mass (kg)	ω_n (rad/s)	Z_{cg} (cm)	Inertia (kg-m ²)
Tank Empty	6.67	6.44	10.2	0.161
Tank Full	8.33	6.44	9.0	0.177
Roll Axis	Dry Mass (kg)	ω_n (rad/s)	Z_{cg} (cm)	Inertia (kg-m ²)
Tank Empty	7.14	6.09	10.2	0.193
Tank Full	8.80	6.09	9.0	0.209

frequency, near 1 Hz for both axes, must not be excited by the thrust vectoring control algorithm. These considerations are of paramount importance when selecting the control law parameter values.

Assuming the “spring force” that returns the inner platform to its vertical orientation is entirely due to the vertical offset of the center of gravity from the gimbal pivot (Z_{cg}), the torsional spring constant can be estimated as

$$K = m_{inner}gZ_{cg} \quad (6.6)$$

where m_{inner} is the mass attached to the inner platform and g is the acceleration of gravity. Using this expression, the principal rotational inertia of the inner platform about the pitch axis can be estimated by

$$I_{yy} = \frac{K}{\omega_n^2} = \frac{m_{inner}gZ_{cg}}{\omega_n^2} \quad (6.7)$$

A similar expression exists for the roll axis. Based on material and component weight estimates and the fuel mass, Table 6.2 shows the estimates of the moments of inertia and other accompanying parameters for full and empty fuel tanks.

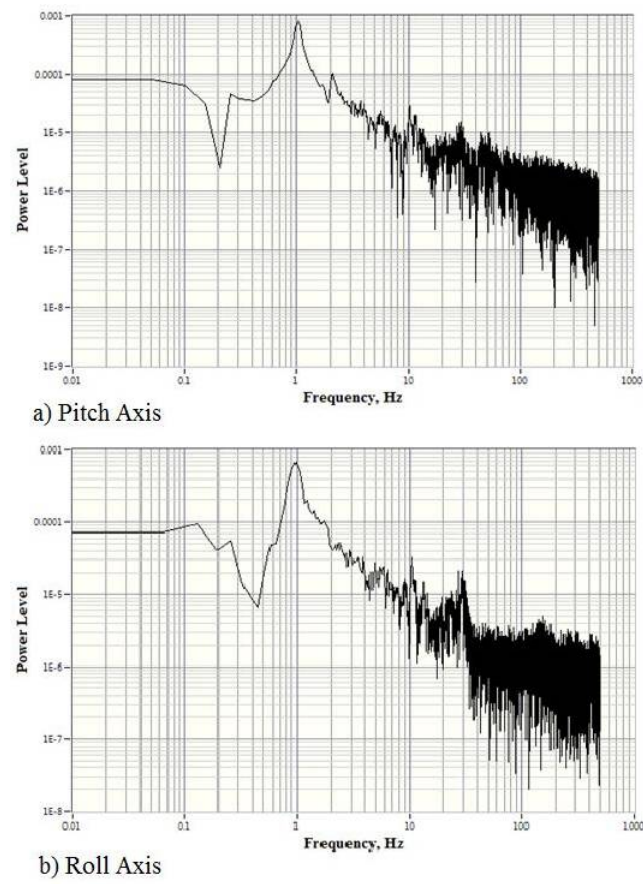


Fig. 6.9: Inner platform unforced response spectrum magnitude.

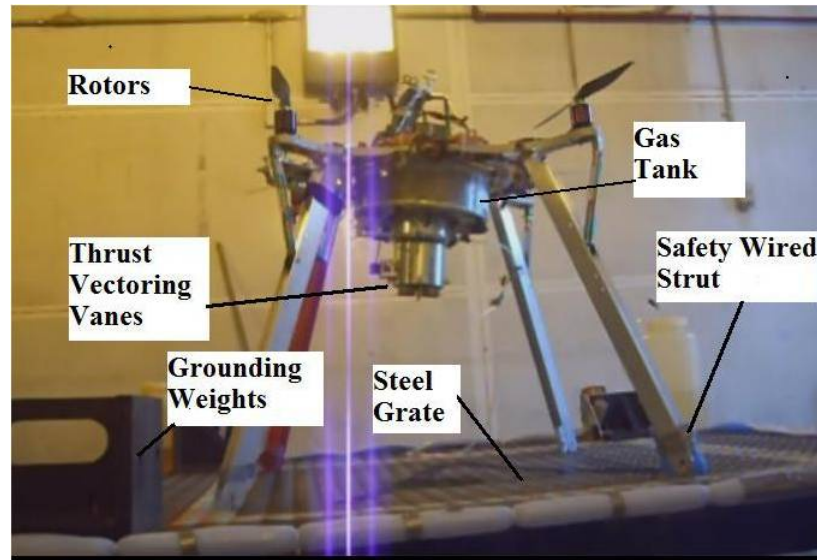


Fig. 6.10: Test setup for TVC ground tests.

6.4 Free Gimbal Combined Systems Tests

A series of CSTs were performed prior to the first hover flight test in order to evaluate the performance of the thrust vectoring controls. The objectives of these free-gimbal tests were to verify the system stability, and also to demonstrate that the thrust vectoring system could effectively control the pitch and roll angles of the inner platform. Figure 6.10 shows the test arrangement. The fully integrated vehicle was placed in the test cell on a steel grate test stand which suspended the nozzle exit plane approximately one meter above the test cell floor. The ESLRV's legs were safety-wired to the grate, which was weighted to prevent the vehicle and the test stand from lifting off the ground.

Depending on the test objective, the pitch and roll gimbals could be locked in place or allowed to rotate. Tests with either gimbal locked and with both gimbals free to rotate were performed. The annular gas tank attached to the inner platform was fully fueled at the start of each test. The full fuel tank holds approximately 1.66 kg of kerosene; enough for approximately five minutes of engine run time at 85% throttle.

The first attempts at controlling the inner platform with the PID controller were unsuccessful. The PID controller was extremely sensitive to disturbances and gain selection. Small changes in the selected gains would excite pitch and roll axis gyroscopic coupling

(caused by the rotating jet turbine), and the platform controller would become entirely unstable.

6.4.1 Proportional Filtered Control Method

With the failure of the PID control law and in order to expedite early flight testing in a near-hover operating mode, a less complex control law was implemented. This algorithm, while very sluggish with regard to the allowable maneuvering performance, is highly robust and allows for significant parameter variations to be performed without continuously exciting the gyroscopic coupling. This control algorithm uses only a proportional error feedback and filters which insure that the moment command frequency is significantly lower than the natural rotational frequency of the inner platform. The coupled filter tends to dampen noisy oscillations in the IMU attitude measurements. Also, the low frequency commands do not excite inter-axis gyroscopic coupling. Because the early tests were intended only to demonstrate the ability of the vehicle to achieve a stable hover condition, the sluggishness of the control command was not an issue.

The form of the hover control law assumes a second order filter of the form

$$\frac{d^2}{dt^2}M_y + 2\zeta\omega_n\frac{d}{dt}M_y + \omega_n^2M_y = \omega_n^2I_{yy}K_p\tilde{\theta} \quad (6.8)$$

In Equation 6.8, ω_n is the natural radian frequency of the filter, and ζ is the damping ratio. When Equation 6.8 is converted to the frequency domain and discretized, the resulting difference equation is

$$(M_y)_k = \frac{a^2}{b}(E_k + 2E_{k-1} + E_{k-2}) - \left(\frac{c}{b}(M_y)_{k-1} + \frac{d}{b}(M_y)_{k-1}\right) \quad (6.9)$$

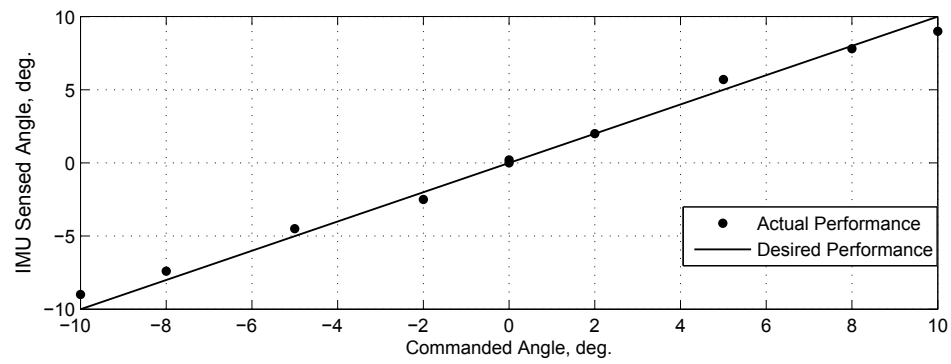
In Equation 6.9, the coefficients a , b , c , and d are given by

$$\begin{bmatrix} a = \omega_n \left(\frac{\Delta t}{2} \right) \\ b = 1 + 2\zeta a + a^2 \\ c = 2(a^2 - 1) \\ d = 1 - 2\zeta a + a^2 \end{bmatrix} \quad (6.10)$$

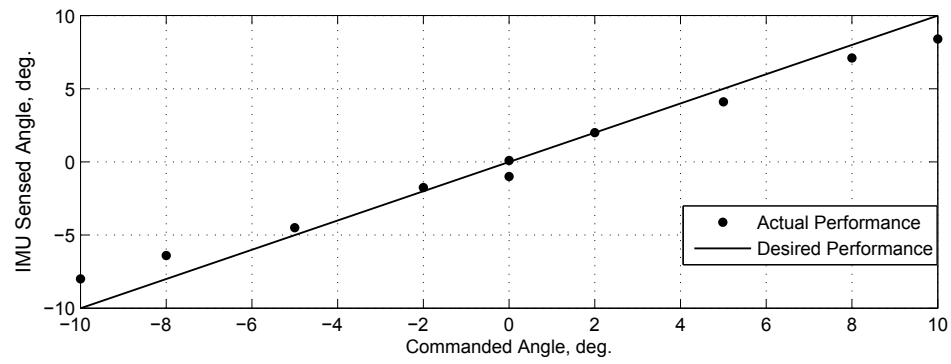
6.4.2 Proportional Filtered Control Law Tests

As was mentioned previously, this interim control law was developed to expedite early flight testing in a near-hover operating mode. The test procedure started with the vectoring control proportional gains set to zero for both pitch and roll axes. The initial damping ratio was set to 1.0 and the cyclic natural frequency was set to 0.1 Hz. The commanded reference control angles were set to zero. The engine was started, allowed to stabilize, and ramped up to 35% throttle. The control gain was gradually increased until the vehicle began to demonstrate signs of oscillatory instability. The primary feature of this instability was a gyroscopic coupling between the pitch and roll axes. If not abated, this coupling would eventually cause the vehicle to become entirely unstable. As the vehicle approached incipient instability, the gain was halved and the pitch and roll oscillations were allowed to dampen out. Once this acceptable gain was selected, then a similar approach was performed for the natural frequency of the filter. The filter frequencies were gradually increased until an incipient instability was once again encountered. At this point the frequency was halved, and the system was allowed to stabilize.

This process was performed repeatedly with the throttle gradually increased to the desired 85% level. Once the 85% throttle level was reached, the commanded pitch and roll angles were varied to place the engine in multiple pitch and roll orientations. This approach verified that the engine could be precisely pointed, and remain stable while maneuvering from one commanded angle set to another. The commanded angle limits varied between $\pm 10^\circ$. Figure 6.11 shows the inner platform's response to various pitch and roll angle commands. Each of the commanded orientations was held approximately five seconds before the next angle set was commanded.



(a) Pitch axis



(b) Roll axis

Fig. 6.11: Commanded orientation vs. IMU sensed orientation for both pitch and roll axes.

Chapter 7

Thrust Vectoring System Design Evolution

The successful control mentioned in the previous chapter occurred only once. Since that test, the vehicle has been beleaguered with issues. Aluminum shavings from the fuel tank clogged the FADEC-controlled fuel valve and destroyed the fuel pump. Additionally, the thermocouple, glowplug and starter motor failed at separate times requiring replacement of each part. While these were only minor setbacks that could be easily remedied, each failure caused a delay in testing of at least a few days, if not weeks. Figure 7.2 illustrates the design evolution of the vehicle as the research team worked to fix root cause of each successive failure.

Two much bigger issues, however, did occur that caused delays of several months in the ground tests. As a result of the the aluminum shavings, the fuel valve could not close properly. Unknown to the test crew, after an unsuccessful engine start, fuel had been spraying into the combustion chamber and was not burned. With the engine in a vertical orientation, the combustion chamber forms a bowl with no outlet for the unburned fuel. On the next start attempt, the unburned fuel suddenly combusted resulting in what is termed a hot start. At the first sign of trouble, the startup procedure was shut down and the fire was quickly put out, but the initial explosion of fuel warped the exhaust gas vanes. The jet engine had to be sent back to the factory to be repaired.

During the month that the engine was being repaired, efforts focused on the other major setback. It was noted after the initial success of the proportional filtered control law that, during tests thereafter, the IMU would stop working a short time after the jet engine was started. Without continuous data from the IMU, the control algorithms could not work. The original avionics setup had the IMU and FADEC communicating with the flight computer through an externally powered USB hub. It was thought that the USB hub

was sensitive to either vibration, or some electromagnetic interference from the jet engine. The hub was replaced with a new one, yet the problem persisted.

Next, a new logic level shifting board was built so that the FADEC could communicate directly through a hardwired RS-232 connection with the flight computer allowing the IMU to communicate directly through the one available USB port. This setup eliminated the need for the USB hub, yet still resulted in loss of IMU data during the engine startup procedure. A second logic level shifting board was built that allowed both the FADEC and the IMU to communicate through separate hardwired RS-232 connections. It was hoped that the USB port had a loose connection that was susceptible to vibrations. Eliminating it would hopefully fix the issue; however, this attempt at a fix also failed.

In addition to altering the connection and communication methods of the avionics package, the IMU was put through a series of tests to see if the sensor itself was sensitive to either vibrations or magnetism. The entire avionics package was exposed to strong magnetic fields and a spectrum of vibrations up to 10,000 Hz. The error could not be duplicated. The avionics package proved that it was durable enough to handle both intense vibrations and electromagnetic interference.

The last attempt to fix the issue with the IMU involved wrapping it in foam to try to isolate it from acoustic interference. The jet engine creates an intense volume of sound on the order of 130 dB or more. The bar graph shown in Figure 7.1 shows the acoustic levels measured at third octave intervals within the range of human hearing, typically 20 Hz to 20,000 Hz. These measurements were made by a Casella CEL-573 real-time acoustic analyzer [48]. This sensor is commonly used for short-term environmental noise surveys within the range of human hearing. The data shows that individual third octave intervals can have acoustic levels over 130 dB. The overall acoustic level was measured at 134.3 dB. Levels above 130 dB can cause instant permanent hearing loss. The acoustic analyzer used only measured acoustic levels in frequencies up to 20,000 Hz. It can be assumed that the jet engine is creating acoustic noise well above this value as the data shows a nearly continuously upward trend in dB level as the frequency level increases.

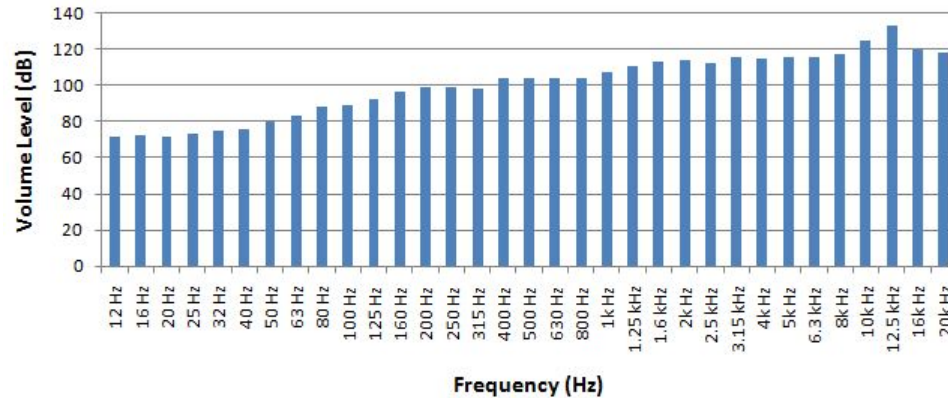


Fig. 7.1: Sound levels produced at third octave frequencies by the JF-170 jet engine.

An acoustic isolation box was built to shield the IMU from the sound field created by the jet engine. The box was lined with silicone and a sound isolation tar commonly used with car audio systems. When placed in this sealed box, the IMU was able to continuously send good data to the on-board flight computer. The IMU was apparently sensitive to intense acoustical vibrations.

With the IMU shielded against the engine's noise a few additional ground tests took place. A third controller was used on these last few ground tests. This new controller, an enhanced PID method, used six gains on each axis in an attempt to account for the cross-axis gyroscopic coupling. In an attempt to better understand the vehicle's dynamics, and hopefully to design a more robust control system, a high-fidelity model of the ESLRV's inner platform was created in Simulink®. This model used a linear quadratic regulator (LQR) [43] to predict the twelve gains that would be used on the actual vehicle. The Simulink® model showed that this new controller was more robust than a normal PID controller and was faster at restoring the engine to its proper orientation.

The IMU worked well During the last few ground tests, but the new controller was unable to prevent the gyroscopic instabilities from taking over. This enhanced PID controller did prevent the system from becoming completely unstable as was seen during earlier ground tests with the standard PID controller, but it was still not stable enough for a hovering flight test. Finally, in late January 2011, during one of the ground tests, a second

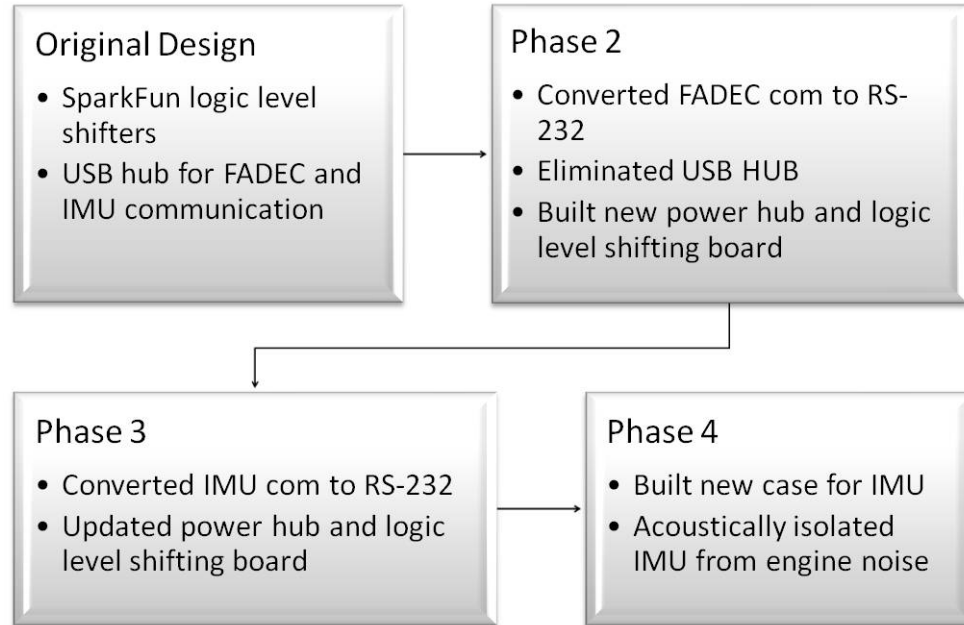


Fig. 7.2: Design progression of the inner gimbal avionics.

engine fire, cause unknown, permanently ended all future tests and a hope for a working TVC system. Budget and time constraints did not allow for the lengthy and costly repair process required to restore the engine to operational status.

Chapter 8

Conclusions

A method for attitude control of a vertically thrusting jet engine has been demonstrated. This method used airfoils placed in the high-speed exhaust flow of the jet engine to vector some of the engine's thrust for use in controlling engine's attitude. Precise attitude control of the jet engine, serving as a means for gravity offset, is necessary to achieve a successful, free-flying, reduced-gravity simulation.

Ground tests show that, in its current configuration, the aerodynamic thrust vectoring system built for the ESLRV is not yet capable of stable attitude control of the inner gimbal. Testing revealed the cross-axis gyroscopic coupling to be a dominant source of error. This gyroscopic coupling quickly grows to a full limit instability that eliminates the possibility of stable flight.

Ground tests with the proportional filtered controller demonstrated that the TVC system is capable of holding a commanded attitude. This controller, however, lacks sufficiently fast enough response times in order to be a viable controller for flight tests. The standard PID controller, having response times on the order of milliseconds, was entirely unable to stabilize the inner gimbal and served only to excite the gyroscopic coupling into a full limit instability.

Efforts were made to improve the standard PID controller so that it could predict and account for the strength of the cross-axis gyroscopic coupling. A linear quadratic regulator was used to calculate twelve gains (six for each axis). Three gains on each axis were designated for the standard proportional, integral and derivative gains. The additional three gains on each axis were again proportional, integral and derivative gains, but were used to account for and predict cross-axis motion.

This improved PID controller was still not able to completely overcome the gyroscopic

coupling motion. It did, however, limit the effect of this incipient error source as it did not grow to become a full limit instability. It is believed that, with the appropriate changes to the gains, the improved PID controller would have been able to successfully stabilize the inner gimbal. This may never be known, as the second engine fire and associated schedule and budget constraints eliminated the possibility of further testing.

One possible reason the TVC system was not able to achieve stable attitude control is the lack of sufficient control authority. The disparity between the predicted and measured gimbal point moments – a difference of approximately 40% – supports this theory. This gimbal point moment disparity is likely the result complex flow interactions produced by the swirl of the exhaust flow and the orthogonal airfoil pairs.

A new nozzle that molds the exit-plane velocity profile into a uniform profile equal to the current average exit velocity should be investigated. This nozzle would reduce the effects of swirl and the effects of complex flow interactions. A uniform flow nozzle would also eliminate the momentum hole, discovered during engine characterization, and possibly increase the thrust produced by the engine. A new jet engine with a more ideal exit-plane flow field could be used as an alternative to replacing the nozzle on the existing jet engine.

Additionally, the vehicle's structure and fuel tank are not of an optimal design and unnecessarily increase the inner platform's rotational inertia while subsequently decreasing the TVC system's control authority. Optimizing the structure and fuel tank design could have many benefits including decreasing the vehicle's mass and increasing the TVC system control authority.

Table 8.1 presents a roadmap for future work on the ESLRV or a similar vehicle. The benefits from using a new nozzle (or jet engine) and other research efforts are detailed in Table 8.1. Some of these benefits include: an increased understanding of the behavior of the TVC system, and an increase in the control authority of the TVC system. Increasing the control authority has the added benefit of decreasing the deflection angle required for a desired gimbal point moment. This in turn would decrease the system response time, allowing for the controller to respond faster to disturbances in attitude.

Table 8.1: Roadmap for Future Research

Research Effort	Method	Benefit
Resolve disparity between predicted and measured gimbal point moment	3-D CFD model of nozzle and airfoils	Better prediction of gimbal point moment: more accurate prediction of TVC system behavior
	New nozzle (or jet engine) with a slower, uniform velocity profile	No rotational swirl and no localized reduction in lift: increased control authority
Reduce the inner platform's angular momentum	Optimize tank size, shape and weight (suggest molded plastic)	Increased control authority
	Optimize gimbal ring size and weight	Increased control authority
Improve the Simulink [®] model and the PID control method	Measure angular momentum of turbine instead of using best estimate	Greater accuracy in prediction of controller gains
	Pivot inner platform at its center of gravity	Able to discretize controller algorithm from simplified equation of motion and then do a control law analysis to optimize gains for desired behavior

Despite the issues observed during ground testing, the aerodynamic TVC system presented has demonstrated its potential as a viable attitude control method. The continued development of this research and other technologies that allow “pin-point” autonomous landing systems to be evaluated, refined, and matured is essential to the future of extraterrestrial exploration.

Perhaps the biggest lesson learned from this design effort is that building and flying a vehicle with 11 degrees of freedom motion is a very daunting task. The 1960’s era LLRV and LLTV design were notable in that they successfully built such a complex vehicle that could fly. However, it can be justifiably argued that flying the LLRV and LLTV during training was more dangerous than the lunar landing itself.

In the pre-apollo era, the analog flight approach was the best available simulation option. In the modern era, with a variety of simulation and computer generated image (CGI) options available, it is more likely that a reduced order system, with several degrees of motion freedom constrained and adjusted for using CGI, may provide a safe flight simulation environment with high enough fidelity that is sufficient for pilot training.

It is likely that the physical-analog gravity offset system creates the most realistic simulation. However, the risks inherent in an 11 degrees of motion freedom vehicle will likely limit the usefulness of the physical gravity offset to unmanned, autonomous vehicles.

REFERENCES

- [1] Review of U.S. Human Spaceflight Plans Committee [Augustine Committee], “Seeking a Human Spaceflight Program Worthy of a Great Nation,” http://www.nasa.gov/offices/hsf/meetings/10_22_pressconference.html, [retrieved 21 July 2011].
- [2] David R. Williams, “Lunar Exploration Timeline,” <http://nssdc.gsfc.nasa.gov/planetary/lunar/lunartimeline.html>, [retrieved 8 May 2010].
- [3] Williams, D. R., “Chronology of Mars Exploration,” http://nssdc.gsfc.nasa.gov/planetary/chronology_mars.html, [retrieved 8 May 2010].
- [4] Lunar and Planetary Institute, “Apollo 11 Mission - Landing Site Overview,” http://www.lpi.usra.edu/lunar/missions/apollo/apollo_11/landing_site/, [retrieved 9 August 2011].
- [5] National Aeronautical and Space Association, “Four out of Six Apollos,” <http://www.nasa.gov/topics/moonmars/features/alhat20081223.html>, [retrieved 18 May 2010].
- [6] Howe, S. D., O’Brien, R. C., Ambrosi, R. M., Gross, B., Katalenich, J., Sailer, L., Webb, J., McKay, M., Bridges, J. C., and Bannister, N. P., “The Mars Hopper: An Impulse-Driven, Long-Range, Long-Lived Mobile Platform Utilizing In Situ Martian Resources,” *Proceedings of the Institution of Mechanical Engineers, Part G: Journal of Aerospace Engineering*, Vol. 225, No. 2, 2011, pp. 144–153.
- [7] Johnson, A., Huertas, A., Werner, R., and Montgomery, J., “Analysis of On-Board Hazard Detection and Avoidance for Safe Lunar Landing,” *Aerospace Conference, 2008 IEEE*, March 2008, pp. 1–9.

- [8] O'Bryan, T. C., and Hewes, D. E., "Operational Features of the Langley Lunar Landing Research Facility," NASA TN D-3828, 1967.
- [9] Nassif, S. H., and Armstrong, N. A., "Apollo Flight Crew Training in Lunar Landing Simulators," *Presented at the 2nd AIAA Flight Test, Simulation, and Support Conference*, AIAA Paper 68-254, 1968.
- [10] Matranga, G. J., Ottinger, C. W., Jarvis, C. R., and Gelzer, D. C., "Unconventional, Contrary, and Ugly: The Lunar Landing Research Vehicle," *Monographs in Aerospace History*, Vol. 35, NASA SP-2004-4535, 2005.
- [11] Ottinger, D. W., "Go For Lunar Landing Conference: From Terminal Descent to Touchdown," <http://ser.sese.asu.edu/GO/>, [retrieved 28 October 2009].
- [12] Jet Central[®], "Rhino Operation and Maintenance Manual," [http://www.jetcentral.com.mx/manuales/RHINO%20KS\(Sin%20garantia\).pdf](http://www.jetcentral.com.mx/manuales/RHINO%20KS(Sin%20garantia).pdf), [retrieved 5 October 2009].
- [13] Bennet, F. V., "Apollo Lunar Descent and Ascent Trajectories," NASA TM-58040, 1970.
- [14] Sutton, G. P., and Biblarz, O., "Thrust Vector Control," *Rocket Propulsion Elements*, John Wiley & Sons, New York, NY, 7th ed., 2001, pp. 608–623.
- [15] Berrier, B. L., and Taylor, J. G., "Internal Performance of Two Nozzles Utilizing Gimbal Concepts for Thrust Vectoring," NASA TP-2991, 1990.
- [16] Carson, G. T., and Capone, F. J., "Static Internal Performance an Axisymmetric Nozzle with Multiaxis Thrust Vectoring Capability," NASA TM-4237, 1990.
- [17] Wing, D. J., Mills, C. T. L., and Mason, M. L., "Static Investigation of a Multiaxis Thrust-Vectoring Nozzle with Variable Internal Contouring Ability," NASA TP-3628, 1997.

- [18] Deere, K. A., Berrie, B. L., Flamm, J. D., and Johnson, S. K., “Computational Study of Fluidic Thrust Vectoring Using Separation Control in a Nozzle,” AIAA Paper AIAA-2003-3803, 2003.
- [19] Flamm, J. D., Deere, K. A., Mason, M. L., Berrier, B. L., and Johnson, S. K., “Experimental Study of an Axisymmetric Dual Throat Fluidic Thrust Vectoring Nozzle for Supersonic Aircraft Application,” AIAA Paper AIAA-2007-5084, 2007.
- [20] Eilers, S. D., Wilson, M. D., Whitmore, S. A., and Peterson, Z. W., “Side Force Amplification on an Aerodynamically Thrust Vectored Aerospike Nozzle,” *Presented at the 47th AIAA/ASME/SAE/ASEE Joint Propulsion Conference & Exhibit, San Diego, CA*, AIAA Paper AIAA-2011-5531, 2011.
- [21] Dungan, T., “A-4/V-2 Makeup - Tech Data and Markings,” <http://www.v2rocket.com/start/makeup/design.html>, [retrieved 7 June 2011].
- [22] Berrier, B. L., and Mason, M. L., “Static Performance of an Axisymmetric Nozzle With Post-Exit Vanes for Multiaxis Thrust Vectoring,” NASA TP-2800, 1988.
- [23] Bowers, A. H., and Pahle, J. W., “Thrust Vectoring on the NASA F-18 High Alpha Research Vehicle,” NASA TM-4771, 1996.
- [24] Alcorn, C. W., Croom, M. A., Francis, M. S., and Ross, H., “The X-31 Aircraft: Advances In Aircraft Agility and Performance,” *Progress in Aerospace Sciences*, Vol. 32, 1996, pp. 377–413.
- [25] Anon., “Lunar and Planetary Surface Landing Research Vehicle: Remote Control Jet Engine Trade Study,” https://chimaera.usu.edu/svn/lpsrv/Jet_Engine_Trade_Study/Jet%20Engine%20Trade%20Study%20Round%20III.pdf, [retrieved 12 June 2010].

- [26] Schaeferemeyer, M. R., Whitmore, S. A., and Wright, C., “Maneuvering and Gravity Offest Flight Controls for an Extraterrestrial Surface Landing Research Vehicle,” *Presented at the 46th AIAA/ASME/SAE/ASEE Joint Propulsion Conference & Exhibit, Nashville, TN*, AIAA Paper AIAA-2010-6936, 2010.
- [27] Calvert, N., Basore, K., Burkhart, C., Cabrera, A., Kosyan, M., Potter, S., Saro, C., Sweeney, J., and van Poolen, C., “Design and Testing of a Quadrotor Aircraft,” http://aeroprojects.colorado.edu/08_09/valasaraptor/AIAA/AIAA_VALASARAPTOR.pdf, [retrieved 1 December 2009].
- [28] Crassidis, J. L., and Junkins, J. L., “Linear Least Squares,” *Optimal Estimation of Dynamic Systems*, Chapman & Hall/CRC, Boca Raton, FL, 2004, pp. 9–13.
- [29] Kreyszig, E., “Confidence Intervals,” *Advanced Engineering Mathematics*, John Wiley & Sons, Hoboken, NJ, 9th ed., 2006, pp. 1052–1053.
- [30] Sutton, G. P., and Biblarz, O., “Nozzle Theory and Thermodynamic Relations,” *Rocket Propulsion Elements*, John Wiley & Sons, New York, NY, 7th ed., 2001, pp. 45–101.
- [31] Zehe, M. J., “Chemical Equilibrium with Applications,” <http://www.grc.nasa.gov/WWW/CEAWeb/ceaHome.htm>, [retrieved 4 August 2011].
- [32] Versteeg, H. K., and Malalasekera, W., “The Finite Volume Method For Convection-Diffusion Problems,” *An Introduction to Computational Fluid Dynamics: The Finite Volume Method*, Pearson Education Limitedl, Harlow, England, 2nd ed., 2007, pp. 134–165.
- [33] Hitec RCD USA, “HS-5245MG Mini Metal Gear Servo,” <http://www.hitecrcd.com/products/digital/digital-micro-mini/hs-5245mg.html>, [retrieved 20 February 2010].
- [34] Drela, M., and Youngren, H., “XFOIL: Subsonic Airfoil Development System,” <http://web.mit.edu/drela/Public/web/xfoil/>, [retrieved 14 January 2010].

- [35] Çengel, Y. A., and Cimbala, J. M., *Fluid Mechanics*, McGraw-Hill, New York, NY, 2006, pp. 46, 567–571, 928–929.
- [36] Phillips, W. F., “Incompressible Flow Over Airfoils,” *Mechanics of Flight*, John Wiley & Sons, Hoboken, NJ, 2nd ed., 2010, pp. 26–38.
- [37] Sommer, S. C., and Short, B. J., “Free-Flight Measurements of Turbulent-Boundary-Layer Skin Friction in the Presence of Severe Aerodynamic Heating at Mach Numbers From 2.8 to 7.0,” NACA TN-3391, 1955.
- [38] Incropera, F. P., Dewitt, D. P., Bergman, T. L., and Lavine, A. S., “Laminar and Turbulent Flow,” *Fundamentals of Heat and Mass Transfer*, John Wiley & Sons, Hoboken, NJ, 6th ed., 2007, p. 360.
- [39] Crane Company, “Flow of Fluids Through Valves, Fittings and Pipe,” Technical Paper 410, 1998.
- [40] Phillips, W. F., “Incompressible Flow over Finite Wings,” *Mechanics of Flight*, John Wiley & Sons, Hoboken, NJ, 2nd ed., 2010, pp. 46–93.
- [41] Gumstix Inc., “Overo[®] Fire COM,” https://www.gumstix.com/store/product_info.php?products_id=227, [retrieved 3 February 2010].
- [42] MicroStrain[®], “3DM-GX3[®]-25, Miniature Attitude Heading Reference System,” <http://microstrain.com/3dm-gx3-25.aspx>, [retrieved 15 November 2009].
- [43] Dorf, R. C., and Bishop, R. H., “Three Term (PID) Controllers,” *Modern Control Systems*, Pearson Prentice Hall, Upper Saddle River, NJ, 11th ed., 2008, pp. 444–447, 791.
- [44] Astrom, K. J., and Murray, R. M., “PID Control,” *Feedback Systems: An Introduction for Scientists and Engineers*, Princeton University Press, Princeton, NJ, 2008, pp. 23–25.

- [45] Franklin, G. F., and Powell, J. D., “Introductory Digital Control,” *Digital Control of Dynamic Systems*, Addison-Wesely Pub. Co., Reading, MA, 2nd ed., 2008, pp. 57–72.
- [46] Wolowicz, C. H., and Yancey, R. B., “Experimental Determination of Airplane Mass and Inertial Characteristics,” NASA TR R-433, 1974.
- [47] Beckwith, T. G., Marangoni, R. D., and Lienhard, J. H., “Assessing and Presenting Experimental Data,” *Mechanical Measurements*, Pearson Prentice Hall, Upper Saddle River, NJ, 6th ed., 2007, pp. 43–73.
- [48] Casella USA, “CEL-573 Real time logging analyzer,” http://www.afcintl.com/other/cel/celpdf/cel-573_brochure.pdf, [retrieved 9 January 2011].